Stripe Melting and Photoinduced Enhancement of Superconductivity in La$_{2-x}$Ba$_x$CuO$_4$

Submitted for the degree of Doctor of Philosophy

Vikaran Khanna

Merton College, University of Oxford

Hilary 2021

Abstract

The interplay between superconductivity and other broken symmetry phases has emerged as a central theme in cuprate physics with increasing reports of charge order in several materials. The relationship between the superconducting state, stripe order, and the so-called low-temperature tetragonal (LTT) structural distortion is one of the great mysteries in high-T_C superconductivity. It has long been believed that stripes are pinned by the LTT distortion and compete with superconductivity to result in an incoherent state with non-superconducting transport. Furthermore, there is evidence that stripes are compatible with in-plane Cooper pairing, creating phases that may involve 2D superconducting CuO_2 planes decoupled as a result of the periodic charge modulation, which, it is speculated, may prevent interlayer Josephson tunneling. In this thesis we combine photoexcitation, time-resolved resonant soft x-ray diffraction and THz time-domain spectroscopy to demonstrate that ultrafast disruption of the stripe ordered phase promptly enhances interlayer Josephson coupling in $La_{1.885}Ba_{0.115}CuO_4$.

Time-resolved resonant soft x-ray diffraction demonstrates that charge order melting occurs immediately after near-infrared photoexcitation whereas the crystal structure remains intact, at least for moderate excitation fluences. THz time-domain spectroscopy reveals that, for the first 2 ps following photoexcitation, a new Josephson plasma resonance edge, at higher frequency with respect to the equilibrium edge, is induced indicating enhanced superconducting interlayer coupling. Furthermore, we show that the fluence dependence of the enhanced interlayer Josephson coupling follows closely that of the stripe order melting and not that of lattice rearrangement.

In the concluding part of the thesis, I also discuss a different excitation geometry (out-of-plane optical pumping), which compared to conventional in-plane excitation promotes a transient superconducting state characterized by both an enhanced transient superfluid density and a longer lifetime.

All in all, this work demonstrates how high-energy charge excitation constitutes, within certain conditions, an alternative method to phonon pumping to promote nonequilibrium superconducting states in high-T_C cuprates, opening new perspectives for the ultrafast optical control of complex solids.

Role of Author

This thesis is the result of multiple collaborations and contributions. The experiments at the core of this thesis were conceptualized by A. Cavalleri and S. S. Dhesi. The $La_{1.885}Ba_{0.115}CuO_4$ single crystals which were primarily studied were grown and characterized by G. D. Gu and J. P. Hill.

Time-resolved resonant soft x-ray diffraction:

Apart from the author, the experimental data at I06 beamline at Diamond was measured by R. Mankowsky, M. Petrich, H. Bromberger, S. A. Cavill, E. Möhr-Vorobeva, M. Först and S. S. Dhesi. The data was analysed by the author and S. S. Dhesi. S. A. Cavill, S. S. Dhesi and the author commissioned several upgrades to the beamline which were required to successfully carry out the measurements.

THz time-domain spectroscopy:

The low frequency THz optics setup was built by the author and D. Nicoletti with helpful inputs from S. Kaiser. The measurements were carried out by the author, Y. Laplace, E. Casandruc and D. Nicoletti. The data analysis, consisting in the determination of the full transient optical response, was performed by the author with support of D. Nicoletti, using a MATLAB code developed by C. R. Hunt [1].

In addition, I also report results from our experiments at the Linac Coherent Light Source. The results from all the above experiments are reported in this thesis and were published in the following papers[1].

---

[1] Other collaborations that the author has been a part are listed but not included in the thesis.

1. Optical enhancement of interlayer coupling in $La_{1.885}Ba_{0.115}CuO_4$ descends from ultrafast melting of striped charge order.

V. Khanna, R. Mankowsky, M. Petrich, H. Bromberger, S. A. Cavill, E. Möhr-Vorobeva, D. Nicoletti, Y. Laplace, G. D. Gu, J. P. Hill, M. Först, A.Cavalleri, and S. S. Dhesi.

Physical Review B, 93, 224522 (2016)

2. Optically induced superconductivity in striped $La_{2-x}Ba_xCuO_4$ by polarization-selective excitation in the near infrared.

D. Nicoletti, E. Casandruc, Y. Laplace, V. Khanna, C. R. Hunt, S. Kaiser, S. S. Dhesi, G. D. Gu, J. P. Hill, and A. Cavalleri.

Physical Review B, 90, 100503(R) (2014)

3. Melting of Charge Stripes in Vibrationally Driven $La_{1.875}Ba_{0.125}CuO_4$: Assessing the Respective Roles of Electronic and Lattice Order in Frustrated Superconductors

M. Först, R. I. Tobey, H. Bromberger, S. B. Wilkins, V. Khanna, A. D. Caviglia, Y.-D. Chuang, W. S. Lee, W. F. Schlotter, J. J. Turner, M. P. Minitti, O. Krupin, Z. J. Xu, J. S. Wen, G. D. Gu, S. S. Dhesi, A. Cavalleri, and J. P. Hill

Physical Review Letters, 112, 157002 (2014)

List of Publications

1. *Optical enhancement of interlayer coupling in $La_{1.885}Ba_{0.115}CuO_4$ descends from ultrafast melting of striped charge order.* V. Khanna et al. Physical Review B, 93, 224522 (2016)

2. *Spatially resolved ultrafast magnetic dynamics launched at a complex-oxide hetero-interface.* M. Först et al. Nature Materials, 14, 883-888 (2015)

3. *Wavelength-dependent optical enhancement of superconducting interlayer coupling in $La_{1.885}Ba_{0.115}CuO_4$.* E. Casandruc et al. Physical Review B, 91, 17 (2015)

4. *Melting of Charge Stripes in Vibrationally Driven $La_{1.875}Ba_{0.125}CuO_4$: Assessing the Respective Roles of Electronic and Lattice Order in Frustrated Superconductors.* M. Först et al. Physical Review Letters, 112, 157002 (2014)

5. *Optically induced superconductivity in striped $La_{2-x}Ba_xCuO_4$ by polarization-selective excitation in the near infrared.* D. Nicoletti et al. Physical Review B, 90, 100503(R) (2014)

6. *Photoinduced melting of magnetic order in the correlated electron insulator* $NdNiO_3$. A.D. Caviglia et al. Physical Review B, 88, 220401(R) (2013)

7. *Optical excitation of Josephson plasma solitons in a cuprate superconductor.* A. Dienst et al. Nature Materials, 12, 535-541 (2013)

8. *Evolution of three-dimensional correlations during the photoinduced melting of antiferromagnetic order in $La_{0.5}Sr_{1.5}MnO_4$.* R. I. Tobey et al. Physical Review B, 86, 064425 (2012)

9. *Driving magnetic order in a manganite by ultrafast lattice excitation.* M. Först et al. Physical Review B, 84, 241104(R) (2011)

10. *Photoinduced Melting of Antiferromagnetic Order in $La_{0.5}Sr_{1.5}MnO_4$ Measured Using Ultrafast Resonant Soft X-Ray Diffraction.* H. Ehrke et al. Physical Review Letters, 106, 217401 (2011)

Acknowledgement

I am deeply indebted to my supervisors Andrea Cavalleri and Sarnjeet Dhesi for their guidance, mentorship and giving me the opportunity to work on exciting scientific problems.

I couldn't have been luckier with the selection of colleagues. Scientifically, they were invaluable, even as I stared blankly back at them in ignorance. Special mention must go to Daniele Nicoletti for always being there and helping me finish my thesis. My early mentors Cristian Manzoni and Matthias Hoffmann are fondly remembered. Working with Michael Först, Michaela Petrich, Katja Möhr-Vorobeva, Roman Mankowsky, Hubertus Bromberger, Stuart Cavill, Yannis Laplace, Eliza Casandruc, has been extremely enjoyable.
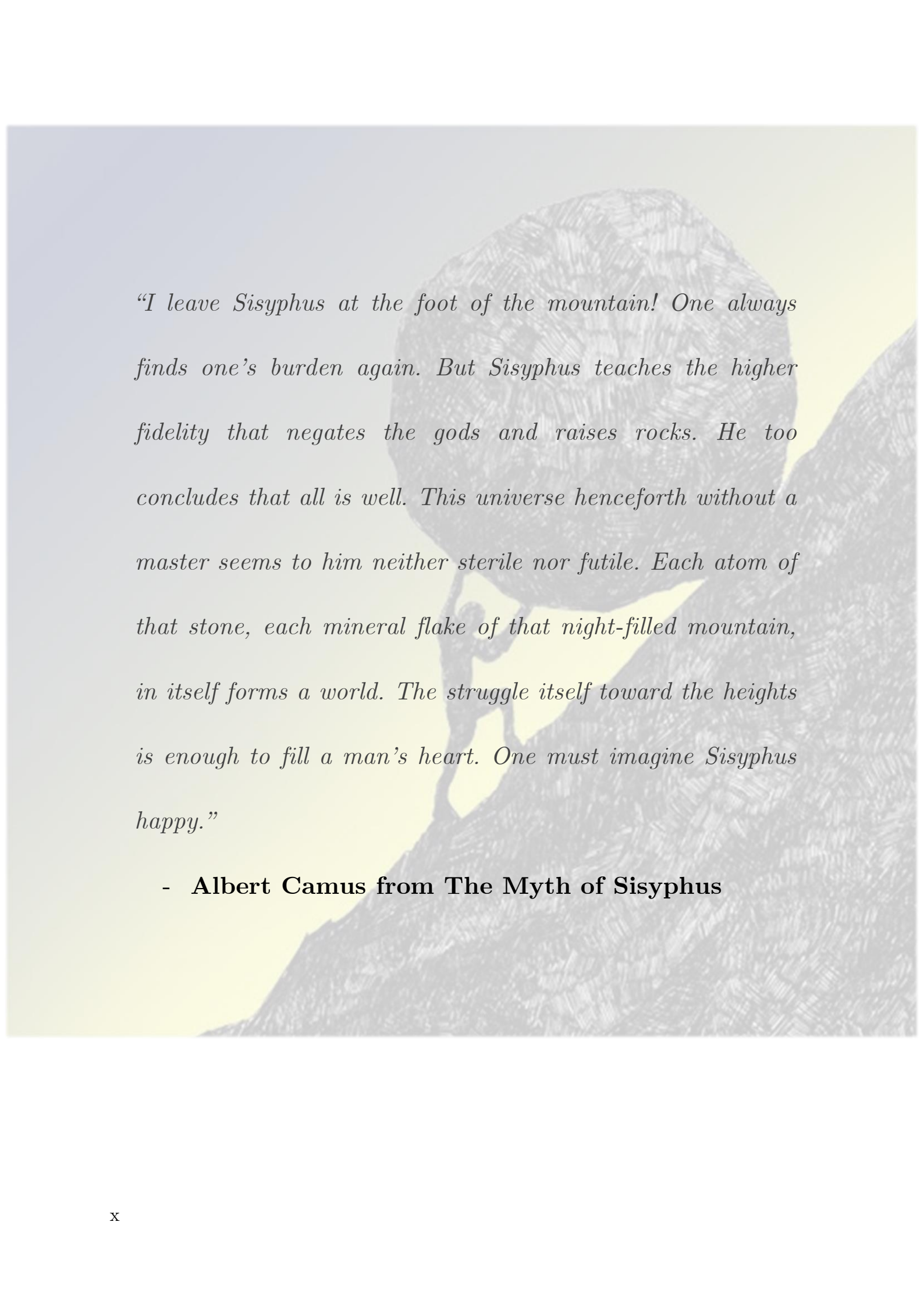
I would like to thank my Oxford 'family' for their encouragement and support all these years. They have helped me pull through some very difficult times.

Lastly, I would like to thank my parents and brother for their love and unquestioning support.

CONTENTS

"I leave Sisyphus at the foot of the mountain! One always finds one's burden again. But Sisyphus teaches the higher fidelity that negates the gods and raises rocks. He too concludes that all is well. This universe henceforth without a master seems to him neither sterile nor futile. Each atom of that stone, each mineral flake of that night-filled mountain, in itself forms a world. The struggle itself toward the heights is enough to fill a man's heart. One must imagine Sisyphus happy."

- Albert Camus from The Myth of Sisyphus

Motivation

The genesis of the work carried out in this thesis comes from the question, can a transient optical field induce superconductivity at temperatures higher than the equilibrium transition temperature, with the goal to achieve room-temperature superconductivity? In recent times, a milestone demonstration of nonequilibrium superconductivity being triggered directly by a light field was reported by Fausti et al. [2] in the cuprate, $La_{1.675}Eu_{0.2}Sr_{0.125}CuO_4$ ($LESCO_{1/8}$). Superconductivity in layered systems like cuprates is established by Josephson tunneling (tunneling of Cooper-pairs) between capacitively coupled stacks of quasi-two-dimensional superconducting Cu-O layers. Superconductivity in each layer and coupling of the layers happens concomitantly, resulting in a three-dimensional superconductor. In $LESCO_{1/8}$ however there are evidences of superconducting fluctuations/precursors up to 40 K, but bulk superconductivity does not arise down to temperatures lower than 5 K. Tranquada et al. [3] have shown that the simultaneous presence of one-dimensional (1D) modulations of charge and spin running along the Cu-O bonds, called stripes, frustrate the interlayer Josephson coupling. The onset of 2D in-plane superconducting correlations and stripes is preceded by a structural phase transition to a low-temperature tetragonal (LTT) phase, which stabilizes the stripes.

Fausti excited $LESCO_{1/8}$ at 10 K, a temperature at which it is non-superconducting, with intense femtosecond optical pulses tuned to 15 μm wavelength (mid-IR). This wavelength is resonant to an in-plane Cu-O vibrational modes and was hypothesized to perturb the LTT structural phase and possibly weaken the stripes and ease the interlayer frustration. The photoinduced state of $LESCO_{1/8}$ was shown to be superconducting-like with the appearance of the Josephson plasmon which is indicative of, Josephson tunneling between planes and, establishment of long-range coherence along the c-axis. As we can see in Fig. M.1, the Josephson plasma edge measured in

1
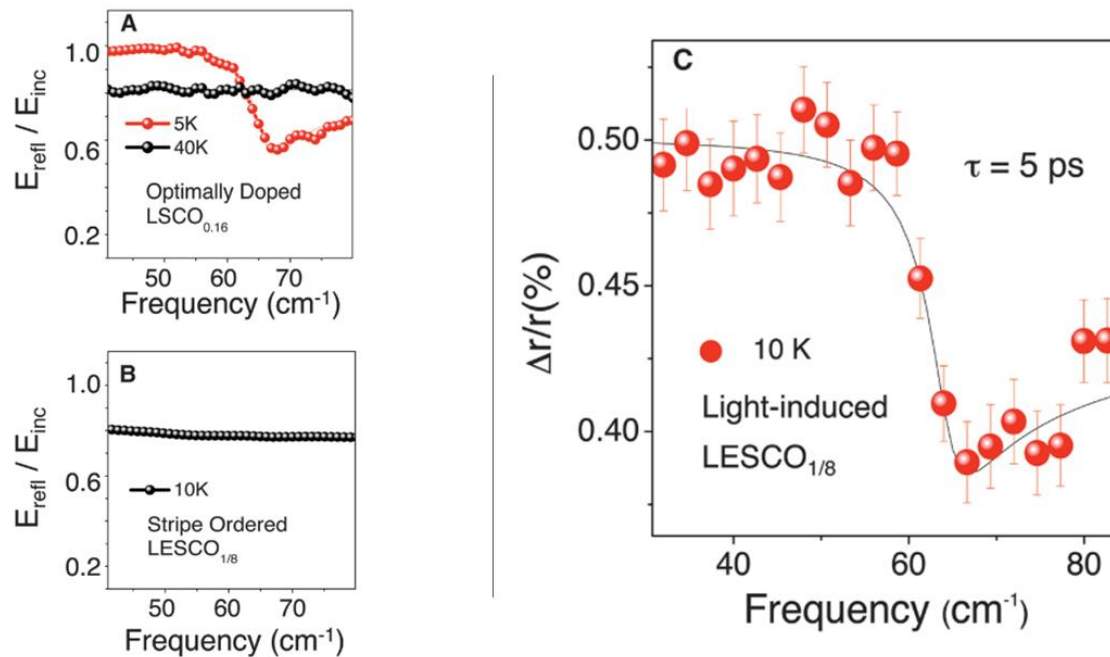
Figure M.1. A: Equilibrium c-axis reflectivity of $La_{1.84}Sr_{0.16}CuO_4$ (T_c = 35 K) above and below T_c. Below T_c the appearance of a JPR reflects coherent interlayer transport. Above T_c, incoherent ohmic transport is reflected by a flat and featureless spectrum. B: Equilibrium c-axis reflectivity of $La_{1.675}Eu_{0.2}Sr_{0.125}CuO_4$ at 10 K. This shows the response of a non-superconducting compound. C: Reflectivity changes in $La_{1.675}Eu_{0.2}Sr_{0.125}CuO_4$ induced by midinfrared excitation at 10 K, showing a light-induced JPR. Figures from [4].

light induced $LESCO_{1/8}$ is at terahertz frequencies, similar to that observed in optimally doped $La_{1.84}Sr_{0.16}CuO_4$ below T_C (= 38 K).

Furthermore, the timescale of the recoupling was shown to be within the 1-2 ps resolution of the THz pulse. Such a short time scale for recoupling may suggest that superconducting correlations are already present in the system before excitation, a scenario which is compatible with the one depicted by Tranquada et al. [3] that the stripe order suppresses bulk superconductivity by frustrating interlayer coupling between Cu-O layers that already retain some superconducting fluctuations above T_C.

The above study threw up some important questions. What is the fate of the stripes and LTT phase post the mid-IR excitation? Does superconductivity emerge in response to stripe melting or do stripes and superconductivity coexist out of equilibrium? Figuring out a cause and effect among the multiple phases in $LESCO_{1/8}$ would help us understand which order needs to be destabilized for superconductivity to appear.

2

The work presented here is in response to the above questions and extend the study to other stripe-ordered cuprates to help elucidate the microscopic mechanisms of photo-induced superconductivity in these materials.

For our study we chose $La_{1.885}Ba_{0.115}CuO_4$ ($LBCO_{11.5\%}$) and $La_{1.875}Ba_{0.125}CuO_4$ ($LBCO_{1/8}$) over $LESCO_{1/8}$ as the stripe order peak intensity is approximately ten times weaker in the latter, making it impossible to do time resolved x-ray measurements at current synchrotrons and free electron lasers. However, both cuprate families are equilibrium superconductors with a maximum $T_c \sim 20$-30 K. They also have similar phase diagrams, with the low temperature ground state characterized by an LTT distortion, and charge and spin stripe order, coinciding with an almost complete suppression of bulk superconductivity at $1/8^{th}$ doping. Furthermore, LBCO at 11.5% doping has a superconducting transition $\sim$ 13 K, allowing us to simultaneously study the interplay between superconductivity, electronic and lattice order in the superconducting state below T_C.

The work detailed in this thesis was done primarily on $LBCO_{11.5}$ and divided between two complementary experimental techniques. In both experiments, $LBCO_{11.5}$ was photoexcited at identical wavelength of $\sim$800 nm (1.55 eV) and fluences. In the first experiment, conducted at the Diamond LightSource synchrotron (UK), we studied the temporal dynamics of stripes and LTT phase to photoexcitation using time-resolved resonant soft X-ray diffraction (TR-RSXD) [5]. In addition TR-RSXD results on the excitation of the in-plane Cu-O stretching phonon with mid-infrared pulses in the non-superconducting, stripe ordered $La_{1.875}Ba_{0.125}CuO_4$ ($LBCO_{1/8}$) performed at the SXR beamline of the Linac Coherent Light Souce (LCLS) are also reported [6]. In the second experiment, carried out in the laser facilities of the Max Planck Institute for Structure and Dynamics of Matter, Hamburg, we used terahertz time-domain spectroscopy to study the response of the Josephson Plasma resonance to photoexcitation [5,7].

Therefore, by using a combination of x-ray and optical spectroscopies, we were able to establish fluence dependence of the photoexcitation and a hierarchy of timescales,

between enhanced superconductivity, melting of charge order, and rearrangement of the crystal structure.

The thesis is organized as follows. In chapter 1, I present an introduction to superconductivity outlining some of the key concepts and models which will be essential in understanding the phenomena. In chapter 2, I focus on the material used for our study, namely $La_{2-x}Ba_xCuO_4$ with an emphasis on the physics of the underdoped regime. Thereafter, I proceed to the experiment side of the thesis, beginning with an introduction to ultrafast pump-probe spectroscopy in Chapter 3. In chapters 4 and 5, I detail the experimental techniques namely, time-resolved resonant soft X-ray diffraction and time domain THz spectroscopy used to investigate the photoinduced properties of $La_{1.885}Ba_{0.115}CuO_4$. In Chapters 6 and 7, I present our results from each technique and conclude with summarizing our results.

1 Introduction to Superconductivity

1.1 Emergent Phenomena

An emergent behavior of a physical system is a qualitative property that can only occur in the limit that the number of microscopic constituents tends to infinity.

-Steven Kivelson [8]

In 1972 P.W Anderson authored an influential paper titled "More is different" [9], where he argued that understanding nature cannot be reduced to reductionism, that is we cannot understand natural phenomena by simply reducing matter to its tiniest constituents or deriving a fundamental equation.

A reductionist hypothesis does not imply a constructionist one:

1. The ability to reduce everything to simple fundamental laws does not imply the ability to start from those laws and reconstruct the universe.

2. The constructionist hypothesis breaks down when confronted by the twin difficulties of scale and complexity.

3. The behaviour of elementary particles, it turns out is not to be understood in terms of a simple extrapolation of a few particles. Instead, at each level of complexity and/or scale entirely new properties appear..."

Very large number of atoms lead to fundamentally new types of behaviour which are not simply the properties of an individual atom multiplied by number of atoms.

Superconductivity is one such aggregate emergent phenomena which is observed in a large assembly of atoms under the right thermodynamic conditions. The discovery of superconductivity dates back to a little over 100 years and though it has been a long and rewarding scientific journey with many important results and applications, with

close to a dozen Nobel Prizes awarded to the field, however a comprehensive theory explaining superconducting behaviour observed in a range of materials is still missing. Certainly, there doesn't exist a reductionist theory, where given a material we can know beforehand if the material will show superconducting behaviour.

In this chapter I give a brief overview of the concepts, and theories/models used to describe the phenomena of superconductivity in conventional and high-temperature superconductors.

1.2 The Discovery

Scientific discoveries often start with trying to answer a question. At the beginning of the twentieth century, one such question namely, what happens to the resistance of metals as you approach 0 K, lead to a remarkable discovery.

In 1908, Heike Kamerlingh Onnes became the first person to liquefy Helium and reach temperatures of 1 K. This technological breakthrough in low-temperature research allowed him to investigate the resistance of metals as you cooled them to absolute zero. It was known that the resistance of metals decreases as you cool them, though it was not known what would happen to their resistance as you cooled them to absolute zero. There were three possibilities as shown in Fig 1.1(a):

1. Electrons would freeze as one approached 0 K, restricting the flow of current and resistance would rise.
2. A non-zero residual resistance.
3. Lastly, resistance would fall to absolute zero.

Onnes, conducted his experiments on Mercury (Hg) since it could be repeatedly distilled to get extremely high purity samples, which was thought to be critical for the experiment. In 1911, his lab measured that the resistance of Hg went to zero just below the boiling point of Liquid-He (4.2 K). This was initially dismissed as an experimental error but on raising the temperature the resistance reappeared. This was the first observation of Superconductivity, Fig. 1.1(b) [10].
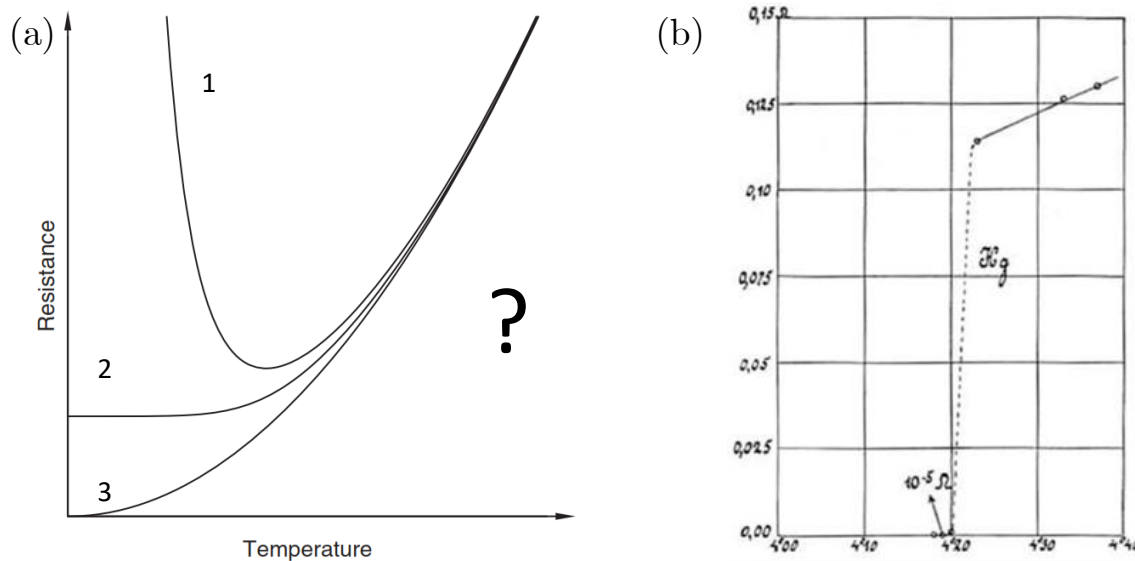
Figure 1.1 (a) Low-temperature resistance of metals according to three popular theories at the turn of the 20th century. Figure adapted from [11]. (b) Discovery of superconductivity: Onnes' experiment of resistance on Mercury (Hg)[10].

Soon after in 1912, he measured superconductivity in Tin ($T_c \sim 3.7$ K) and Lead ($T_c \sim 6$ K) heralding a century of discovery of superconductivity in new materials. For his work on low temperature properties of materials he was awarded the Nobel Prize for Physics in 1913, with the citation stating [12]

For his investigation on the properties of matter at low temperature which led, inter alia, to the production of Liquid He

1.3 Meissner-Ochsenfeld effect: Superconductor vs Perfect Conductors

Superconductivity, as the name suggests, may appear synonymous with a material showing perfect conductivity (resistivity, $\rho \rightarrow 0$), but there is a fundamental difference between a perfect conductor and superconductor. In 1933, Walter Meissner and Robert Ochsenfeld [13] observed that in the presence of magnetic field, if a superconductor is cooled below its transition temperature the magnetic field from within the superconductor is expelled ($B = 0$ inside), thus showing a perfect diamagnetic response (magnetic susceptibility, $\chi \rightarrow -1$):
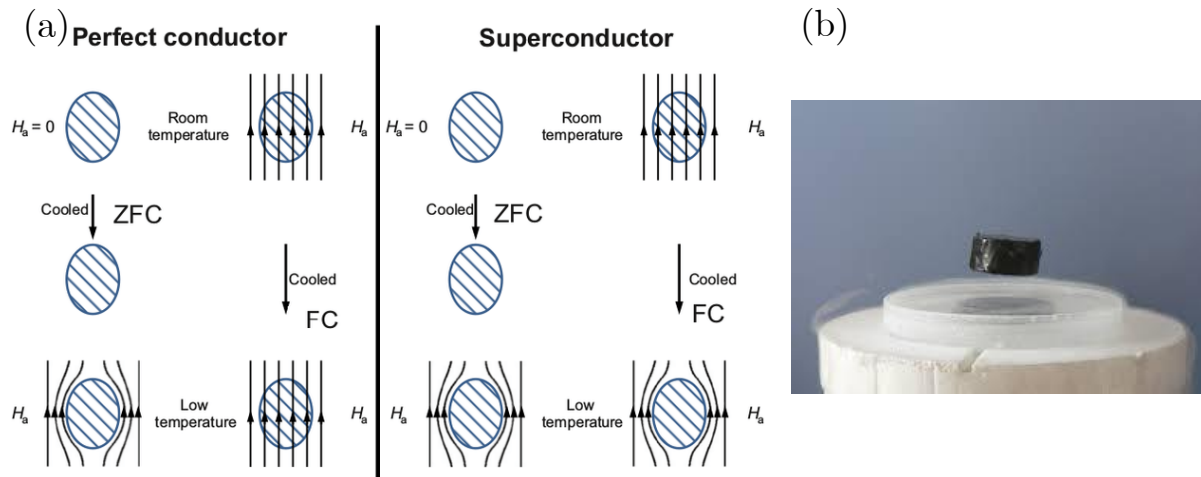
Figure 1.2 (a) Superconductor vs Perfect conductor. A perfect conductor can be thought of as a flux conserving medium, whereas a superconductor is a flux expelling medium [14]. (b) Demonstration of Meissner-Ochsenfeld effect: Magnet levitating above a superconductor cooled by liquid nitrogen [15].

$$B = \mu_0(M + H) = 0 \;\Rightarrow\; M = -H \;\Rightarrow\; \chi = \frac{dM}{dH} = -1 \tag{1.1}$$

The expulsion of a magnetic field from a superconductor, is known as the Meissner-Ochsenfeld effect[2]. This occurs due to currents appearing on the surface of the superconductor which screen the inside of a superconductor from an external field and creates an external field opposite to the one applied.

The response of a perfect conductor to a magnetic field is quite different. As shown in Fig. 1.2, even though the final state is characterized by the same thermodynamic variables, namely temperature (T) and magnetic field (H), the final state of a perfect conductor is defined by the history of the sample. However, in the case of a superconductor, irrespective of the sequence of events, the sample would end up in a state where there is complete expulsion of the magnetic flux and the final state is y defined only by T and H. Therefore, superconductivity is a stable thermodynamic state defined by $\rho \to 0$ and $\chi \to -1$, not just $\rho \to 0$. There exists a critical field $(H_c(T))$ above which a superconductor is unable to expel an external magnetic field. Empirically, $H_c(T)$ shows a parabolic dependence on temperature:

---

[2] Magnetic levitation, where a magnet hovers mid-air above a cooled superconductor, is a popular science demonstration of the Meissner-Ochsenfeld effect.

$$H_c(T) = H_c(0) \left(1 - \frac{T}{T_c}\right)^2 \tag{1.2}$$

Where $H_c(0)$ is the value of the field at T = 0 K.

1.4 Entropy

The Meissner-Ochsenfeld effect suggests that the superconducting state has lower energy than the normal state, as work must be done to expel or keep out the magnetic flux. At $H_c(T)$, it is no longer energetically favourable for the superconducting state to expel the magnetic flux and superconductivity is destroyed. The difference in the Gibbs free energy $(G_{n,s})$ of the normal and superconducting state in zero field is[3]

$$G_n(T,0) - G_s(T,0) = \frac{H_c^2}{8\pi} \tag{1.3}$$

$$\Rightarrow G_n(T,0) > G_s(T,0) \tag{1.4}$$

The energy difference $\frac{H_c^2}{8\pi}$ is called the condensation energy and gives a sense of the stability of the Meissner state vis-à-vis the normal state.

Furthermore, using the relation $S = \left(\frac{\partial G}{\partial T}\right)_H$ we can find the difference in entropy (S) of the two states,

$$S_n(T,0) - S_s(T,0) = -\frac{H_c}{4\pi}\frac{dH_c}{dT}. \tag{1.5}$$

Since $\frac{dH_c}{dT}$ is always negative, the right-hand side of the equation is always positive.

$$\Rightarrow S_n(T,0) > S_s(T,0) \tag{1.6}$$

Thus, the entropy of the superconducting state is less than the normal state. Or in other words, the superconducting state is described by more order than the normal state.

---

[3] Using the relations, $\left(\frac{\partial G}{\partial H}\right)_T = \mu_0 M$ and $M = -H$

The normal-superconducting phase transition is of second-order in zero field, as at T_c, $H_c = 0 \implies S_n(T, 0) = S_s(T, 0)$. However, in the presence of a field, the entropy change is discontinuous, and the phase transition is of first-order[4].

1.5 Phenomenological Theories

In 1934, Henrik Casimir and Cornelius Jacobus Gorter formulated a 'two-fluid' model [16] suggesting that the total current density in a superconductor is a superposition of, the normal current density (j_n) comprising of normal electrons with concentration (n_n), having properties of the normal state, and a supercurrent density (j_s) with concentration of superelectrons (n_s) which are responsible for the superconducting properties and only observed below T_c. Thus, we have

$$j_n + j_s = j \, , \tag{1.7}$$

$$n_n + n_s = n = \frac{N}{V} \tag{1.8}$$

Though this phenomenological model had limited success in explaining some of the observed properties in superconductors, the basic premise of the two-fluid model, two co-existing electron fluids, has been extended to other theories.

In 1935, the London brothers, Fritz and Heinz London, developed a theory to encapsulate the lossless diamagnetic response of a superconductor[5] [17]. An intuitive explanation for the London theory follows.

---

[4] There is latent heat associated with the phase transition as it takes place at a temperature lower than T_c.

[5] Developed during their stay in Oxford, where the brothers were visiting as part of a fellowship put together by Frederick Lindeman to accommodate scientists fleeing Nazi Germany [11].

To account for perfect conductivity, we can consider that the superconducting electrons are insensitive to scattering. Using the relation for canonical momentum p $(= m\mathbf{v} + e\mathbf{A}/c)$ and assuming that the superelectrons retain their ground-state property of $\langle \mathbf{p} \rangle = 0$, the supercurrent density can be expressed in terms of the vector potential

$$j_s = -\frac{q^2 n_s}{m^* c} \mathbf{A} \tag{1.9}$$

Where, q and m^* are the charge and mass of the superelectrons. The above expression is analogous to Ohm's law $(j_n = \sigma_n \mathbf{E})$. Instead of the electric field, it is the magnetic vector potential $\mathbf{A}$ driving a supercurrent j_s, and these supercurrents shield the bulk of a superconductor from an external magnetic field. As $\mathbf{A}$ is not a gauge-invariant quantity and charge conservation requires $\nabla.j_s = 0$, the London gauge $\nabla.\mathbf{A} = 0$ is used above. Taking the time derivative of eq. 1.9, yields,

$$\frac{\partial j_s}{\partial t} = \frac{q^2 n_s}{m^* c} \mathbf{E} \tag{1.10}$$

This is the first London equation, and it describes perfect conductivity since any electric field accelerates the superconducting electrons. This contrasts with a normal conductor, where an electric field maintains the velocity of the electrons against resistance (Ohm's law).

Further, if we take the curl of the first London equation and integrate in time, we get

$$\nabla \times j_s = -\frac{q^2 n_s}{m^* c} B + C(\mathbf{r}) \tag{1.11}$$

$C(r)$ can be determined from initial conditions. However, to account for the Meissner-Ochsenfeld effect, Londons postulated that $C(\mathbf{r}) \equiv 0$ irrespective of the history of the sample, resulting in the second London equation

$$\nabla \times j_s = -\frac{q^2 n_s}{m^* c} B \tag{1.12}$$
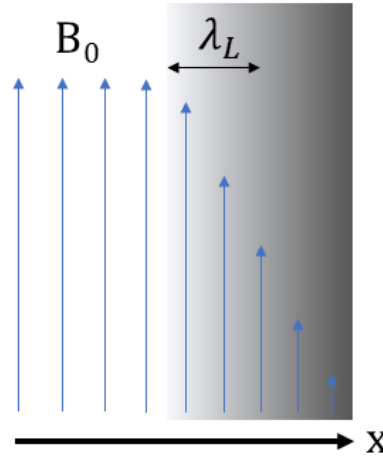
Figure 1.3 Illustration of the London penetration depth. B_0 is the magnetic field at the surface and decays exponentially inside the superconductor. The London penetration depth λ_L defines the distance over which applied field is reduced to 1/exp.

Using Ampere's law, $\nabla \times B = \frac{4\pi}{c} j_s$, the above equation reduces to

$$\nabla^2 B = \frac{1}{\lambda_L^2} B \tag{1.13}$$

Where, $\lambda_L = \sqrt{\frac{m^* c^2}{4\pi q^2 n_s}}$ has dimensions of length and is known as the London penetration depth. For a 1D case we get the solution: $B(x) = B_0 e^{-x/\lambda_L}$. Therefore, the London penetration depth defines the screening length over which the applied field is reduced to $1/e$ and for $x \gg \lambda_L$, $B(x) \to 0$ in accordance with the observed Meissner-Ochsenfeld effect[6]. Using Maxwell's equations, we can obtain a similar relation for the attenuation of the electric field.

The London theory was further developed by Brian Pippard [18]. While conducting surface impedance measurements in superconductors he observed that the superconducting state is destroyed at depths much greater than the London penetration depth. Furthermore, he noted that even a slight addition of impurities changed λ_L significantly, while leaving T_c and H_c unchanged. This led him to develop a non-local generalization of the second London equation, implying that the current density j_s at

---

[6] For a perfect conductor as discussed in the previous section, the magnetic flux does not change in time i.e $\dot{B} = 0$.

a point in space is not simply a function of A at that point but on the value of A averaged over a volume surrounding that point[7]. Pippard defined the radius of this volume as the coherence length, $\xi(l)$, which is independent of temperature and since it accounts for impurities, is related to the mean free path l of an electron in metals –

$$\frac{1}{\xi(l)} = \frac{1}{\xi_0} + \frac{1}{l} \tag{1.14}$$

Where, ξ_0 is the value of $\xi(l)$ in the limit of large l. ξ_0 can be approximated using the Heisenberg uncertainty principle and is in the range of $10^3 - 10^4$ Å.[8]

1.6 Optical Conductivity in a two-fluid model

In the previous sections we have not considered the time-dependence of the external electromagnetic field. To model the response of a superconductor to a time-dependent electric field, we must treat conductivity as a frequency dependent complex quantity[9] and consider the parallel ohmic response of the normal electrons. For an electric field, $E(t) = E_o e^{i\omega t}$, the first London equation gives a $1/\omega$ dependence to the imaginary part of the conductivity [19]

$$\sigma_{2s}(\omega) = \frac{n_s q^2}{m^* \omega c} \tag{1.15}$$

Using Kramers-Kronig relations[10], the corresponding real part of the conductivity is,

$$\sigma_{1s}(\omega) = \frac{n_s \pi q^2}{2m^* c} \delta\{\omega = 0\} \tag{1.16}$$

---

[7] This is analogous to the non-local response of an electric field in a metal.

[8] Only electrons within $\sim k_B T_c$ of the Fermi surface play a role for phenomena that sets in at T_c . These electrons have a momentum range $\Delta p \approx k_B T_c / v_F$, where v_F is the Fermi velocity. Therefore, the uncertainty in position is given as:

$$\Delta x \gtrsim \hbar / \Delta p \approx \hbar v_F / k_B T_c$$
$$\Rightarrow \xi_0 = a \frac{\hbar v_F}{k_B T_c} \sim 10^3 - 10^4 \text{ Å}$$

Where a is numerical constant of the order of unity.

[9] $\sigma(\omega) = \sigma_1(\omega) + i\sigma_2(\omega)$

[10] The Kramers-Kronig relations are simple integral formulas relating a dispersive process to an absorption process, and vice versa [82].

The response of the normal electrons can be estimated using the Drude model. In this model, electrons under the influence of an applied field execute a diffusive motion, with a relaxation time τ_n which defines the time for the system to relax back to equilibrium once the electric field is removed. The equation of their motion is

$$m\frac{dv}{dt} = -eE(t) - \frac{mv}{\tau} \tag{1.17}$$

Giving a complex optical conductivity,

$$\hat{\sigma}_n(\omega) = \frac{n_n e^2 \tau_n}{m}\frac{1}{1 - i\omega\tau_n} \tag{1.18}$$

The efficacy of this two-fluid model is limited to frequencies below the superconducting energy-gap frequency, since additional loss mechanisms set in above that frequency, and dissipation approaches that of the normal state. In this regime the relaxation time of the normal electrons is short, such that $\omega\tau_n \ll 1$. Therefore, the combined conductivity of the two fluids reduces to -

$$\hat{\sigma}(\omega) = \frac{n_s \pi q^2}{2m^* c}\delta\{\omega = 0\} + \frac{n_n e^2 \tau_n}{m} + i\frac{n_s q^2}{m^* \omega c} \tag{1.19}$$

Thus, superconductors always show finite dissipation at nonzero frequencies, with the ohmic channel providing dissipation, which is reflected in the real part of the conductivity. In contrast, the imaginary part shows $1/\omega$ frequency dependence and is proportional to the superfluid density, n_s.

1.7 The Ginzburg Landau Theory

In the London theory the superfluid density n_s is assumed to be homogenous (constant in space) therefore it cannot describe variations in n_s due to change, in temperature, applied magnetic field or at the interface of a superconductor. In 1950, Ginzburg[11] and Landau proposed a phenomenological theory which accounted for spatial variations of

---

[11] Vitaly L. Ginzburg was awarded the Physics Nobel prize in 2003 "for pioneering contributions to the theory of superconductors and superfluids" [100].

n_s. Their work extended Landau's theory of second-order (continuous) phase transitions to charged superfluids. Phase transitions can be characterized by a change in the underlying symmetry of a physical system. This change can be quantified by an order parameter[12], a concept introduced by Landau. The basic premise of Landau's theory is that the free energy F of a system is a function of the order parameter and other thermodynamic variables, and the equilibrium state is the one that minimizes the free energy. Since the order parameter is small close to the transition temperature, the free energy can be expanded as a Taylor's series as a function of the order parameter, including only those terms that are allowed by symmetry.

Ginzburg and Landau proposed a complex pseudowavefunction $\psi(r,t)$ as an order parameter associated with the superconducting transition, with $|\psi(r,t)|^2$ proportional to density of superconducting electrons, n_s [20,21]. To account for spatial inhomogeneities of n_s, they incorporated the gradient of the order parameter into the expansion for free energy.

Therefore, for a superconductor the free energy Landau functional is

$$F_s(\psi, \mathbf{A}) \cong \int d^3r \left[\alpha|\psi|^2 + \frac{1}{2}\beta|\psi|^4 + \frac{1}{2m^*}\left|\left(\frac{\hbar}{i}\nabla - \frac{q}{c}\mathbf{A}\right)\psi\right|^2 + \frac{B^2}{8\pi}\right] \qquad (1.20)$$

The above equation describes the free energy of a superfluid condensate of particles with charge q and effective mass m^* in a magnetic field (A is the vector potential). The phenomenological coefficients α and β are chosen to minimize the energy.

On minimizing the free energy functional with respect to ψ and A, we get the following two Ginzburg-Landau (GL) equations,

$$\frac{1}{2m^*}\left(\frac{\hbar}{i}\nabla - \frac{q}{c}\mathbf{A}\right)^2\psi + \beta(T)|\psi|^2\psi + \alpha(T)\psi = 0 \qquad (1.21)$$

---

[12] The order parameter is taken to be zero in the high temperature disordered phase and has a finite value in the low temperature ordered phase.

$$i\frac{q\hbar}{2m^*}(\psi^*\nabla\psi - \psi\nabla\psi^*) - \frac{q^2}{m^*c}|\psi|^2\mathbf{A} = \mathrm{j}_s \qquad (1.22)$$

The 1st GL equation is analogous to a nonlinear Schrödinger equation for a free particle and describes the dependence of the order parameter on the magnetic vector potential $\mathbf{A}$. The 2nd GL equation gives the superconducting current density, and its form is similar to the probability current of a wavefunction.

The GL theory encapsulates two length scales which play a fundamental role in characterizing superconductors. The length scale over which the magnetic field penetrates a superconductor (or in other words destroys superconductivity), is the effective penetration depth:

$$\lambda = \sqrt{\frac{mc^2}{4\pi|\psi|^2e^2}} \qquad (1.23)$$

And the length scale over which n_s can spatially vary without appreciable change to the superconducting state is known as the coherence length[13] and given by

$$\xi = \frac{\hbar}{\sqrt{2m|\alpha(T)|}} = \frac{\Phi_0}{2\sqrt{2}\pi H_c\lambda} \qquad (1.24)$$

where $\Phi_0 = \frac{hc}{2e}$ is the quantum of magnetic flux. The ratio of these two length scales is the dimensionless Ginzburg-Landau parameter, $\kappa = \lambda/\xi$. In elemental superconductors the penetration depth is much smaller than the coherence length, and $\kappa \ll 1$. These are called Type I superconductors and the superconducting state is characterized by an almost perfect Meissner-Ochsenfeld state until the critical field H_c.

In 1957, Abrikosov published an important result where he explored $\xi < \lambda$ [22]. Specifically, for $\kappa > 1/\sqrt{2}$, he showed that instead of a discontinuous breakdown of superconductivity at H_c, there is a continuous penetration of flux starting at a lower

---

[13] The coherence length introduced by Pippard and that by Ginzburg-Landau are distinct but related quantities. For pure superconductors, and $T \ll T_c$, $\xi(T) \approx \xi_0$. Henceforth, ξ will refer to the GL coherence length.
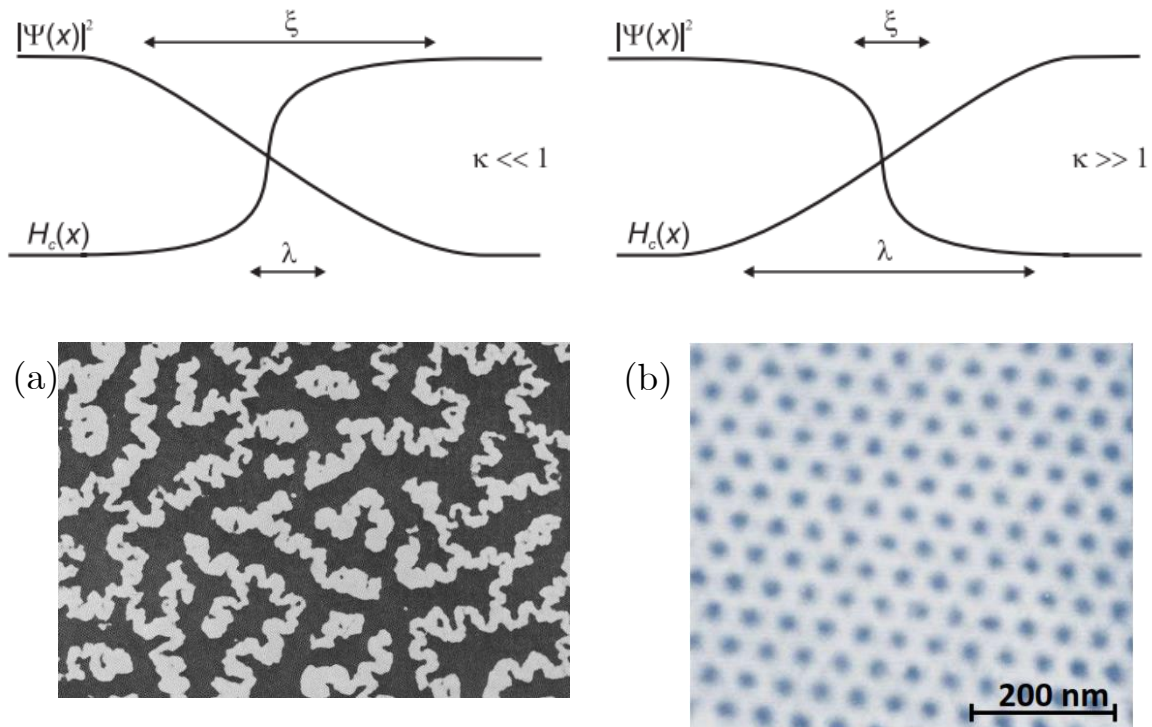
Figure 1.4 (Top panel) Interface between superconducting and normal domains with corresponding length scales (ξ, λ). Scanning tunneling microscope images of (a) Domains and (b) vortices formation in Type I and type II superconductors respectively [23,24].

critical field H_{c1} and only reaching a higher critical field H_{c2} is superconductivity destroyed. Since there is partial penetration of the field, the energy cost of holding the field out is less, therefore $H_{c2} > H_{c1}$. Between the two critical fields, H_{c1} and H_{c2}, the superconductor is in the mixed state or Schubnikov phase, where the flux penetrates in a triangular array of flux tubes, each carrying a quantum of flux Φ_0 [19]. These types of materials are called Type II superconductors and is the most common class of superconductors. High-T_c cuprates which will be introduced in the next chapter are type II superconductors.

1.8 BCS Theory

The discovery of the isotope effect in 1950 independently by Maxwell and Reynolds et al. [25,26] played a pivotal role in broadening our understanding of superconductivity. They observed that the T_c of Hg isotopes is proportional to the inverse square root of their isotopic mass M - $T_c \propto M^{-0.5}$. The isotope effect was observed in other superconductors as well. The universality of the isotope effect suggested that lattice

17

vibrations (phonons) play a crucial role in determining T_c. Thus, to develop a microscopic theory for superconductivity one has to look beyond electrons.

It was shown by Herbert Fröhlich and subsequently more comprehensively by John Bardeen and David Pines [27,28] that an attractive interaction between electrons can be mediated through phonons. Conceptually this mechanism depicted in fig. 1.5 can be seen as follows. As ions are heavier than electrons, lattice distortions caused by electron-ion collisions persist long after the electron that caused them has passed. Locally this gives rise to a small dipole moment which can attract other electrons in the vicinity, with the Coulomb repulsion between electrons being largely screened by the positive ions.

This attractive Fröhlich interaction is represented in fig1.5, shows an electron of wave vector $\vec{k}_1$ scattered into state $\vec{k}'_1$ and emitting a phonon of wave vector $\vec{q}$; $\vec{k}_1 = \vec{k}'_1 + \vec{q}$. A second electron with wave vector $\vec{k}_1$ absorbs the phonon and scatters into state $\vec{k}'_2$; $\vec{k}_2 + \vec{q} = \vec{k}'_2$. Conservation of crystal momentum between the initial and final electron states, gives [29]

$$\vec{k}_1 + \vec{k}_2 = \vec{k}'_1 + \vec{k}'_2 = \vec{b} \tag{1.25}$$

Where the vector $\vec{b}$ denotes the sum of the crystal momenta of this electron pair. It follows that the energy change of the first electron before and after scattering is less than the phonon energy. If E_1 and E'_1 denote the energy of the first electron before and after scattering, respectively, it follows that $\Delta E_1 = |E_1 - E'_1| < \hbar\omega_q$ where $\hbar\omega_q$ is the phonon energy. Since the Debye frequency $\omega_D > \omega_q$ and $(\hbar\omega_D/E_F)\sim 10^{-3}$, the energy scale of this attractive interaction is small.

Leon Cooper, observed that the energy change associated with the pairing mechanism

$$\Delta E = \frac{\hbar^2}{m}k_F\Delta k \simeq \hbar\omega_D \tag{1.26}$$
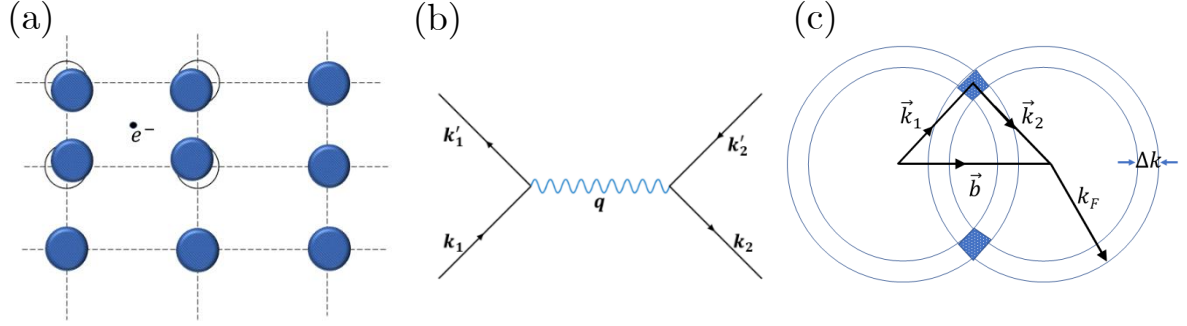
Figure 1.5 (a) A schematic diagram of an electron polarizing positive ions in its vicinity to create an attractive potential for a second electron following in the wake of the first electron. (b)Feynman diagram depicting the electron-phonon interaction. (c) Schematic diagram showing two shells in $\vec{\boldsymbol{k}}$-space of radius $\boldsymbol{k_F}$ and thickness $\Delta\boldsymbol{k}$ corresponding to the two electrons forming a Cooper pair [29].

implies

$$\Delta k \simeq \frac{m\omega_D}{\hbar k_F} \tag{1.27}$$

The maximum number of electron pairs satisfying eqs (1.26-1.27) occurs when $\vec{b} = 0$ or $\vec{k}_1 = -\vec{k}_2$. Therefore, an arbitrary weak attractive electron-electron interaction, makes the Fermi liquid unstable towards pairing of electrons with equal and opposite momentum and spin[14]. This bound electron pair is called a Cooper pair and has a spatial extent[15] determined by the coherence length ξ. Subsequently, Schrieffer described the superconducting ground state by a single macroscopic wavefunction constructed from a coherent many-body wavefunction of Cooper pairs. In 1957, John Bardeen[16], Leon Neil Cooper and John Robert Schrieffer published their seminal paper outlining a microscopic theory for superconductivity, known as the BCS theory [30]. For their work they were jointly awarded the Nobel prize in Physics in 1972 [31].

One of the key predictions of the BCS theory is the energy of the ensemble of Cooper pairs is lowered by $2\Delta \sim 3.5k_B T_c$. This energy gap observed experimentally is a measure of the binding energy of Cooper pairs and gives the minimum energy required to break

---

[14] To maximize the probability of the electrons being in proximity.

[15] Considering the relaxation frequency of phonons, $\tau_D = 2\pi/\omega_D = 10^{-13}s$ and Fermi velocity of electrons, $v_F \sim 10^8 \, cm/s$. As a result, electrons within a range $\sim 10^3 \text{Å}$ are affected.

[16] To date John Bardeen is the only double recipient of the Nobel Prize in Physics. He was jointly awarded the 1956 Physics Nobel Prize, with William Shockley and Walter Brattain, for the invention of the transistor.

19

a pair and create two quasiparticle excitations. Since $2\Delta \leq \hbar\omega_D$, the upper limit of T_c for a superconductor with pairing mechanism driven by electron-phonon interaction[17] corresponds to ~ 30 K. Therefore, the discovery in 1987 of superconductors with T_c ~ 100 K was so surprising. It was evident that the BCS theory is insufficient in describing superconductors with such high transition temperatures. Pairing interactions in such superconductors is unconventional and involves exchange of bosons other than phonons. The quest to find the 'glue' that leads to pairing of electrons at temperatures pushing towards room-temperatures has been one of the outstanding/pressing fundamental problems in physics with game-changing technological applications.

1.9 Josephson Effect

As described in the previous section the superconducting state is defined as a coherent superposition of Cooper pairs, that is it describes a state with a fixed/rigid phase. This arises from the spontaneous symmetry breaking of U(1) rotational symmetry with respect to the phase of the macroscopic wavefunction, as depicted in Fig. 1.6.

What is the physical significance of a superconductor having a fixed phase and can this phase be observed? This was the question pondered by a young graduate student Brian D. Josephson in 1961 [32]. The absolute phase φ of an isolated superconductor is unobservable, however the phase difference $\Delta\varphi$ between two superconductors can in principle be measured. The number-phase uncertainty relation,

$$\Delta N \Delta \varphi \geq \frac{1}{2} \tag{1.28}$$

suggests that to observe $\Delta\varphi$ the two superconductors would have to exchange electrons[18]. This led Josephson to study the tunneling rate of Cooper pairs across a thin

---

[17] MgB_2 with a of T_c of 39 K has the highest transition temperature for a conventional superconductor.
[18] The superconducting state is characterized by a definite phase, φ and a corresponding uncertainty in the number of Cooper pairs, N. However, in the thermodynamic limit $N \rightarrow \infty$, the uncertainty in φ is negligible.
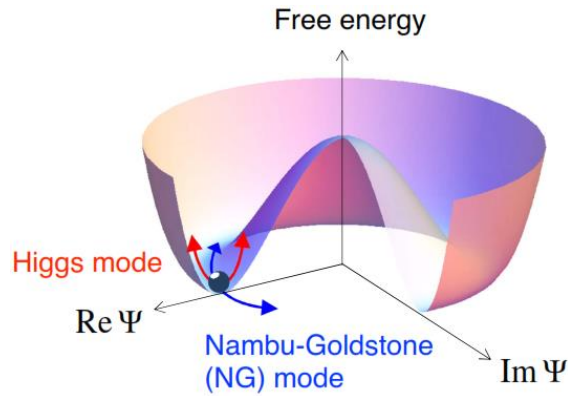
Figure 1.6   Illustration of spontaneous symmetry breaking for a system having U(1) rotational symmetry. The Mexican-hat free energy potential is function of the complex order parameter Ψ. In the ground state fluctuations of the phase (Nambu-Goldstone mode) and amplitude (Higgs mode) of the order parameter lead to emergence of two types of collectives modes [33].

insulating barrier separating two identical superconducting electrodes—a Josephson junction.

However, Josephson predicted tunneling of Cooper pairs to be a coherent process, implying that the probability of a Cooper pair to tunnel through a barrier is the same as that for a single electron. He showed that the phase difference between two condensates drives a tunneling current across the junction even in the absence of an external potential. This is known as the DC Josephson effect. Furthermore, he predicted that application of a potential difference (V) across the junction would lead to a periodically varying current at a frequency $2eV/\hbar$. This is known as the AC Josephson effect. The Josephson effects were subsequently confirmed experimentally [34,35] and in 1973 Josephson was jointly[19] awarded the Nobel prize in Physics *"for his theoretical predictions of the properties of a supercurrent through a tunnel barrier, in particular those phenomena which are generally known as the Josephson effects".* [36]

The physics of the Josephson effects can be deduced from the 2nd Ginzburg-Landau equation which relates the order parameter to the supercurrent density. On substituting the macroscopic wavefunction $\psi(r,t) = \sqrt{n_s(r,t)}\, e^{i\varphi(r,t)}$, describing the entire

---

[19] Together with Leo Esaki and Ivar Giaever.
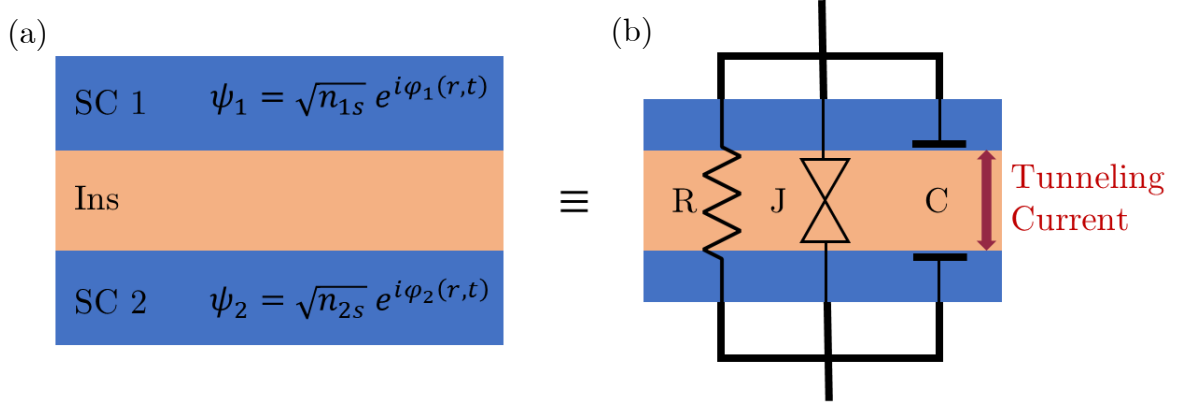
Figure 1.7 (a) Josephson junction and (b) equivalent RCSJ circuit.

ensemble of Cooper pairs in a superconductor, and replacing charge q and mass m^* with that of a Cooper pair, $-2e$ and $2m$ respectively, eq. 1.22 reduces to

$$j_s = \frac{\hbar e n_s}{m} \left[\nabla\varphi(r,t) - \frac{2\pi}{\Phi_o} \mathbf{A}(\text{r},t) \right] \tag{1.29}$$

If we consider current across a SIS Josephson junction—two bulk superconductors separated by an insulator—the supercurrent across the junction, I_s, is proportional to a gauge invariant phase difference $\gamma(r,t)$, defined as

$$\gamma(r,t) \equiv \int_1^2 \left(\nabla\varphi - \frac{2\pi}{\Phi_o}\mathbf{A} \right) \cdot ds \tag{1.30}$$

$$= \varphi_2(r,t) - \varphi_1(r,t) - \frac{2\pi}{\Phi_o} \int_1^2 \mathbf{A} \cdot ds \tag{1.31}$$

In the absence of a magnetic field ($\mathbf{A} \equiv 0$) the current across the Josephson junction is proportional to the phase difference ($\Delta\varphi$) of the two condensates. As the wavefunctions of the junction electrodes have a 2π periodicity and time-invariance of Josephson current requires that $I_s(\Delta\varphi) = -I_s(-\Delta\varphi)$. Thus, the supercurrent across a SIS junction should have the form

$$I_s = I_c \sin\Delta\varphi + \sum_{m=2}^{\infty} I_m \sin(m\Delta\varphi) \tag{1.32}$$
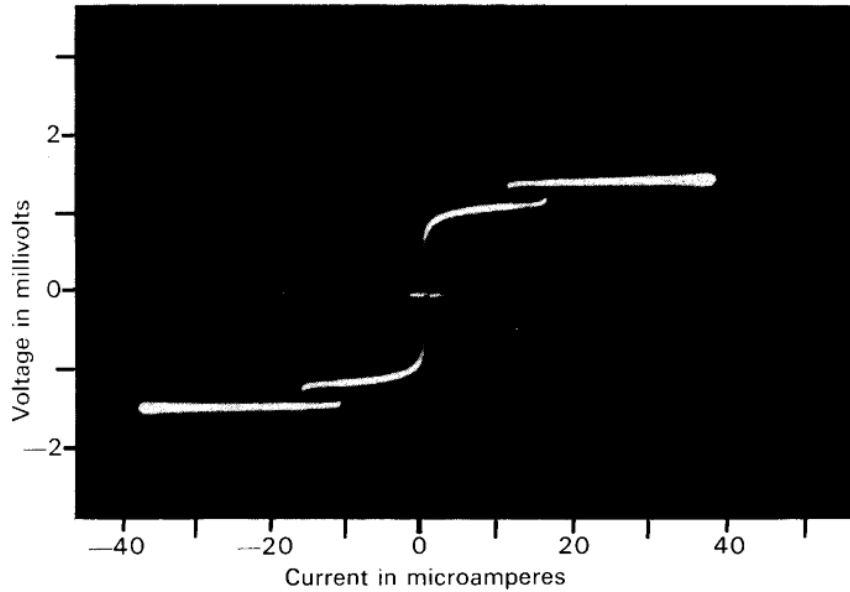
Figure 1.8   The first published observation of tunnelling between two evaporated-film superconductors [34]. A zero-voltage supercurrent is clearly visible [37].

I_c is the critical or maximum Josephson current, which is determined by the coupling strength between the two electrodes. In the weak coupling limit, we can ignore the second term, thus simplifying the expression to

$$I_s = I_c \sin \Delta\varphi \tag{1.33}$$

This is known as the DC Josephson effect as it implies that even in the absence of an external potential, a supercurrent across the Josephson junction would continue to flow till the phase difference $\Delta\varphi$ is maintained.

In the presence of a constant bias voltage V, the phase difference would evolve according to

$$\frac{d}{dt}\Delta\varphi = \frac{2e}{\hbar}V \tag{1.34}$$

leading to an alternating supercurrent

$$I_s(t) = I_c \sin\left(\Delta\varphi_0 + \frac{2e}{\hbar}Vt\right) \tag{1.35}$$

23

oscillating at the frequency of $\omega_J = 2eV/\hbar$, whereby the net current across the junction remains zero. This is known as the AC Josephson effect[20].

The DC and AC Josephson effect imply a nonlinear inductance, as a small change in phase difference (small enough to preserve the zero-voltage state) gives rise to a current change,

$$\frac{dI_s}{dt} = I_c \cos \Delta\varphi \frac{d}{dt} \Delta\varphi \tag{1.36}$$

which in turn induces a voltage

$$V = \overbrace{\frac{\hbar}{2eI_c \cos \Delta\varphi}}^{L} \frac{dI_s}{dt} \tag{1.37}$$

The above expression describes a nonlinear inductance $L = \hbar/(2eI_c \cos \Delta\varphi)$ that depends on the equilibrium phase difference between the two condensates. The phase difference can be adjusted by an external current or voltage source, and in its absence takes the minimum value $L_0 = \hbar/(2eI_c)$. The Josephson inductance is kinetic inductance as it arises from the kinetic energy of the Cooper pairs.

In the finite voltage regime, a Josephson junction allows single particle tunneling which can be modeled by an ohmic resistivity R in parallel to the junction and due to the geometry of the junction a parallel capacitor is added to include charging effects. Therefore, the total current flowing through a Josephson junction can be described by a resistively and capacitively shunted junction (RCSJ), with the total current through the junction equal to the contribution from the three branches, and given by,

$$I = I_c \sin \Delta\varphi + \frac{V}{R} + C\dot{V} \tag{1.38}$$

---

[20] Important for metrology as it relates frequencies (or time) to voltages.
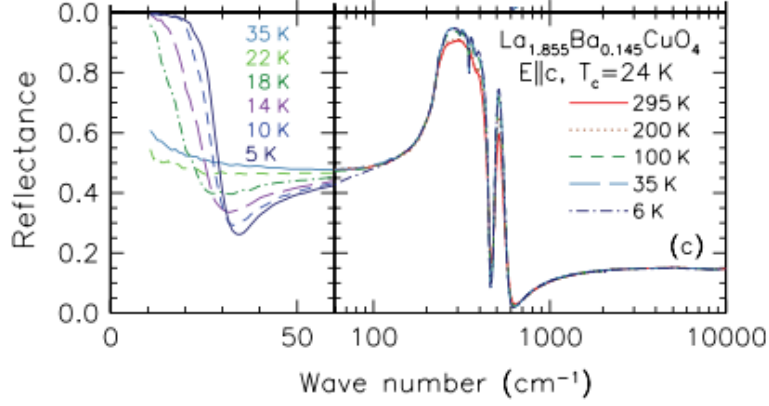
Figure 1.9 Infrared reflectivity spectra of $La_{2-x}Ba_xCuO_4$ for x = 0.145 (T_c = 24 K) with polarization perpendicular to the CuO$_2$ planes (E$||$c) for different temperatures above and below T_c [38].

Using the Josephson's equations and introducing a dimensionless time variable $t \rightarrow \omega_{JP}t$, the above expression reduces to a second-order differential equation of the phase difference,

$$\Delta\ddot{\varphi} + \beta_c\Delta\dot{\varphi} + \sin\Delta\varphi = \frac{I}{I_c} \qquad (1.39)$$

Where the parameter $\beta_c = \omega_{JP}RC$ determines the damping. In the limiting case of small amplitudes, $\sin\Delta\varphi \approx \Delta\varphi$, the characteristic frequency is defined as $\omega_{JP} = \sqrt{2eI_c/(\hbar C)} = 1/\sqrt{L_0C}$, and corresponds to the resonance frequency of an undamped oscillator circuit. The plane wave solutions of eq.(1.39) are a plasma oscillations (longitudinal waves), with the electric current and field oriented normal to the barrier. The oscillatory behaviour can be understood in terms of an exchange between the inductive and capacitive energy terms.

The frequency of the Josephson plasma modes is related to the superfluid density, ρ_s as $\omega_{JP}^2 \propto \rho_s$. In conventional superconductors both uncondensed normal carriers and the superconducting fluid participate in the plasma response, therefore signatures of the low-density superconducting plasma are difficult to detect. However, in layered superconductors, like high-T_c cuprates, since the normal-state transport along the c-axis is insulating, no metallic plasmon is visible in that direction. Therefore, at $T < T_c$ when superconducting tunnelling sets in, distinctive features appear, reflecting the superconducting plasma alone, see Fig. (1.9). For most cuprates an interlayer

25

superconducting plasma mode is observed at GHz–THz frequencies [39]. This makes THz spectroscopy an ideal tool to observe the superconducting state. In the following chapter I give a qualitative overview of high-T_c cuprates, followed by a discussion on $La_{2-x}Ba_xCuO_4$ and its phase diagram.

2 The Cuprate La$_{2\text{-}x}$Ba$_x$CuO$_4$

2.1 Discovery and Background

Till the mid-1980s the highest attained transition temperature for superconductors, observed in Nb$_3$Ge, had been languishing at 23 K. The discovery of superconductivity in La$_{2\text{-}x}$Ba$_x$CuO$_4$ (LBCO) by Bednorz and Müller in 1986, revitalized the field of superconductivity [40]. It was the first observation of a material having a T$_c$ above 30 K and led to a new classification of superconductors—materials with T$_c$ above 30 K are classified as high-T$_c$ superconductors. Their discovery was motivated by research in mixed valent complex oxides showing a Jahn-Teller (JT) polaron formation which could account for strong electron-phonon coupling and consequently a higher T$_c$. Complex metal oxides show a strong JT effect—where a molecular complex exhibiting an electronic degeneracy will spontaneously structurally distort to remove or reduce the degeneracy. If the stabilization energy associated with a JT distortion is comparable to the bandwidth of the material it will lead to electron localization and the formation of JT polarons. Therefore, they hoped that by doping JT active sites into a cubic perovskite (ABX$_3$) lattice, these polaronic centers might pair and superconductivity may emerge.

In late 1985, Müller became aware of the compound Ba-La-Cu oxide, which had all the prerequisites that they were looking for—perovskite-type structure with Cu showing two different valencies[21]. By varying the La/Ba ratio in different samples they were able to measure the onset of resistivity drop at 35 K. Bednorz and Müller cautiously

---

[21] Cu^{3+} is a non-JT ion as it has one hole in each of its two 3d orbitals with e$_g$ symmetry, on the other hand Cu^{2+} has one hole which could go to either of the two e$_g$ orbitals. In this case the degeneracy is broken through a structural distortion (JT-effect).
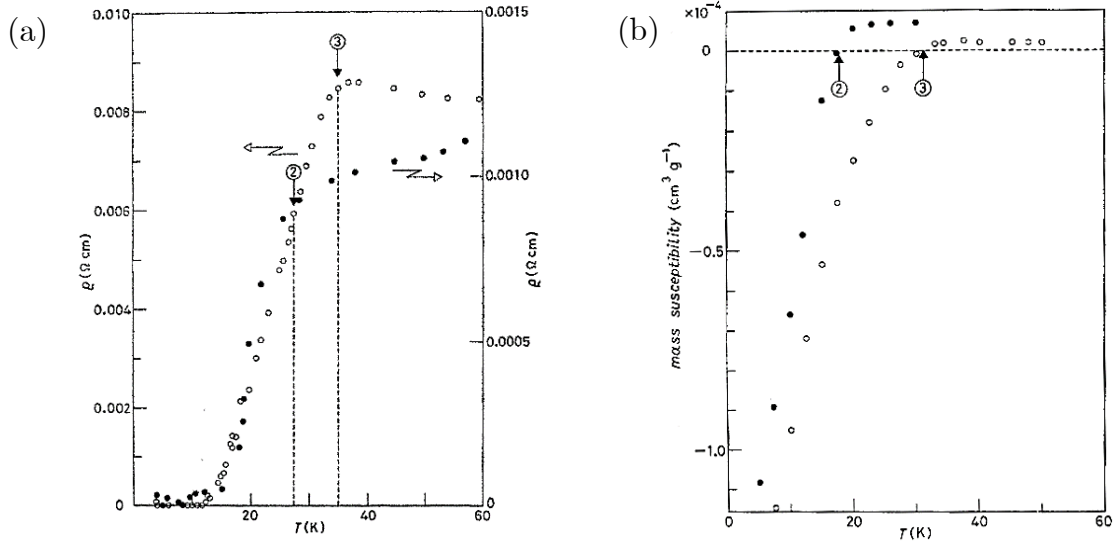
Figure 2.1 First reported (a) Resistivity and (b) Suspectibility of La$_{2-x}$Ba$_x$CuO$_4$ samples [41].

published their results under the heading "Possible High Tc Superconductivity in the Ba-La-Cu-O System" [40]. Through subsequent X-ray analysis, resistivity, and susceptibility measurements they could identify the Ba doped La$_2$CuO$_4$ as the superconducting compound which had a layered perovskite-like structure of K$_2$NiF$_4$ type.

The discovery of superconductivity in LBCO was a shot in the arm for superconductivity as it paved the way for discovery of related layered copper oxide superconductors (cuprates) with T$_c$'s above liquid N$_2$, see fig. 2.2. In 1987, Bednorz and Müller were awarded the Nobel prize in Physics "*for their important break-through in the discovery of superconductivity in ceramic materials.*"[42]

Since the discovery of superconductivity in cuprates, other families of superconducting materials have also been discovered, but as is visible in fig. 2.2 their maximum T$_c$ is still far below that of cuprates. It is ironical to find cuprates superconducting as they are very poor conductors at room temperature and as we will see later, the parent (undoped) materials are insulating antiferromagnets. As superconductivity arises out of mediated attractive interaction between electrons, while magnetism arises from strong repulsive interactions between electrons, it would appear that these two forms of order are antithetical to each other.
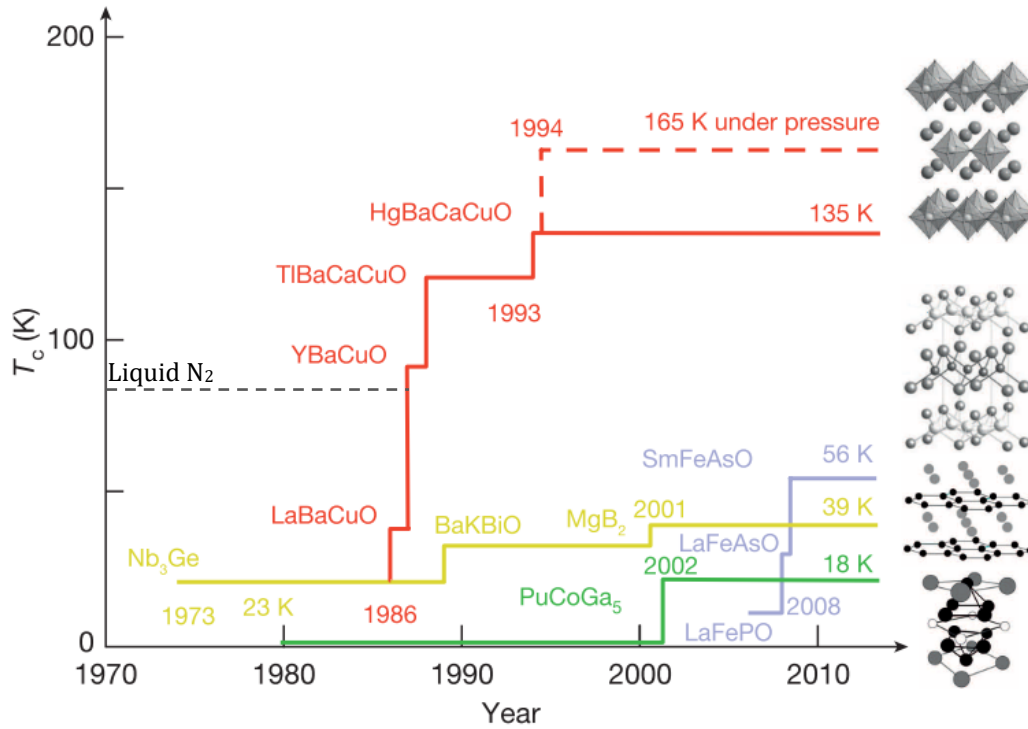
Fig 2.2 Transition temperature versus year of discovery for different families of superconductors [43].

Unfortunately, BCS theory has proved inadequate to explain the mechanism for superconductivity observed in cuprates, as solely electron-phonon coupling cannot account for such high T$_c$. Till date high temperature superconductivity remains as one of the most consequential open problems in physics. However, I will outline some salient universal features of cuprates which stem from the high transition temperatures and strongly layered crystal structure.

Cuprates share a common layered structure comprising of atoms sandwiched between CuO$_2$ layers. This results in highly anisotropic transport and magnetic properties, that approach the 2D behaviour expected from a stack of decoupled superconducting film planes. Using the Lawrence and Doniach (LD) formalism, cuprates can be viewed as two-dimensional layered materials with superconducting CuO$_2$ planes which are weakly coupled via Josephson tunneling through insulating barriers, see fig. The superconducting order parameter, $\psi_n = |\psi_n|e^{i\varphi_n}$ is suitably described if we consider a constant order parameter amplitude throughout the material and a set of phases $\{\varphi_n(x, y, t)\}_{n=1,...,N}$ in which each phase $\varphi_n(x, y, t)$ describes the phase difference of the Josephson junction made of two neighboring superconducting layers.

29

Figure 2.3 Cuprates can be modelled as stacks of 2D superconducting films. Experimental I–V characteristics of a bulk BSCCO sample below T$_c$ [39,44].

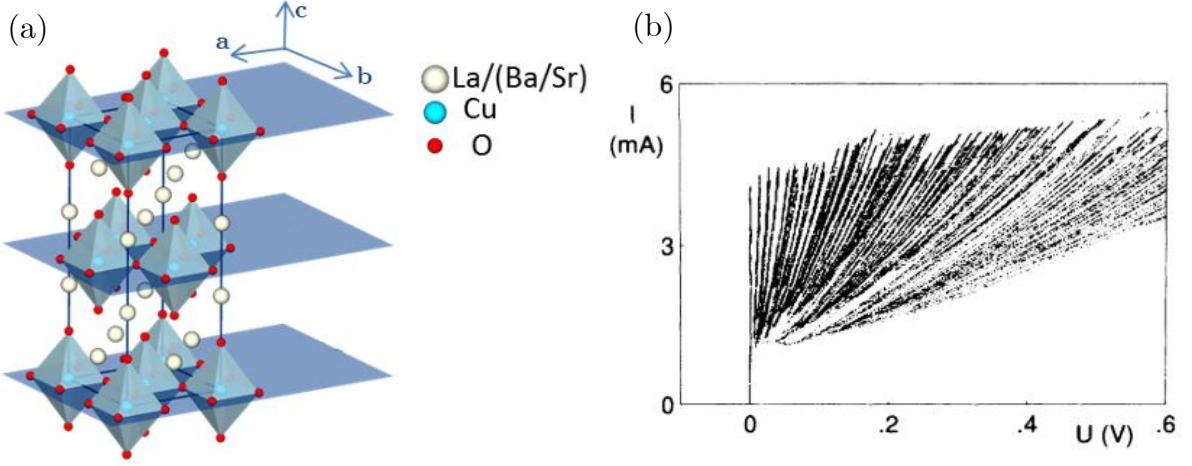Current–voltage (I–V) measurements along the c-axis of Bi$_2$Sr$_2$CaCu$_2$O$_{8+\delta}$ (BSCCO) and other high-T_c cuprates have detected signatures of Josephson tunneling. Crucially, the observation of multiple branches in the I–V curves, as shown in fig. 2.3, is characteristic of the response of a stack of Josephson junctions connected in series [39].

The superfluid density ρ_s parametrizes the rigidity of the superconducting order parameter. Cuprates have anomalously low superfluid density are thus characterized by small phase stiffness and poor screening. This implies that phase fluctuations play a significant role in cuprates. We can identify two temperatures, one associated with the fluctuations of the phase $T_\theta \approx \rho_s/m^*$ where m^* is the effective mass and the other $T_c \approx 0.5\Delta_0/k_B$ is associated with the Cooper pair binding energy, where Δ_0 is the average superconducting gap and k_B is the Boltzman constant. In a BCS superconductor, $T_\theta \gg T_c$ therefore fluctuations of the phase of the superconducting condensate are unimportant, once Cooper pairs form they immediately condense. On the other hand in cuprates, since $T_\theta \approx T_c$ thermal fluctuations of the phase play a crucial in determining the actual superconducting transition temperature. In cuprates, it is postulated that pairing and coherence are decoupled. Pairing happens at a temperature much higher than T_c. At T_c the phase locks to form a long-range ordered superconducting state [43,46]. In the sections ahead we will see the physics of the of the phase fluctuations is intertwined with that of the competing order.
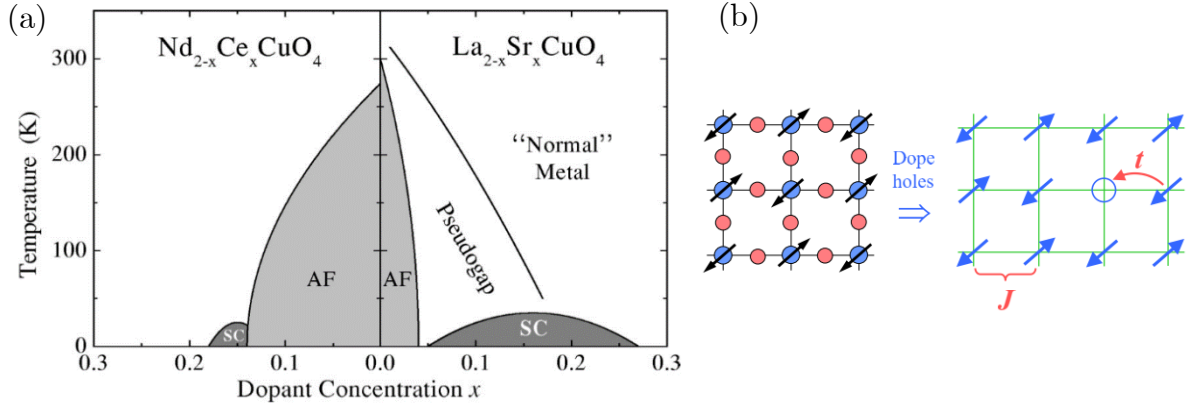
Figure 2.4 (a) Phase diagram for electron and hole doped cuprates as a function of doping (b) The left-hand side depicts the electronic structure of CuO_2 plane - magnetic moments of the Cu ions (blue) surrounded by Oxygen ions (red). Right-hand side shows the dominant interactions for a doped Mott insulator [45].

2.2 Parent Compound: La_2CuO_4

In the copper-oxygen (Cu-O) layer, Cu^{2+} ion is doubly ionized and in a d^9 configuration with each Cu having six O neighbours. The Cu^{2+} ion has one hole which can go into either of the two e_g orbitals, however due to the Jahn-Teller distortion which results in the CuO_6 octahedra being elongated along the c axis, this degeneracy is removed with the $d_{x^2-y^2}$ orbital being the highest partially filled orbital. As a result, the electronic structure of Cu-O planes involves hybridization of the Cu $d_{x^2-y^2}$ orbitals with planar-coordinated $2p_x$ and $2p_y$ O orbitals[22]. From tight-binding model we would expect La_2CuO_4 to be metallic which contrasts with the undoped compounds observed to being insulators. The physics of the system can instead be understood in terms of the Hubbard model which takes into account not only the kinetic energy of the electrons, as done by conventional band theory, but also the Coulomb interaction U between two electrons on the same site. An electron can reduce its energy by an amount t by hopping from one site to the next[23]. When the on-site Coulomb repulsion, U, dominates over the hopping energy, t, the electrons are localized, and the ground state is a Mott

---

[22] This will help explain the polarization dependence of the XAS measurements in the following sections as X-rays with the electric field parallel to the Cu-O plane (ab plane) are more sensitive to the doped-holes, as they probe states in the in the Cu-O plane.

[23] The hopping term, t, is proportional to the band width, W.

insulator. The half-filled band split into two, separated by the energy U with the lower lying band (lower Hubbard band, LHB) being completely filled while the higher lying one, the upper Hubbard band (UHB) is empty.

However, an electron can still lower its kinetic energy by making a virtual hop to a nearest-neighbor site and back again, though due to the Pauli exclusions principle, it can only hop if its spin is antiparallel to that of an electron already on the neighboring site. The effective Heisenberg exchange energy between neighboring antiparallel spins corresponds to the superexchange energy $J = 4t^2/U$.

Therefore, the fundamental problem of high-temperature superconductivity in hole-doped copper-oxide compounds is to understand the competition between antiferromagnetic spin correlations, arising out of strong Coulomb interactions and kinetic energy of doped carriers which favour delocalization.

The superexchange interaction is mediated via the oxygen atom which we have excluded in the above picture. Zaanen, Sawatsky and Allen provided a more accurate description of the parent cuprate compounds and categorized them as charge-transfer insulators [47]. If d_i^n indicates n electrons in the d states of the site i, then the Coulomb energy U associated with a Mott excitation can be denoted as a $d_i^n d_j^n \boxed{\leftrightarrow} d_i^{n-1} d_j^{n+1}$. In addition, we need to consider a charge transfer between a metal atom and a ligand site L (the ligands are oxygen in our case). The charge transfer excitation, with energy Δ, can be written as $d_i^n \boxed{\leftrightarrow} d_i^{n-1} \underline{L}$, where $\underline{L}$ is a ligand hole. When $\Delta < U$, the gap corresponds to Δ rather than U, as depicted above in the figure, and the material is charge-transfer insulator.

Uchida et al. reported optical conductivity measurements on single crystals of LSCO at various dopings at room temperature [48]. From fig we can see that La$_2$CuO$_4$ is an insulator with a gap of ~ 2 eV. With increase in doping, we introduce states in the charge transfer gap and eventually at higher dopings the conductivity evolves into a Drude peak.
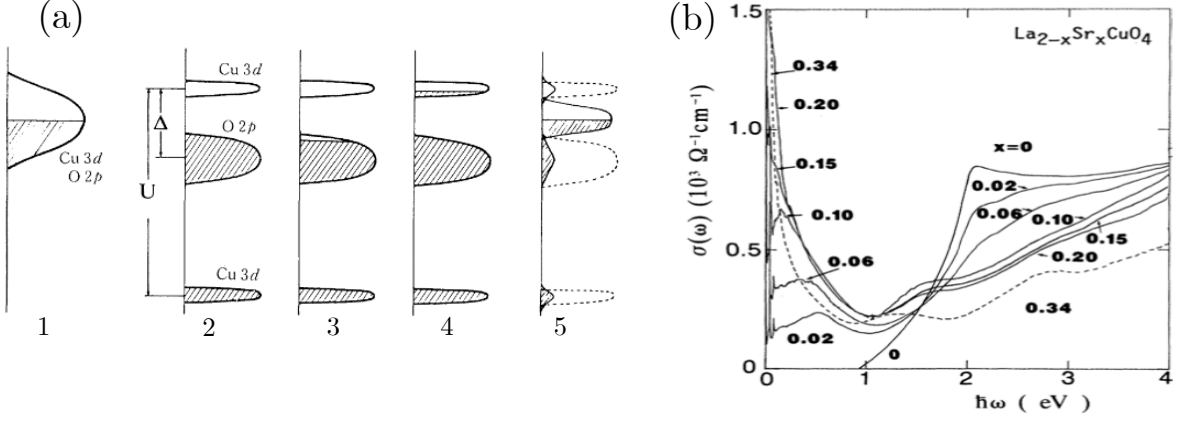
Figure 2.5 (a) Effective densities of states for undoped (1,2) and doped (3-5) CuO$_2$ planes. (1) Expected Fermi liquid band picture. (2) Charge-Transfer (CT) insulating state with split Cu 3d bands due to onsite coulomb repulsion U. The O 2p band is separated by a charge transfer energy Δ from the upper Cu 3d band. Rigid CT energy bands (3) and (4) for hole and electron doping. (5) mid-gap states inferred from experiments. (b) In-plane optical conductivity for La$_{2-x}$Sr$_x$CuO$_4$. Figures from [49].

In cuprates superconductivity emerges on chemically doping the parent compounds. In the case of La$_2$CuO$_4$ on substituting trivalent La by divalent Ba leads to holes being added to the Cu-O plane and is known as hole doping[24]. On the other hand, doping Nd$_2$CuO$_4$ with Ce^{4+} leads to electrons being added to the Cu-O plane and is thus called electron doping. In Fig. 2.4 (a) the phase diagram, as a function of doping, for both hole-doped and electron-doped cuprates is shown. Though the phase diagrams for the two kinds of dopings are similar, there is an apparent asymmetry. However, as the subject of our investigation is a hole-doped cuprate I will refrain from elaborating on the electron-doped phase diagram.

On the hole-doping side as seen in Fig. 2.4(a), Cu^{2+} spins in undoped La$_2$CuO$_4$ order antiferromagnetically with a Neel temperature T$_N$ of approximately 300 K. However, antiferromagnetic order is rapidly suppressed and destroyed by 2-4% hole concentration. After the suppression of the antiferromagnetic order, superconductivity appears, ranging from 6-25% doping. In the superconducting regime T$_c$ shows a dome

---

[24] We can resort to ionic valence counting to get a sense of charge distribution in cuprates. (La^{3+})$_2$(Cu^{2+})(O^{2-})$_4$ the parent compound is neutral. However, CuO$_2$ has a charge of 2−, which implies that the CuO$_2$ planes pull charge away from the La$_2$O$_2$ layers. Substituting La^{3+} with Sr^{2+} or Ba^{2+} we are reducing the charge in the system and effectively removing electrons from (or adding holes to) the CuO$_2$ planes.

shaped variation with respect to doping and the doping concentration (c)   x=x$_m$ which shows the maximum T$_c$ is referred to as optimal doping while the   region x<x$_m$ and x>x$_m$ is the underdoped and overdoped region, respectively. The region above T$_c$ on the underdoped side is called pseudogap and though thoroughly investigated is not very well understood. Pseudogap represents a region where there is depletion of density of states near the Fermi surface and the Fermi surface is partially gapped to both spin and charge excitations. In the overdoped regime the material crosses over to conventional Fermi liquid behaviour. In the following sections I will be discussing the incipient orders that arise in the pseudogap regime.

2.3 The 1/8 Anomaly in LBCO

Soon after the discovery of high-temperature superconductivity in La$_{2-x}$Ba$_x$CuO$_4$ studies showed a strong suppression of the T$_c$ centered around 1/8th (12.5%) doping [50,51]. This is surprising as its sister compound LSCO which is also doped with divalent Sr ions, shows only a slight kink in T$_c$ at this doping, see Fig. 2.6(a). The suppression of superconductivity in LBCO is referred to as the 1/8th anomaly and suggests the existence of a competing order.

X-ray diffraction studies by Axe et al. revealed a distinction between LBCO and LSCO [51]. The CuO$_6$ octahedra that make up the CuO$_2$ planes show no average tilting at high temperatures. On cooling down there is a second-order phase transition to a low-temperature-orthorhombic (LTO) phase, where the octahedra rotate around [110] axes, which is diagonal to both the CuO$_2$ square lattice and the Cu-O-Cu bonds. As illustrated in Fig. 2.6 (c) in this tilt pattern there is no distinction between orthogonal Cu-O bonds. At even lower temperatures, LBCO undergoes a second transition to the low-temperature-tetragonal (LTT) phase, which is absent in LSCO. In the LTT phase, the tilt axis runs parallel to the square lattice and the Cu-O-Cu bonds. As a result, orthogonal Cu-O bonds are no longer equivalent. For a given CuO$_2$ layer, Cu-O-Cu bonds along one direction are perfectly straight, while those perpendicular to them are
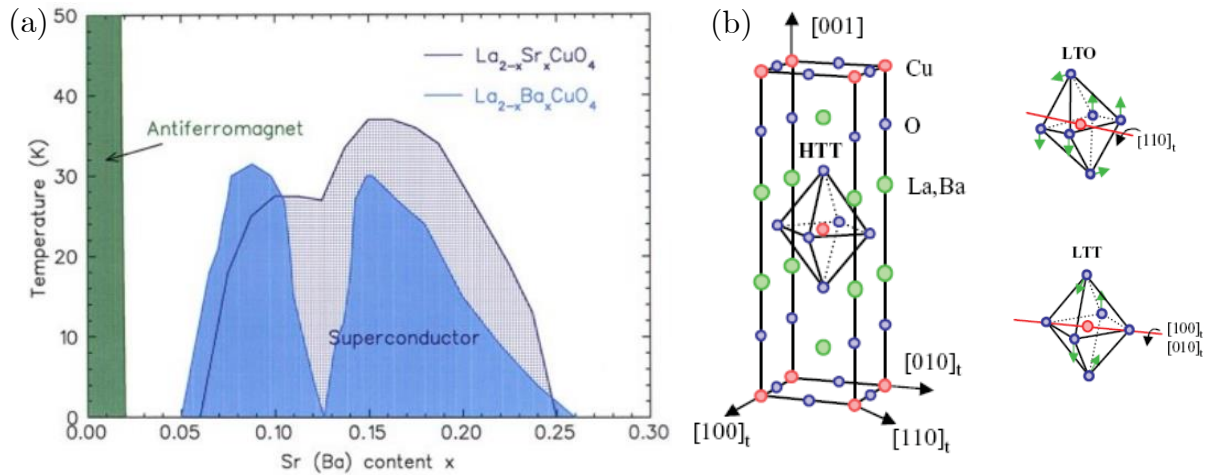
Figure 2.6 (a) Comparison of superconducting T$_c$ vs doping in LBCO and LSCO. (b) Unit cell of La$_{2-x}$Ba$_x$CuO$_4$ in the HTT phase. (c) Tilt directions of CuO$_6$ octahedra in LTO and LTT phase [50,52].

bent. Furthermore, the tilt axis of the octahedra is orthogonal in adjacent layers, alternating between [010] and [100] along the c axis. As we will see from the following section, the electronic order that emerges around 1/8th doping of LBCO mirrors the symmetry of the LTT phase. Therefore, the LTT phase plays a pivotal to pinning/stabilizing the order that competes with bulk superconductivity.

2.4 Stripes

The physics of the underdoped regime in hole-doped cuprates can be understood within the framework of the stripe model [47,53,54]. It was proposed that with the breakdown of antiferromagnetic order due to doping, phase separation takes place, with doped carriers spatially segregating into linear chains that separate antiphase antiferromagnetic domains, Fig. 2.7(b).

The mechanism is somewhat as follows. As opposed to a semiconductor, where doped charge distribution remains homogenous, in an antiferromagnet, doped holes form self-organized local inhomogeneities. The shape of this clustering is decided by the dimensionality of the system involved and for a D dimensional system you get (D-1) dimensional ordering. Consequently, in the case of 2D CuO$_2$ planes one expects the doped holes to have a 1D distribution. This inhomogeneous distribution arises because,

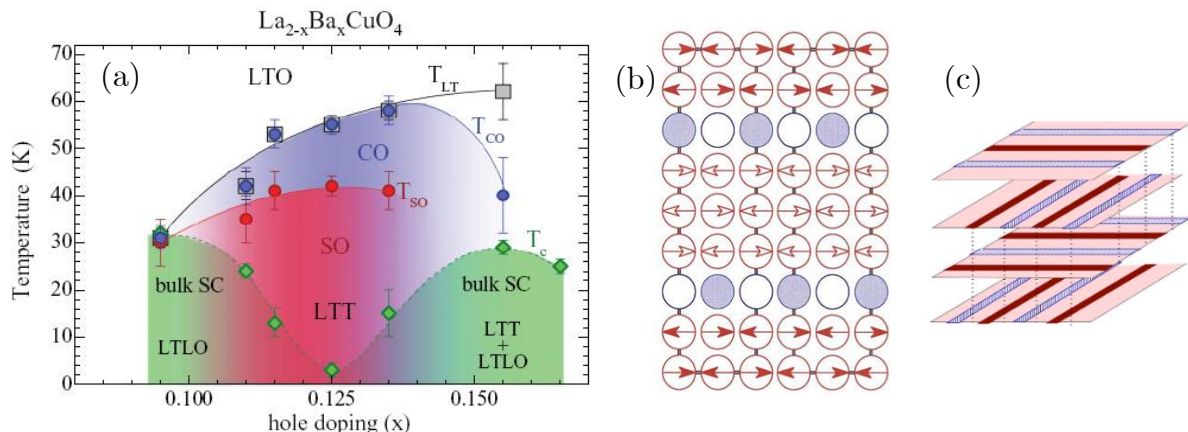Figure 2.7. (a) Temperature vs doping phase diagram of La$_{2-x}$Ba$_x$CuO$_4$. (b) Assumed stripe pattern in a hole-doped CuO$_2$ plane. Only Cu ions with their magnetic moments is represented. The spin rotates 180º on crossing a domain wall which is represented by the circles. A filled circle denotes the presence of a hole on metal site [23] (c) The stripe ordering in adjacent CuO$_2$ planes [3,52,55].

antiferromagnetic interactions among magnetic ions and Coulomb interactions between electrons favour localization of electrons, whereas the zero-point kinetic energy of the doped holes favours itinerant behaviour. Therefore, the best comprise between these competing interactions is achieved by having doped holes delocalized along linear stripes, while the region in-between them remains in the undoped antiferromagnetic insulating state, fig. 2.7. Thus, in the stripe phase we see the appearance of a spin and charge ordering, which can be observed by neutron and x-ray diffraction measurements.

In cuprates striped phase was first identified by neutron scattering[25] and x-ray measurements in La$_{1.6-x}$Nd$_{0.4}$Sr$_x$CuO$_4$ [3] and later confirmed in La$_{2-x}$Ba$_x$CuO$_4$ [56] and La$_{1.8-x}$Eu$_{0.2}$Sr$_x$CuO$_4$ [57], for doping x=12.5%. Figure 2.7 succinctly captures the relationship between spin/charge order, crystal structure and superconductivity for different dopings. Significantly, as shown in Fig. 2.7 spin and charge order in LBCO were shown to exist only after the transition to the LTT phase. While charge stripe order develops soon after transition to the LTT phase, spin order develops at a slightly lower temperature. Furthermore, it was also shown that the stripes lie along the direction of nearest neighbour bonds, implying that they are oriented along the Cu-O-

---

[25] Since neutrons have no charge, they do not scatter directly from the from the modulated charge distribution, but are instead scattered by the ionic displacements induced by charge modulation.

Cu bonds and the anisotropy of orthogonal Cu-O-Cu bonds in the LTT phase helps stabilize the stripes.

Since stripes mirror the symmetry of the LTT phase, stripes in adjacent planes are orthogonal to each other. Furthermore, in order to minimize Coulomb repulsion, the phase of the stripes is shifted by π as compared to their next-to-nearest neighbour layers, giving rise to two-fold periodicity along the c axis. The stacking arrangement of stripes consistent with the X-ray measurements is illustrated in Fig. 2.7.

On comparing the peak widths of charge order in- and out- of plane we can see there is a large anisotropy in correlations lengths. The correlation length of stripes in the CuO$_2$ plane is in the range of 200-250 Å and is isotropic. However, stripes are only weakly coupled perpendicular to the CuO$_2$ plane, with a correlation length of about 20-25 Å. To put this in perspective, the lattice parameters in the HTT phase are: $a_t = 3.78$ Å and $c = 13.2$ Å. Though there is big difference between the in- and out- of plane correlations lengths, charge order disappears isotropically with increase in temperature.

While neutron scattering measurements firmly established the existence of static spin order, charge order was on less sure footing, as the observed CO peaks can also arise from magnetoelastic coupling between the spins and the lattice. Another widely used technique, non-resonant x-ray scattering is mainly sensitive to the core electrons and it too measures the associated lattice distortion due to charge ordering. Therefore, both techniques are inadequate to address the question of whether stripe order involves ordering of the doped holes.

This question has been successfully addressed using resonant soft x-ray scattering (RSXS) where the incident x-ray photon energy is tuned to resonantly excite core electrons into the valence band. By tuning the x-ray energy to an absorption edge, the atomic scattering form factor is enhanced, therefore giving scattering measurements that are sensitive to specific atomic orbitals.
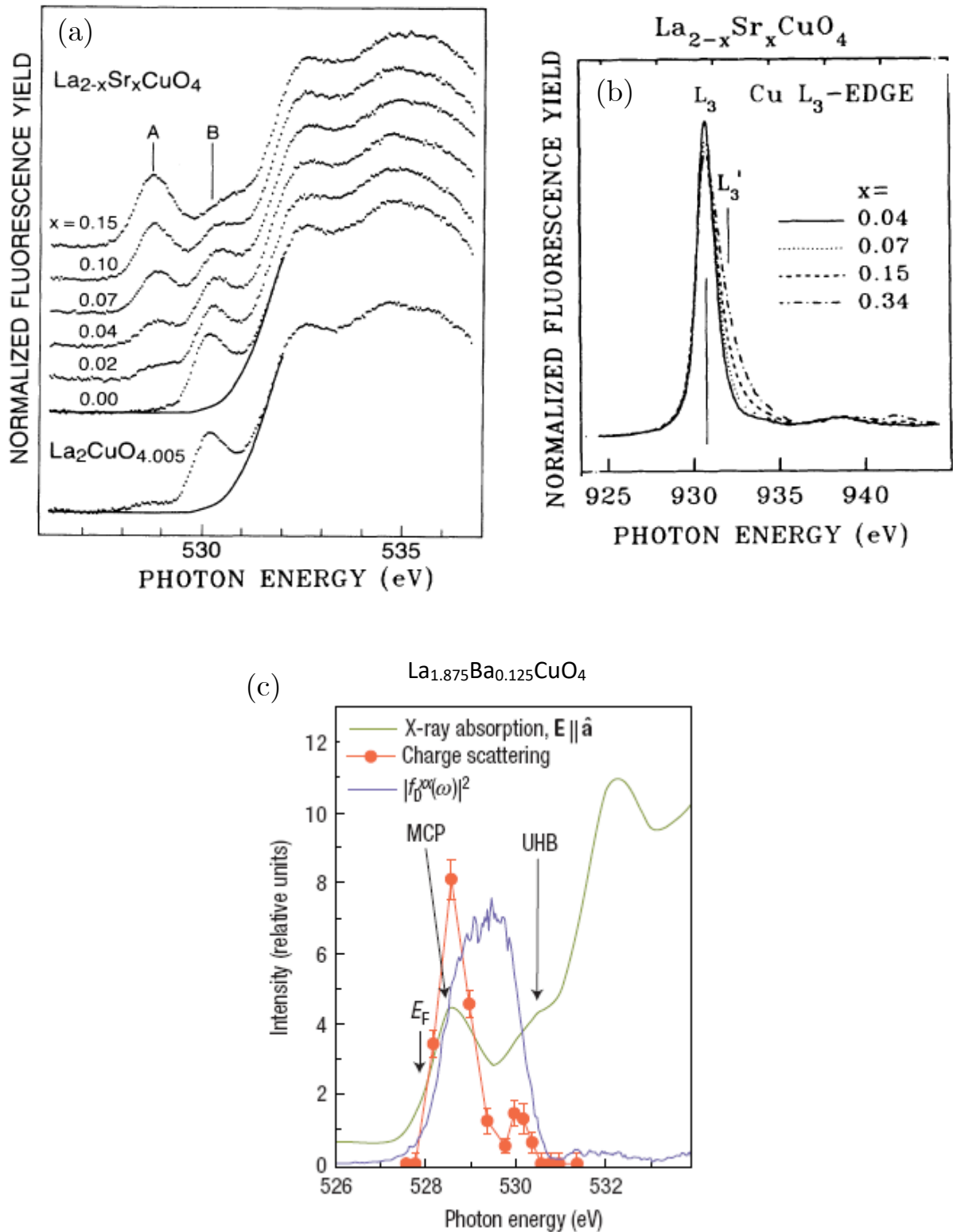
Figure 2.8 Normalized fluorescence yield at the (a) O K-edge and (b) Cu L$_3$ edge of La$_{2-x}$Sr$_x$CuO$_4$ (c) XAS spectrum of La$_{2-x}$Ba$_x$CuO$_4$ at the O K-edge highlighting the mobile carrier peak (MCP) and the 'upper Hubbard band' (UHB). $|f_D^{xx}|^2$ is the scattering length of the doped holes [58–60].

In cuprates, Cu 3d and O 2p orbitals dominate the density of states near the Fermi surface. The nominal electronic configuration of Cu-O for the parent compound is Cu $3d^9$ (one hole in $d_{x^2-y^2}$ band) O $2p^6$ (full p-band). However, the Cu-O bond is covalent and there is hybridization of the p-d orbitals, leading to a partial delocalization of the hole onto O. Since the energy required to add another hole on the Cu site is very large, U ∼ 9 eV, on doping the holes go primarily to the oxygen site but are strongly coupled antiferromagnetically via the superexchange interaction to holes on the Cu site.

Therefore, by studying the absorption edges which correspond to the valence electron ordering, the participation of doped holes in charge order can be ascertained. These edges correspond to the dipole-allowed, Oxygen K-edge (1s → 2p) and Copper L$_{3,2}$ edge (L$_3$: 2p$_{3/2}$ → 3d$_{x2-y2}$; L$_2$: 2p$_{1/2}$ → 3d$_{x2-y2}$). Oxygen K edge is at 543.1 eV and Cu L$_3$ and L$_2$ edge are at 932.7 eV and 952.3 eV, respectively, falling in the soft X-ray regime. The states corresponding to the L$_2$ edge are unaffected by doping and will not be discussed further.

X-ray absorption spectroscopy (XAS) on La$_{2-x}$Sr$_x$CuO$_4$ at O K edge is shown in Fig. 2.8(a). The spectrum shows two distinct pre-peaks (labeled A and B) observed at photon energies 528.8 and 530.3 eV. Both peaks show considerable doping dependence. Peak A results from doping induced holes and thus also referred to as "Mobile carrier peak" and the contribution is mainly from 3d$^9\underline{L}$ → $\underline{1s}$3d^9 transition. Peak B is associated with the "upper Hubbard band" and stems from 3d^9 → $\underline{1s}$3d^{10} transition of the undoped material, which is allowed due to the hybridization of 3d$^{10}\underline{L}$ and 3d^9 in the ground state. Here $\underline{L}$ and $\underline{1s}$ denote the O 2p$_{x,y}$ ligand hole and O 1s core hole, respectively. XAS on Cu L$_3$ edge reveals a slight reduction in intensity of the absorption edge on doping and a doping induced satellite peak (shoulder indicated as L$_3$') appears ∼ 1 eV above the main edge, Fig. 2.8(b). The contribution to the absorption edge comes from the transition mentioned above and the satellite peak is associated with 3d$^9\underline{L}$ → $\underline{2p}_{3/2}$3d$^{10}\underline{L}$ transition. Here $\underline{2p}$ corresponds to a hole being created in the p orbital of the Cu atom. Importantly as the valence states are polarized in the Cu-O plane, both

the Oxygen pre-peak and Cu *L* features seen in XAS are only observed for horizontal polarization of the X-rays, E||ab.

XAS on LBCO$_{1/8}$ shows identical features and from the above analysis it becomes apparent that the feature most sensitive to doped holes, is the mobile carrier peak. Indeed, RSXS studies on LBCO$_{1/8}$ by Abbamonte et al. found a strong resonance at both the mobile carrier peak and upper Hubbard band, Fig. 2.8 [60]. Thus, indicating that doped-holes are ordered in the striped phase.

Since stripe order is observed in the LTT phase, where the rotational symmetry of the CuO$_2$ planes is reduced from fourfold to twofold. How essential is the reduced lattice symmetry to existence of stripe order? High pressure x-ray diffraction measurements by Hücker et al. demonstrated that even on restoring the fourfold symmetry of LBCO, charge-stripe order still exists [61]. Thus, stripe correlations are electronically driven and do not depend on reduced lattice symmetry.

From the above observations we can conclude that the stripe phase is a spontaneous breaking of the translational and rotational symmetry of the system in the form of quasi-long-ranged, coexisting spin and charge order, which is driven by an instability in a strongly correlated system. In the next section we discuss the coexistence of the stripes and superconductivity and the emergence of a novel broken symmetry.

2.5 Superconductivity and Stripes

At first glance of Fig. 2.7(a) it may appear that superconductivity and stripes are competing orders. However, their relationship is quite nuanced. Resistivity and susceptibility measurements of LBCO$_{1/8}$ show highly anisotropic behaviour with the onset of the spin-stripe order. As illustrated in Fig. 2.9 (a) we see that the in-plane resistivity ρ_{ab} shows a large drop at 40 K, while the c-axis resistivity ρ_c remains unchanged. Also, the drop in ρ_{ab} coincides with a weak onset of 2D diamagnetism. Furthermore, as we approach 16 K, ρ_{ab} goes to zero although ρ_c remains comparatively large. These measurements suggest a 2D superconducting transition in the CuO$_2$ planes.
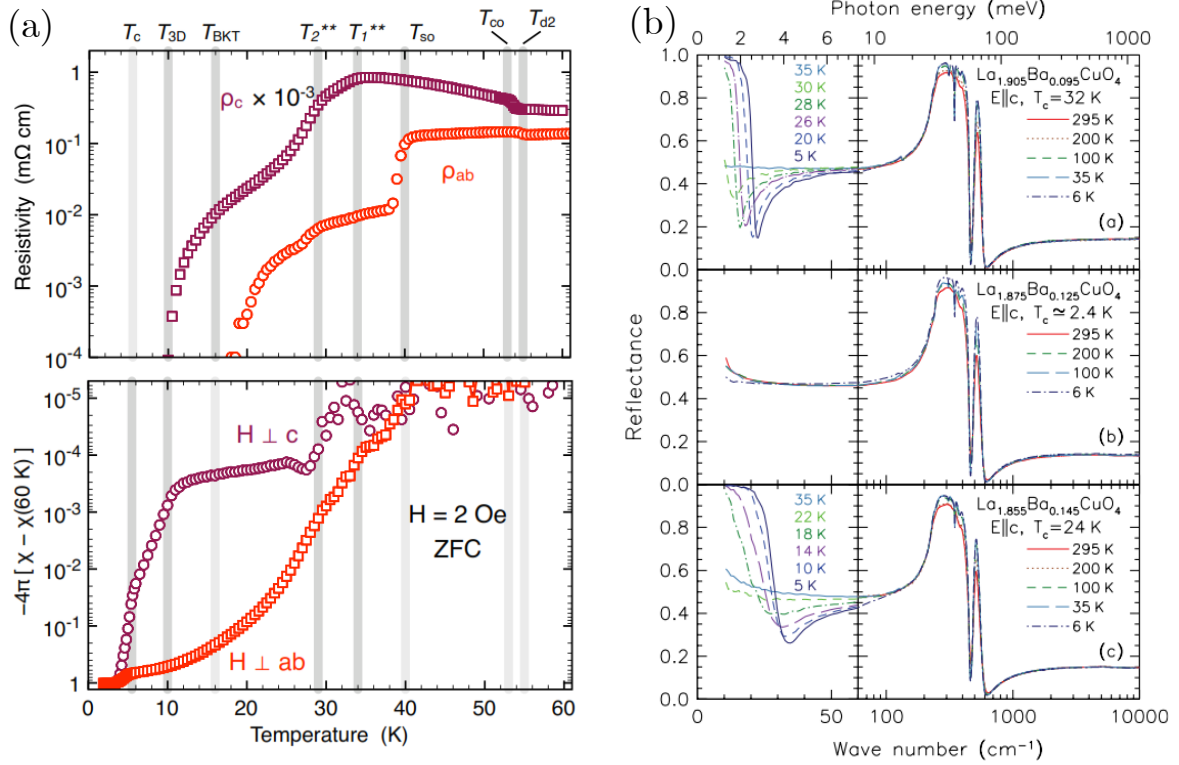
Figure 2.9 (a) (top) Resistivity and (bottom) magnetic susceptibility, in-plane and perpendicular to the planes [62]. (b) C-axis infrared reflectance measured in La$_{2-x}$Ba$_x$CuO$_4$ for different dopings [38].

The in-plane transport goes from linear to nonlinear regime, suggesting that the 2D superconducting order develops through a Berezinskii-Kosterlitz-Thouless transition. The appearance of 2D superconductivity without the observation of bulk 3D superconductivity is quite surprising, because, as soon as the in-plane superconducting correlations become large, Josephson coupling of the CuO$_2$ layers should lead to the emergence of 3D superconductivity. The absence of 3D order implies a frustration of Josephson coupling.

The decoupling of CuO$_2$ layers can be observed in the c-axis reflectance of LBCO$_{1/8}$. In Fig. 2.9 (b) for comparison reflectance along c-axis optical for three dopings is depicted. On relating these doping concentrations to Fig. 2.8 we see that LBCO for x = 0.095 and 0.145 is superconducting and below T$_c$ we see the appearance of a Josephson Plasmon resonance. LBCO$_{1/8}$ on the other hand does not undergo a superconducting transition down to 5K and thus we do not observe Josephson plasmon resonance in the material.
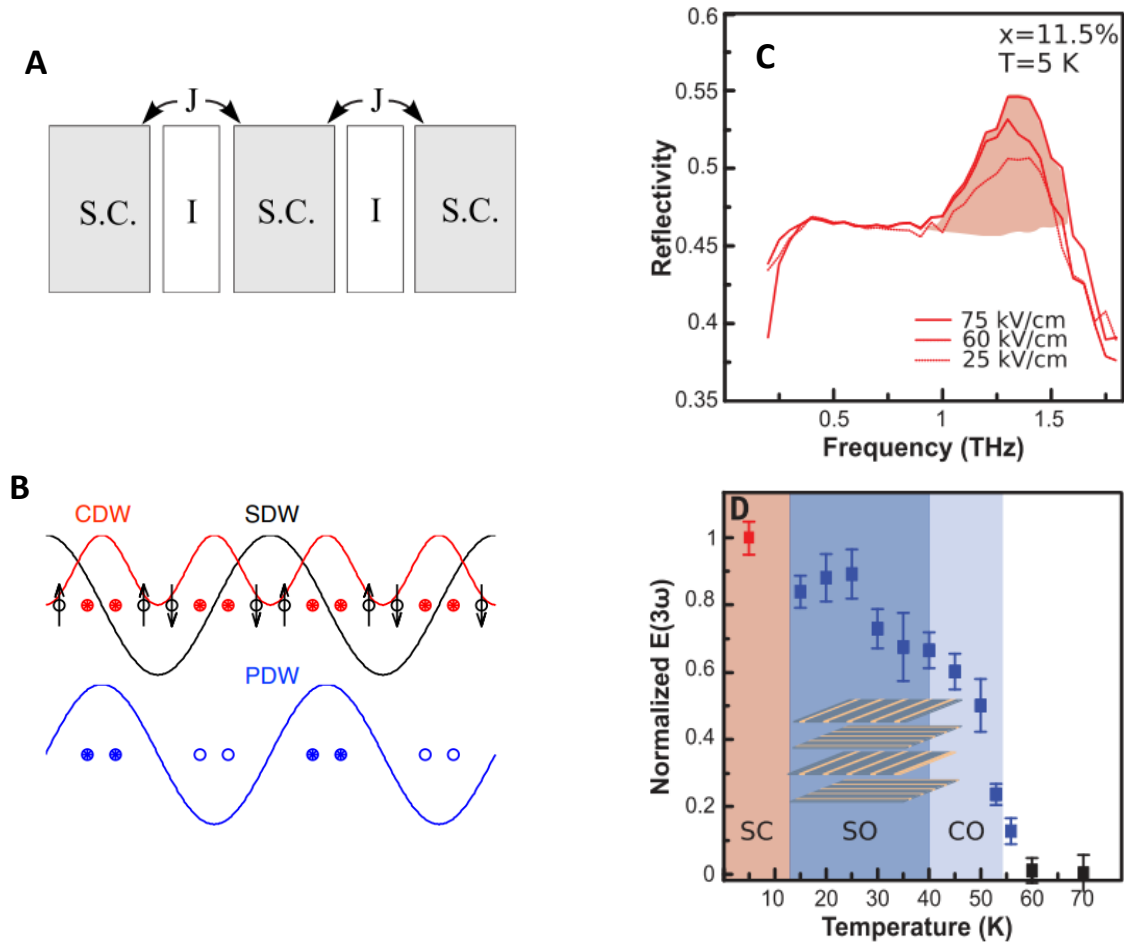
Figure 2.10. (A) Pair density Wave (PDW) superconductor can be modeled as a superconductor (SC) separated by insulating regions (I) forming a Josephson junction. (B) Schematic of charge density wave (CDW), spin density wave (SDW) and PDW orders, indicating the relationships among the phases of the modulations [63]. (C)Nonlinear frequency-dependent reflectivity measured in the striped La$_{1.885}$Ba$_{0.115}$CuO$_4$. (D) Temperature dependence of the third-harmonic signal (normalized to the highest field measurements at T =5 K) [64].

The above results suggest that stripe order is compatible with 2D superconducting correlations, however it leads to decoupling of the CuO$_2$ planes and therefore bulk superconductivity in the system is suppressed. Consequently, below the spin-ordering temperature, the phase is also described as a striped superconductor, where superconducting, charge and spin order parameters are closely intertwined with each other, rather than merely coexisting or competing.

Berg et al. proposed pair-density-wave (PDW) superconducting order to describe the physics of the striped superconductor [55,65]. As illustrated in Fig 2.10, a striped superconductor can be thought of as an array of superconducting regions (SC)

separated by insulating antiferromagnetic order (I), therefore forming extended superconductor-insulator-superconductor junctions. If the Josephson coupling across the insulating barrier is negative, favouring a π junction, then a striped superconducting phase is found. This leads to a spatially modulating SC order which changes sign between neighbouring stripes and goes to zero in the insulating region. The period of the PDW is same as that of the spin-order and twice that of the charge order. Furthermore, as stripes in neigbhouring CuO$_2$ layers are orthogonal to each other, the oscillations of the PDW superconducting order leads to the Josephson coupling between CuO$_2$ layers to be zero and thus we do not observe the emergence of bulk superconductivity in a striped superconductor.

This makes the PDW invisible to linear c-axis optical measurements as the stripe alignment causes the interlayer superconducting tunneling to vanish on average. However, the nonlinear optical response of the PDW is non-zero. Rajasekaran et. al. observed a giant terahertz third harmonic, characteristic of nonlinear Josephson tunneling, in La$_{1.885}$Ba$_{0.115}$CuO$_4$ above the transition temperature T$_c$ = 13 K and up to the charge-ordering temperature T$_{co}$ = 55 K, see Figs. 2.10(C) and Fig. 2.10 (D). These results are indicative of a pair density wave condensate in underdoped cuprates [64].

From the above discussion we can see that superconductivity emerges as a compromise between competing interactions in a Mott insulator. The underdoped regime is the battleground between various phases and interactions. The question as to exactly how and why superconductivity emerges from this cauldron has been one of the longstanding problems in physics for the past 30 years. In our effort to understand this puzzle we have endeavoured to study the underdoped cuprate La$_{1.885}$Ba$_{0.115}$CuO$_4$. In the following chapters I will describe the experimental techniques used in our investigations.

3 Introduction to Ultrafast Spectroscopy

3.1 Overview

The key to understanding the dynamics of a system is to be able to observe it motion, that is effectively see how it transforms from one state to another. With a digital camera if we want to capture a sharp image of a moving subject, we will typically need to play with shutter speed, aperture, and ISO[26] settings, in a way that the subject is effectively stationary for the duration of exposure tie. However, as the dynamics gets faster, simply changing the camera settings is insufficient to get a clear still frame. For example, if we would like to take the picture of a hummingbird hovering mid-air, and wish to 'freeze' its wings, reducing the shutter speed down to one thousandth of a second ($10^{-3}s$) won't help. As shown in Fig. 3.1(a) we will end up with a dark picture, since there isn't enough light entering the sensor, and it will still be blurry as there is some movement of the wings during the exposure time. To overcome this problem, we will need to use a flash, as it provides high intensity light over a very short duration, much shorter than any mechanical shutter can function. This will allow us to increase the exposure time, allowing enough light to enter the sensor, while simultaneously freezing the wings as they are motionless for the duration of the flash, Fig. 3.1(b). This stroboscopic technique illustrates how intensity and duration of the flash, determines the timescale of the motion we can capture. The above analogy gives a sense of ultrafast spectroscopy, where light sources having extremely high intensity over a duration shorter or comparable to the phenomena being investigated are used to capture,

---

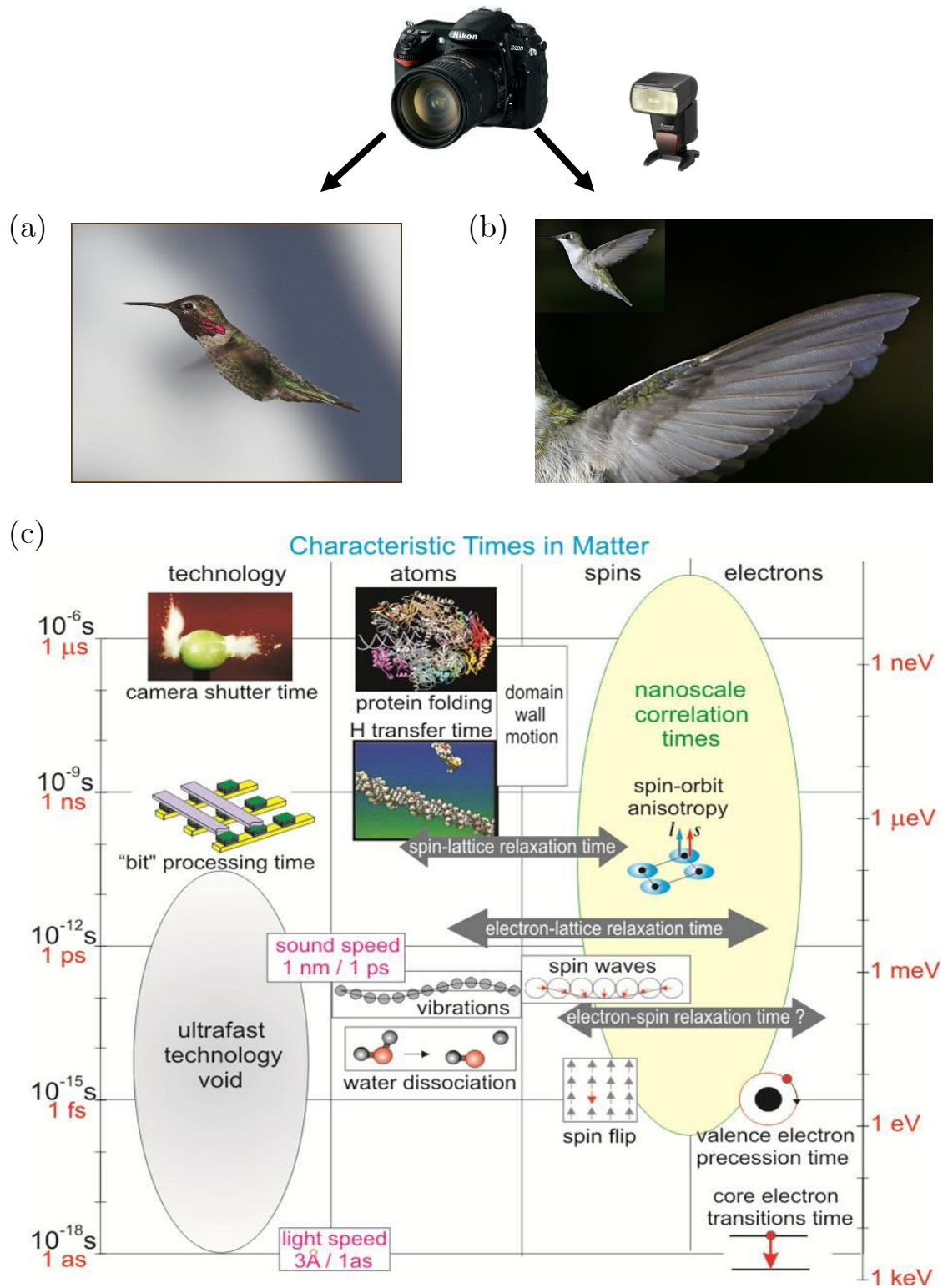[26] Sensitivity of the image sensor - CCD.

45

Figure 3.1 a) Picture of a hummingbird taken with shutter speed of 1/1000 s b) Picture taken with a flash 1/20,000 s and shutter speed 1/200 s. c) Characteristic energy and timescales in matter. Adapted from [66].

understand, and manipulate the dynamics of the quantum world. As shown in Fig. 3.1(c) both, from understanding the fundamental physics of phenomena and a technological point of view the picosecond to femtosecond ($10^{-12} - 10^{-15} s$) timescale is of high relevance.

Quantum materials are characterized by competing spin, orbital and lattice interactions, resulting in a phase diagram with multiple co-existing/competing phases and collective modes from broken continuous symmetries. In response to a weak external stimulus, these phases can rapidly transform from one to another. Phase transitions showing: Insulator ⇌ Metal, Insulator ⇌ Superconductor, Paramagnet ⇌ Magnet, have been observed in quantum materials [67]. Therefore, by developing the ability to controllably manipulate their phases, we can develop a number of technological applications from them [68].

3.2 Pump-Probe Technique

The invention of femtosecond lasers with solid state gain medium, like titanium-doped sapphire (Ti:sapphire), was truly transformational for ultrafast spectroscopy. In comparison to previous dye-lasers, Ti:sapphire lasers are highly stable, have low noise and provide turnkey operation, thus being a perfect light source for investigating subtle transient phenomena on a femtosecond timescale.

The workhorse of ultrafast spectroscopy is the pump and probe technique, where a laser beam is split into two – a pump and a probe beam. The pump beam provides the trigger, it photo-excites[27] the dynamics we wish to investigate, either by providing sufficient energy to the system to overcome a potential barrier or resonantly excite a particular transition/mode. The probe beam sequentially images the system at different time delays post the photoexcitation. This allows us to build a complete picture, a movie of sorts, of the phenomena we wish to investigate and watch the evolution of the

---

[27] I am using the term photo-excite in a general sense that is excitation by a femtosecond laser pulse. In literature, the term is used synonymously with excitation at 800 nm (1.55 eV).
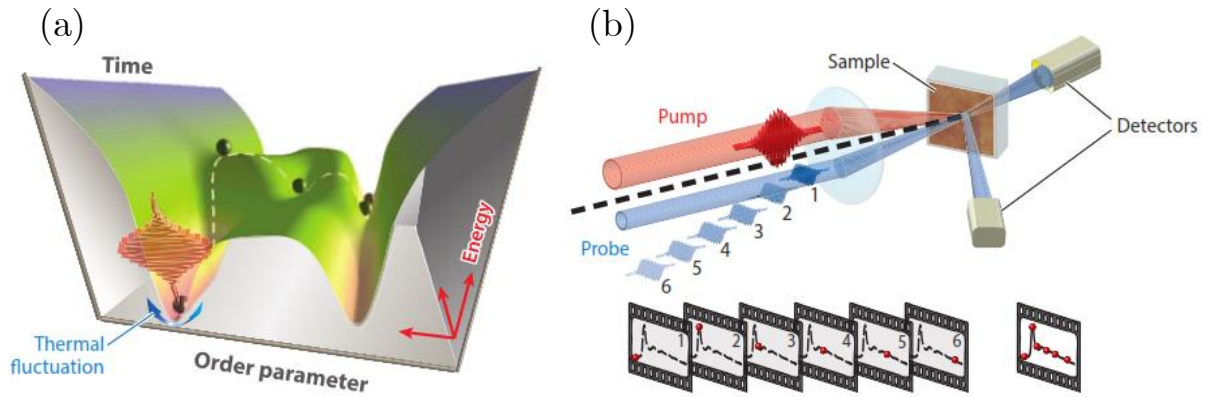
Figure 3.2 (a) Evolution of a photoinduced phase transition. (b) Schematic of a pump-probe setup used to temporally resolve the dynamics of a photoinduced state. A pump (red) pulse creates a nonequilibrium state. Snapshots (1-6) of the transient state are taken at different time delays by a probe (blue) pulse. Figures from [69].

system as it relaxes back into the ground state or transform into another phase. An illustration of a pump-probe setup is shown in Fig. 3.2(b). Using this template, we can construct more sophisticated ways to examine our sample.

Importantly, we are not restricted to the photon energy of the laser, which in the case of a Ti:sapphire laser is 1.5 eV ($\sim$820 nm). Due to the high field intensity of a laser pulse, the linear relationship ($P = \chi E$) between the polarization P induced in a medium and an external electric field E breaks down. In general, P can be expressed as a power series in E –

$$P = \chi^{(1)}E + \chi^{(2)}E^2 + \chi^{(3)}E^3 + \cdots + \chi^{(n)}E^n \,,$$

here $\chi^{(n)}$ is the nth order susceptibility of the material. For weak fields, the dominant contribution is $\chi^{(1)}$, however for strong fields the higher order terms, $\chi^{(n>1)}$ become relevant and this gives rise to nonlinear processes, which play an important role in ultrafast spectroscopy. Essentially, the nonlinear response of a material, allows the emission of a photon having a frequency different from the one incident. Also, as accelerating charges and time-varying currents radiate electromagnetic waves, we can

also create far-infrared radiation (THz) from biased photoconductive antennas[28] excited by laser beams. Therefore, by directing a laser beam through optical crystals and/or photoconductive antennas we can tune the wavelength to selectively probe or pump certain energy states of a system.

Furthermore, Ti:sapphire lasers are now often used in conjunction with x-ray Free Electron Lasers and 3rd generation synchrotrons. As the latter generate high intensity short pulses spanning the ultraviolet-to-hard x-ray regime, a number of time-resolved diffraction and photoemission techniques have been developed to study the effects of photo-excitation on photoemission and electronic/orbital/lattice ordering, among other things [67].

It was shown early on that intense laser pulses can nonthermally destroy the superconducting state [70,71]. Pump-probe studies in high-T_c superconductors have concentrated on studying the Cooper-pair breaking and quasiparticle relaxation dynamics in these materials. Shining eV-energy photons on a superconductor leads to Cooper-pair breaking and creation of quasiparticles, with excitation of electrons to unoccupied states above the Fermi-level. Thereafter, the photo-excited carriers relax to states near the Fermi level via intraband electron-electron scattering and electron-phonon scattering. In the next step quasiparticles recombine across the superconducting gap (Δ_{sc}) with emission of a boson with energy $\geq 2\Delta_{sc}$. Since, pair-breaking and quasiparticle recombination are related by time reversal symmetry, both processes are mediated by the same boson/s. Identifying, the boson mechanism for pairing is crucial to understanding and developing a theory for high-T_c superconductivity.

The scope of this thesis is qualitatively different because the goal of our work is to destabilize a coexisting or competing order and study the temporal evolution of the underlying suppressed superconducting state.

---

[28] A photoconductive antenna is a light switch consisting of metal electrodes deposited on a semiconductor substrate. They are discussed in greater detail in chapter 5.

4 Time resolved Resonant Soft X-ray Diffraction and Setup at I06 Beamline at Diamond Light Source

For over a century X-rays have been used to study the atomic and electronic structure of materials. With the advent of quantum materials where the ordering of charge, spin, orbital, and lattice degrees of freedom determine the electronic and magnetic grounds states, new experimental approaches with selective sensitivity to such ordering were required. Resonant X-ray scattering has proved to be a powerful technique in that sense allowing to measure new forms of electronic and magnetic order in materials. In this chapter, I start by describing light-matter interaction and lay the groundwork for diffraction and resonant X-ray scattering. Thereafter, I introduce synchrotron radiation and conclude with describing the experimental setup used to carry out time resolved resonant soft X-ray diffraction at the I06 beamline at Diamond Light source.

4.1 Semi-classical picture of X-ray scattering

Consider an electromagnetic wave with unit polarization vector $\boldsymbol{\epsilon}$ and fields,

$$\boldsymbol{E}(\boldsymbol{r}, t) = \boldsymbol{\epsilon} E_0 e^{-i(\omega.t - \boldsymbol{k}.\boldsymbol{r})}, \tag{4.1}$$

$$\boldsymbol{B}(\boldsymbol{r}, t) = \frac{1}{c}(\boldsymbol{k} \times \boldsymbol{\epsilon}) E_0 e^{-i(\omega.t - \boldsymbol{k}.\boldsymbol{r})}, \tag{4.2}$$

incident on a free electron (m_e) with charge $-e$ and spin s. The motion of the electron follows the oscillating electric field, creating an electric dipole moment [72]–

$$p(t) = \frac{-e^2}{m_e \omega^2} E_o e^{-i\omega t} \tag{4.3}$$

The dipole acts as a source of radiation and if we assume it to be a point source, the field of the radiation scattered/re-radiated from the dipole has a spherical wave form, $e^{ik.r}/r$ and is expressed as

$$E'(t) = \frac{\omega^2}{4\pi\varepsilon_o c^2} \frac{e^{ik'r}}{r} [k' \times p(t)] \times k' \tag{4.4}$$

where k' is the scattered wave vector. On substituting eq. (4.3) in (4.4) we get the scattered field for charge scattering

$$E'(t) = -\frac{1}{4\pi\varepsilon_o} \frac{e^2}{m_e c^2} \frac{e^{ik'r}}{r} [k' \times E(t)] \times k' \tag{4.5}$$

The negative sign implies that charge scattering introduces a phase shift of π between the incident and scattered fields.

Similarly, we can obtain the field scattered by the spin, s, of an electron/charge, by taking into account the associated magnetic field $B(r,t)$ which induces a magnetic moment $m(t)$. However, since we primarily look at charge scattering in cuprates, I will not be elaborating further on spin scattering.

From a practical point of view, it would be important to calculate the intensity of the radiation scattered from the free charges into a detector that subtends a solid angle $\Delta\Omega$. This quantity is defined as the differential scattering cross-section, with dimensions [Lenght^2/Solid Angle], given by

$$\frac{d\sigma}{d\Omega} = |f(\epsilon, \epsilon')|^2 \tag{4.6}$$

Here, ϵ' is the polarization of the scattered light and $f(\epsilon, \epsilon')$ is the polarization dependent scattering length, defined as

$$f(\epsilon, \epsilon') = -\frac{re^{-ik'r}}{E} E'.\epsilon'. \tag{4.7}$$

Then, the total scattering cross-section from the charge of a single electron also called the Thomson cross-section, is

$$\sigma_e = \int |f(\epsilon, \epsilon')|^2 \, d\Omega = r_o^2 \int_0^{2\pi} \int_0^{\pi} \sin^2\theta \, \sin\theta \, d\theta d\phi = \frac{8\pi}{3} r_o^2 \tag{40}$$

where $r_o = e^2/4\pi \, \varepsilon_o m_e c^2 = 2.82 \times 10^{-6}$ nm is the classical electron radius or the Thomson scattering length.

The next step in complexity is to study scattering from a multi-electron atom. From the above treatment we can assume the total scattered amplitude as the sum of amplitudes of individual electrons. However, since the atom is of finite size, depending on which electron scatters, there would be a small path length differences in the travel of the scattered radiation to the detector. This leads to interference effects, which are taken into account by the atomic form factor, $F^o(Q)$, defined as [72,73]

$$F^o(Q) = \int \rho(r) e^{iQ.r} \, dr \tag{4.9}$$

Here ρ is the charge density in the atomic volume and $Q = k' - k$ is the associated momentum transfer in the scattering process. In the limit $Q \rightarrow 0$ all the volume elements scatter in phase and $F^o(Q) = Z$, the number of electrons in the atom. The atomic form factor $F^o(Q)$ defined in eq. (4.9) can also be defined as the Fourier transform of the charge density of the atom. The scattering length of the atom, $f_{atom}(Q)$, is given by the Thomson scattering length r_o times the atomic specific form factor times the polarization factor

$$f_{atom}(Q) = r_o F^o(Q) \epsilon.\epsilon' \tag{4.10}$$

Baring Free Electron Laser (FEL) X-ray sources, the x-ray intensity at present synchrotrons is insufficient to produce a measurable signal from the scattering cross-

section of atoms and molecules. Therefore, in order to amplify the scattered intensity and get a good signal to background ratio, it is necessary to bring the numerous scattering elements together and assemble them into crystals.

4.2 Crystal Diffraction

The lattice of a crystal is the periodic arrangement of atoms, molecules or ions in three dimensions. Owing to the translational symmetry of the system we can define a vector R_n which spans the entire lattice. Such a vector is called a primitive lattice vector and defined as

$$R_n = n_1\boldsymbol{a_1} + n_2\boldsymbol{a_2} + n_3\boldsymbol{a_3} \quad ; \boldsymbol{n_1}, \boldsymbol{n_2}, \boldsymbol{n_3} \in \mathbb{Z} \tag{4.11}$$

Where $\boldsymbol{a_1}, \boldsymbol{a_2}, \boldsymbol{a_3}$ are the basis vectors of the lattice and $\mathbb{Z}$ is the set of integers. If r_j is the position of jth element in the lattice, then the position of any element in the crystal is given by $R_n + r_j$. Therefore, summing over the individual atomic form factors, the scattering length for a crystal, $F^{crystal}(Q)$, can be written as [73]

$$F^{crystal}(Q) = r_o.(\epsilon.\epsilon') \overbrace{\sum_{r_j} F_j^o(\boldsymbol{Q}) e^{iQ.r_j}}^{\substack{\text{Unit cell structure} \\ \text{factor}}} \overbrace{\sum_{R_n} e^{iQ.R_n}}^{\text{Lattice Sum}} \tag{4.12}$$

where we factorized the scattering amplitude of a crystal into two parts. The first term under the summation operator is called the unit cell structure factor with $F_j^o(\boldsymbol{Q})$ being the atomic form factor of the jth atom. The second term is a sum over all lattice sites. For a non-vanishing $F^{crystal}(Q)$, it is required that

$$\boldsymbol{Q}.\boldsymbol{R_n} = 2\pi \times integer \tag{4.13}$$

In which case the, lattice sum becomes of the order N, with N being the number of unit cells. For eq. (4.13) to be fulfilled it can be shown that $\boldsymbol{Q} = \boldsymbol{G}$, where G is the reciprocal lattice vector, defined as

$$\boldsymbol{G} = h\boldsymbol{a_1^*} + k\boldsymbol{a_2^*} + l\boldsymbol{a_3^*} \quad ; \boldsymbol{h}, \boldsymbol{k}, \boldsymbol{l} \in \mathbb{Z} \tag{4.14}$$
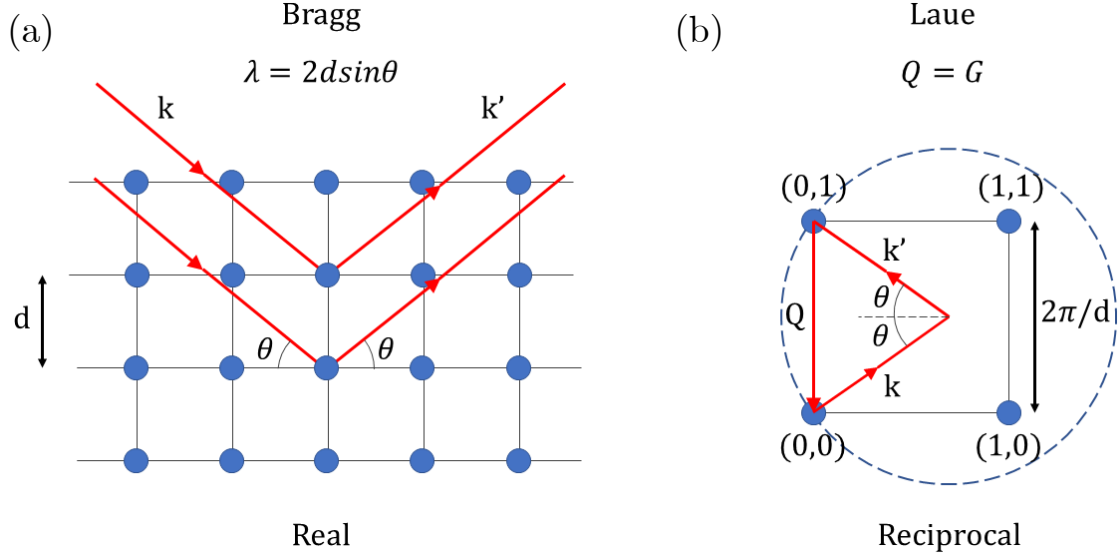
Figure 4.1 (a) Bragg diffraction in real space and (b) Laue condition in reciprocal space. These descriptions are equivalent. See footnote 28.

and spanned by the reciprocal lattice basis vectors $\boldsymbol{a_1^*}, \boldsymbol{a_2^*}, \boldsymbol{a_3^*}$ and constructed in terms of the basis vectors $\boldsymbol{a_1}, \boldsymbol{a_2}, \boldsymbol{a_3}$ −

$$\boldsymbol{a_1^*} = 2\pi \frac{\boldsymbol{a_2} \times \boldsymbol{a_3}}{\boldsymbol{a_1} \cdot (\boldsymbol{a_2} \times \boldsymbol{a_3})} \; ; \boldsymbol{a_2^*} = 2\pi \frac{\boldsymbol{a_3} \times \boldsymbol{a_1}}{\boldsymbol{a_1} \cdot (\boldsymbol{a_2} \times \boldsymbol{a_3})} \; ; \boldsymbol{a_3^*} = 2\pi \frac{\boldsymbol{a_1} \times \boldsymbol{a_2}}{\boldsymbol{a_1} \cdot (\boldsymbol{a_2} \times \boldsymbol{a_3})} \tag{4.15}$$

Therefore, using eqⁿs (4.11), (4.14) and (4.15) gives

$$\boldsymbol{G} \cdot \boldsymbol{R_n} = 2\pi \left(hn_1 + kn_2 + ln_3 \right) = 2\pi \times interger \tag{4.16}$$

Consequently, $F^{crystal}(Q)$ is non-vanishing if and only if, $\boldsymbol{Q} = \boldsymbol{G}$ equals a reciprocal lattice vector. As shown in fig. 4.1 this condition is also known as Laue condition and is equivalent to Bragg's law, $n\lambda = 2d \sin\theta$, where λ is the wavelength of the incident X-rays and d is the distance between the atomic planes[29].

To summarize, scattering from a crystal is restricted to defined points in the reciprocal lattice. Furthermore, the intensity at each point is modulated by the magnitude of the unit cell structure factor.

---

[29] Starting with Laue equation $Q = G \rightarrow k' - k = G \rightarrow |k|^2 = |k' - G|^2$ for elastic scattering condition since $|k|^2 = |k'|^2$ we get $2k' \cdot G = |G|^2$. For a lattice spacing d, $|G| = 2\pi n/d$. Therefore, the Laue equation reduces to Bragg's law $2d \cdot sin\theta = n\lambda$

4.3 Resonant Scattering

So far we have considered the interaction of EM radiation with free electrons. This is an obvious simplification since electrons in atoms are bound and occupy states with discrete energy levels. Therefore, a multielectron atom can be envisaged as a collection of n harmonic oscillators with each oscillator corresponding to resonant excitation/de-excitation of a core electron from a shell, with binding energy E_n. Consequently each atom will have a set of resonance frequencies $E_n = \hbar\omega_n$ and a characteristic damping term Γ_n, which represents the dissipation or absorption of the applied field. Therefore, the motion of the bound electron with coordinate x, can be approximated to that of a forced harmonic oscillator, with the equation of motion written as [72],

$$\frac{d^2x}{dt^2} + \Gamma_n\frac{dx}{dt} + \omega_n^2 x = -\frac{eE_o}{m_e}e^{-i\omega t} \tag{4.17}$$

having a solution of the form

$$x = \frac{1}{\omega^2 - \omega_n^2 + i\omega\Gamma_n}\frac{eE_o}{m_e}. \tag{4.18}$$

Similar to our earlier consideration calculating the scattering length for a free single electron, we can obtain the frequency dependent scattering length of a bound electron n with resonance frequency ω_n

$$f_n(\omega) = r_o F_n(\omega)\boldsymbol{\epsilon}.\boldsymbol{\epsilon}' \tag{4.19}$$

Here $F_n(\omega)$ is the frequency dependent resonance factor for a core electron n given by

$$F_n(\omega) = \frac{\omega^2}{\omega^2 - \omega_n^2 + i\omega\Gamma_n}. \tag{4.20}$$

Using the definition (4.8) the angle integrated scattering cross-section is

$$\sigma_n^{scat} = \frac{8\pi}{3}\frac{\omega^4}{(\omega^2 - \omega_n^2)^2 + (\omega\Gamma_n)^2}r_o^2, \tag{4.21}$$
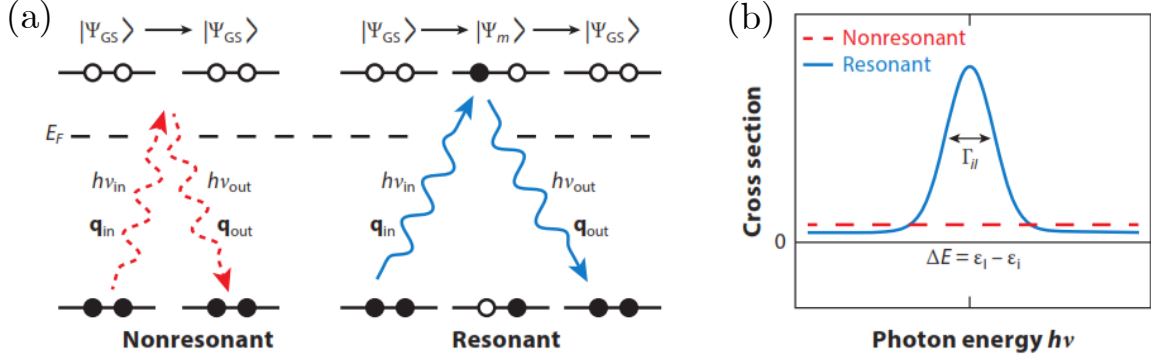
Figure 4.2 (a) Resonant and non-resonant scattering. As opposed to non-resonant scattering, resonant scattering process is a virtual transition. It involves absorption of a photon through the excitation of an occupied core electron to an unoccupied valence state, followed by a de-excitation process with photon emission. (b) Enhancement of scattering cross-section at resonance. Figure from [74].

which at resonance $\omega = \omega_n$ reduces to

$$\sigma_n^{res,scat} = \frac{8\pi}{3}\left(\frac{\omega_n}{\Gamma_n}\right)^2 r_o^2 = \left(\frac{\omega_n}{\Gamma_n}\right)^2 \sigma_T \,. \tag{4.22}$$

Since ω_n and Γ_n have the same dimensions and $\Gamma_n << \omega_n$, the resonant scattering factor is enhanced by a factor $(\omega_n/\Gamma_n)^2 \approx 10^4$ over non-resonant Thompson scattering. Thus, resonant scattering allows us to observe systems with small scattering cross-section.

Furthermore, resonant scattering can be used to probe valence band states. This becomes evident from the quantum mechanical description of the process. A time-dependent EM field induces transitions between an initial state $|i\rangle$ and final state $|f\rangle$, both states are a combination of the photon and electron. Therefore, the X-ray absorption and scattering cross-sections can be calculated by considering the time-dependent perturbation of the sample by the EM field.

The transition probability up to second-order perturbation is given as,

$$T_{i\to f} = \frac{2\pi}{\hbar}\left|\langle f|H_I|i\rangle + \sum_{n=1}^{\infty}\frac{\langle f|H_I|n\rangle\langle n|H_I|i\rangle}{E_i - E_n}\right|^2 \delta(E_i - E_f)\rho(E_f) \,. \tag{4.23}$$

H_I is the Hamiltonian representing the interaction of the electron with the photons,

$$H_I = \frac{e\boldsymbol{A}.\boldsymbol{p}}{m} + \frac{e^2 A^2}{2m} \,, \tag{4.24}$$

and $\rho(E_f)$ is the density of final states per unit energy. The vector potential $\boldsymbol{A}(\boldsymbol{r}, \boldsymbol{t})$ describing the radiation field is linear in photon creation $(a_k^\dagger)$ and annihilation operators (a_k). Since in free space $\boldsymbol{E} = -\partial \boldsymbol{A}/\partial t$, the transition probability is driven by the electric field $\boldsymbol{E}$ of the EM wave.

In eq. (4.23) the first term describes first-order processes, where the system evolves directly from the initial to the final state. The first contribution to H_I (see eq. (4.24)) describes an absorption or emission process as it is linear in $\boldsymbol{A}$ and hence can either create or destroy a photon. The second term of H_I is quadratic in $\boldsymbol{A}$ and represents an elastic scattering process, with the annihilation and creation of a photon, leaving the electron in the same state after scattering.

Resonant scattering is a second-order process, which involves transitions from $|i\rangle$ to $|f\rangle$ via virtual[30] intermediate states $|n\rangle$. As shown in fig. (4.2) the process can be visualized as absorption of an incident photon which leads to the excitation of an electron from its ground state $|i\rangle$ to an unoccupied[31] intermediate state $|n\rangle$. The electron then undergoes the reverse, making a transition from $|n\rangle$ to $|i\rangle$ with the emission of a scattered photon in the process. Away from resonance, the transition rate of these processes is suppressed by the denominator, $E_i - E_n$. However close to resonance, $E_i \approx E_n$, the denominator tends to zero and there is a strong enhancement in the transition rate of resonant scattering processes. Therefore, resonant scattering not only provides enhanced scattering close to absorption edges, providing elemental specificity but also, through intermediate states allows access to the physics of unoccupied valence states.

---

[30] Energy conservation can be violated till the final state is reached.

[31] On account of Pauli's exclusion principle.

The photon energies used in Resonant Soft X-ray Diffraction (RSXD) lie in the soft x-ray range, $100\,eV < h\omega < 2\,keV$ and thus the name[32]. The energy range for RSXD leads to a couple of experimental challenges. One, in the soft x-ray range there is high absorption of x-rays in air, therefore measurements must be carried out in an ultra-high vacuum environment. Second, x-ray wavelengths range from $12\,nm$ ($100\,eV$) to $0.6\,nm$, resulting in a large Ewald sphere. Thus, resonant soft-ray diffraction is useful for investigating materials with a large unit cell or when the system shows ordering over large lattice spacing.

4.4 Synchrotron Radiation

The RSXD measurements detailed in the thesis were carried out at the I06 beamline, at Diamond Light source (henceforth referred to as 'Diamond'), an advanced third generation synchrotron facility based at the Rutherford Appleton Laboratory, UK.

A synchrotron produces light from a relativistic beam of charged particles, typically electrons, orbiting a storage ring at a constant energy[33] (a few GeV). The beam is kept in the desired horizontal orbit by magnetic fields[34]. In such a configuration, the electrons experience the Lorentz force and emit Bremsstrahlung radiation tangential to their motion, which in the rest frame of the observer is confined to a radiation cone with a small opening angle [72,73]. The radiation is typically in the x-ray (keV) part of the electromagnetic spectrum, though photon energies down to the infrared (meV) are also produced, but at lower intensities. This collimated intense beam of light, spanning a very wide frequency range can be used for a variety of experiments.

---

[32] This energy range includes the metal K- and L- edges. Both edges involve transitions that provide valuable spectroscopic information on transition metals.

[33] Electrons are generated by thermionic emission inside an electron gun. Thereafter, they are accelerated in stages to the desired energy, following which they are injected into the storage ring.

[34] The beam is kept in a circular orbit by dipole electro-magnets (also called Bending Magnets), while other magnets such as quadrupoles and sextupoles keep the beam to a well-defined cross-section.
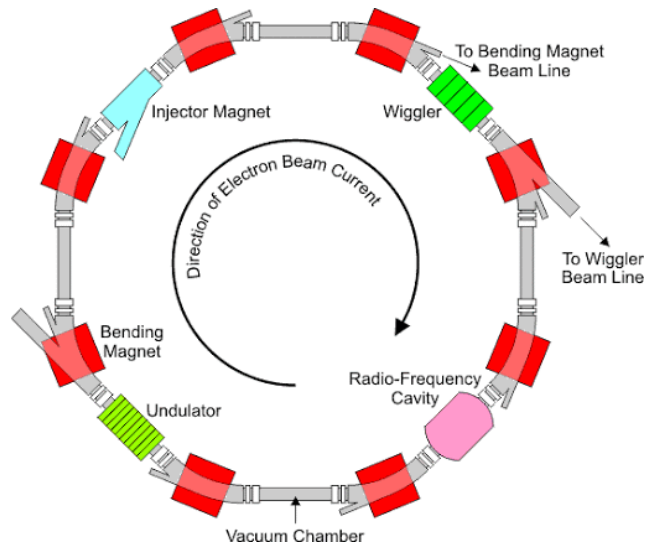
Figure 4.3 Schematic of the storage ring of a Synchrotron. The ring comprises of multiple straight sections with Bending magnets used to steer the beam around the ring. Beamlines are situated tangential to the ring [75].

It is important to note that the radiation produced at a synchrotron is not a continuous beam. Electrons emit radiation as they transverse around the ring and therefore lose energy. Radiofrequency (RF) cavities are spaced at regular intervals along the storage ring to replenish the energy lost by the electrons. The electric field inside an RF cavity forms a potential well, a 'bucket', forcing the electrons to accumulate in 'bunches'[35]. Consequently, the emitted radiation has a time structure. Each bunch comprises $\sim 10^{10}$ electrons within a length $l \simeq 10\ mm$, in the rest frame of the observer. This corresponds to a pulse duration of about $\tau = l/c \simeq 30\ ps$ full width half maximum, making synchrotrons ideal light sources for time resolved x-ray diffraction studies.

4.5 Diamond Light Source

Diamond Light Source has a storage ring with a circumference of 561 meters with the electrons orbiting at $3\ GeV$. The ring comprises of 48 straight sections which can accommodate insertion devices - array of permanent magnets configured to make the electron beam oscillate about the propagation direction many times - and 48 bending

---

[35] The electric field oscillates at a frequency such that only electrons moving at the desired energy experience zero acceleration inside the cavity, while electrons with slightly different energies will either decelerate or accelerate depending on if they arrive earlier or later inside the cavity.

magnets which are used to steer the beam around the ring[36]. The various experimental stations (Beamlines) situated tangentially around the ring make use of radiation emitted from either insertion devices or the bending magnets (Fig. 4.3). At Diamond depending on the beamline, the electromagnetic radiation can range from the far-infrared ($2.4\ meV$) to the ultra-hard x-ray ($150\ keV$) regime.

Under standard operation, the beam current of the storage ring is kept constant ($\cong$ $300\ mA$) by operating in top-up mode, where electron bunches in the storage ring[37] are replenished periodically ($\sim$ 12 mins). Consequently, the x-ray intensity on the sample varies by very small amounts and experiments can run over multiple days without interruptions.

4.6 Undulator Radiation

Insertion devices comprise of an array of alternating north and south poles of permanent magnets, which force the electrons to execute a highly oscillatory path and concomitantly emit X-rays. There are two types of insertion devices, wigglers and undulators, with the latter being used on beamline I06 for the production of soft x-ray radiation.

The difference between wigglers and undulators is the maximum angular deviation of the electron beam from the propagation axis as it transverses the device. This is denoted by a dimensionless number K, expressed as [73] -

$$K = 0.934\lambda_u[cm]B[T]. \tag{4.25}$$

where λ_μ is the oscillation period and B is the magnetic field of the insertion device. In a wiggler the magnetic field is strong and thus the angular deviation of the electron

---

[36] Insertion devices are way more efficient at producing x-rays as compared to bending magnets. Synchrotrons with storage rings optimised to accommodate insertion devices are characterised as 3rd generation light source.

[37] Even though the storage ring is kept under very high vacuum (typically 10^{-10} mbar) there are collisions between electron bunches and particles in the ring, which leads to the beam current decaying over a period of time.
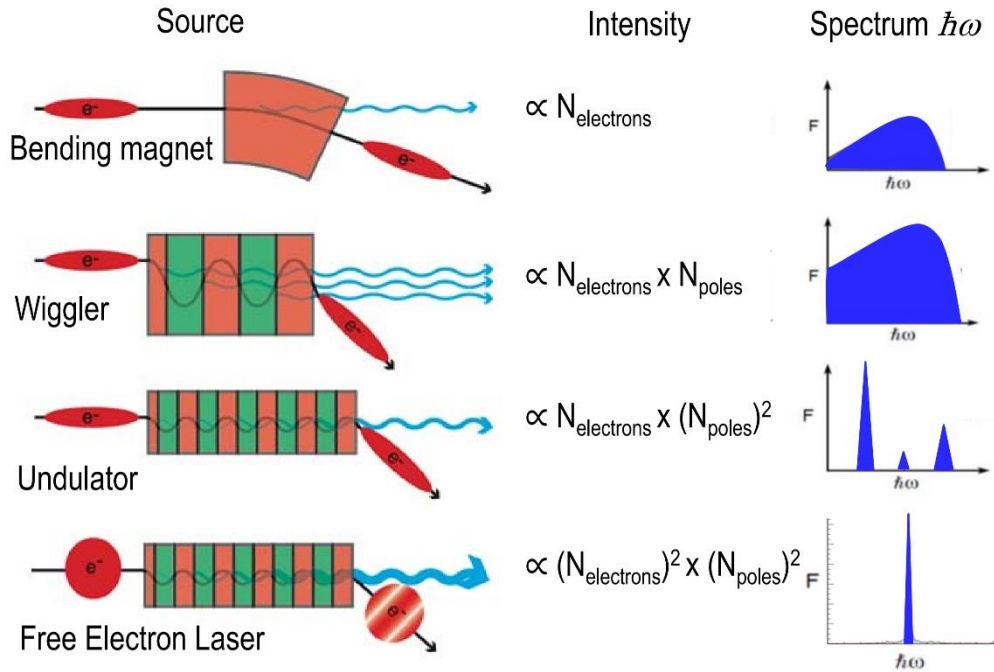
Figure 4.4 Comparison of radiation intensity and spectrum emitted from different sources [76].

beam about its propagation direction is large, $K \gg 1$. The radiation generated by a wiggler may be viewed simply as that generated from a series of independent bending magnets.

In contrast, the magnetic field in an undulator is weak, and the angular deflection is very small, $K \approx 1$. Because of the weak deflection we can assume that both the electrons and emitted photons travel effectively straight. Therefore, the wavefront emitted by an electron from two positions separated by λ_μ (or multiples n thereof) will be in phase, resulting in constructive interference. The energy spectrum from an undulator, thus is centered around a fundamental wavelength and includes its higher harmonics, given by the following equation -

$$n\lambda_n = \frac{\lambda_u}{2\gamma^2}\left(1 + \frac{K^2}{2}\right), \quad n = 1,2, \dots \tag{4.26}$$

The emitted wavelength can be tuned by varying the undulator gap, which changes the inside magnetic field, which in turn changes K. Additionally, undulators provide complete control of the polarization of the emitted radiation. Not only can we achieve
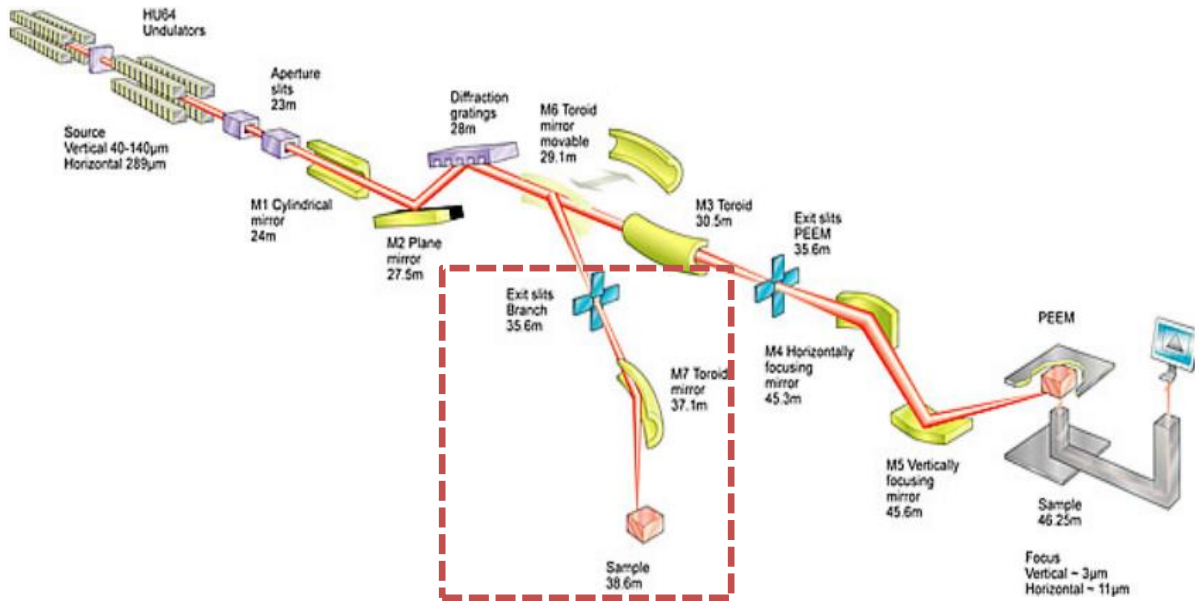
Figure 4.5 I06 Beamline. The highlighted area is the branchline.

linearly polarized light but through a complicated arrangement of the magnets make the electron beam transverse a helical trajectory, giving rise to emission of circularly polarized light of either handedness.

4.7 Beamline I06

The I06 beamline is a soft x-ray beamline making use of two so-called APPLE II undulators, whose energies can be tuned over a range of $120 - 1500$ eV for vertical polarization, $80 - 2100$ eV for horizontal polarization and $106 - 1300$ eV for circular polarization. Following the undulator, a plain grating monochromator spectrally filters the light to a bandwidth of 40 meV.

Time resolved Resonant Soft X-ray Diffraction (Tr-$RSXD$) experiments reported in this thesis were performed on the branchline of the I06 beamline, which is outlined in Fig. 4.5. On the branchline, the x-rays can be focused to a spot size of 20 $\mu m \times 200$ μm in the vertical and horizontal direction, respectively. Furthermore, as runtime of single measurement often last many hours, and the sample size can be relatively small, it is essential that the X-ray beam maintained very high pointing stability on the sample for long durations. This was achieved by stabilizing a hexapod mirror such that the
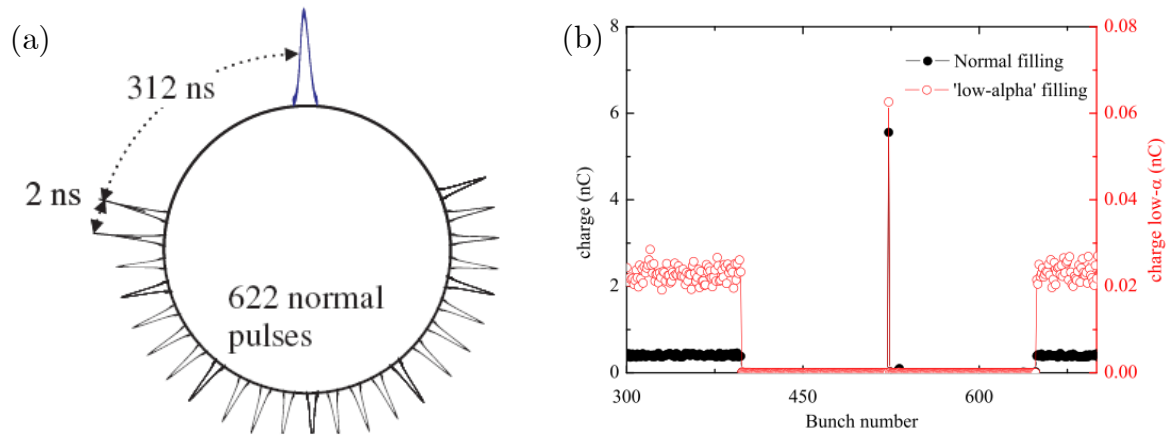
Figure 4.6 (a) Filling pattern in 'camshaft' or 'hybrid' mode. (b) Comparison of the charge in the 'low-alpha' mode with the normal hybrid mode.

photoemission (which is measured as a current) from exit slits close to the sample is kept constant.

4.8 Filling pattern

The Diamond storage ring can accommodate **936** electron bunches separated from each other by **2 ns**. This translates to **499.654 MHz** repetition rate for the X-rays, with round-trip frequency of each electron bunch being **533.83 KHz**. Unfortunately, such high repetition rates do provide a sufficiently large time window to measure the signal generated from a specific x-ray pulse. Therefore, for time-resolved measurements, a special filling pattern of the storage ring is used. This pattern is referred to as 'Camshaft' or 'Hybrid' mode.

In this configuration, two-thirds of the ring is filled with electron bunches with the usual **2 ns** temporal spacing, while the remainder third of the ring is filled with only one electron bunch, Fig. 4.6(a). As a result, the single bunch is separated from the next bunches by several hundred nanoseconds on either side and is known as the 'camshaft' or timing pulse. Consequently, this provides a large enough time window for the X-ray detection electronics to 'gate'[38] the signal generated from the camshaft pulse. Another advantage of the separation of the camshaft pulse from the contiguous

---

[38] Time window during which any generated signal is measured. Signals outside the time window are discarded.

pulses is that it allows increasing the charge in the camshaft bunch by about an order of magnitude to $\sim 5-6\,nC$, as compared to the multi-bunches $\sim 0.4\,nC$, see Fig.4.6(b). This produces bigger signals from the camshaft pulses, albeit these bunches are wider spread in space on account of enhanced coulomb repulsion inside the bunch. Typically, the camshaft pulse has a duration of about $60\,ps$ (Full Width at Half Maximum - FWHM).

The X-ray pulse duration can be reduced by decreasing the longitudinal width of the electron bunch, coming at the cost of the reduced amount of charges that can be packed into the same bunch and the concomitantly decreased X-ray flux. Since, the longitudinal width of the electron bunch is expressed in terms of the momentum compression factor, α, this mode of operation is known as the 'low-α' mode. At Diamond, in the low-α mode, X-ray pulse duration of $5\,ps$ (FWHM) can be achieved with $64\,pC$ of charge stored.

4.9 Diffraction Chamber Layout and Experimental Setup

The diffractometer designed for the RSXD experiments is housed inside a vacuum chamber (base pressure of $10^{-9}mbar$) and employs a $\theta-2\theta$ design, with independent manipulators for the sample (θ) and (2θ) detector rotation. The diffractometer geometry allows the following types of diffraction scans:

1. <u>Radial scan or $\boldsymbol{\theta-2\theta}$ scan</u>: A scan along a fixed direction defined by the scattering vector $\boldsymbol{Q}$ perpendicular to the sample surface. This is done by rotating the sample and the detector in steps of θ and 2θ, respectively, about the center of rotation z.

2. <u>Transverse scan</u>. This is a scan perpendicular to the direction defined by $\boldsymbol{Q}$. It contains information about correlation in the plane perpendicular to $\boldsymbol{Q}$, but is also often affected by the sample mosaicity. A transverse scan can be done by rotating the sample about z, while keeping the detector position fixed.
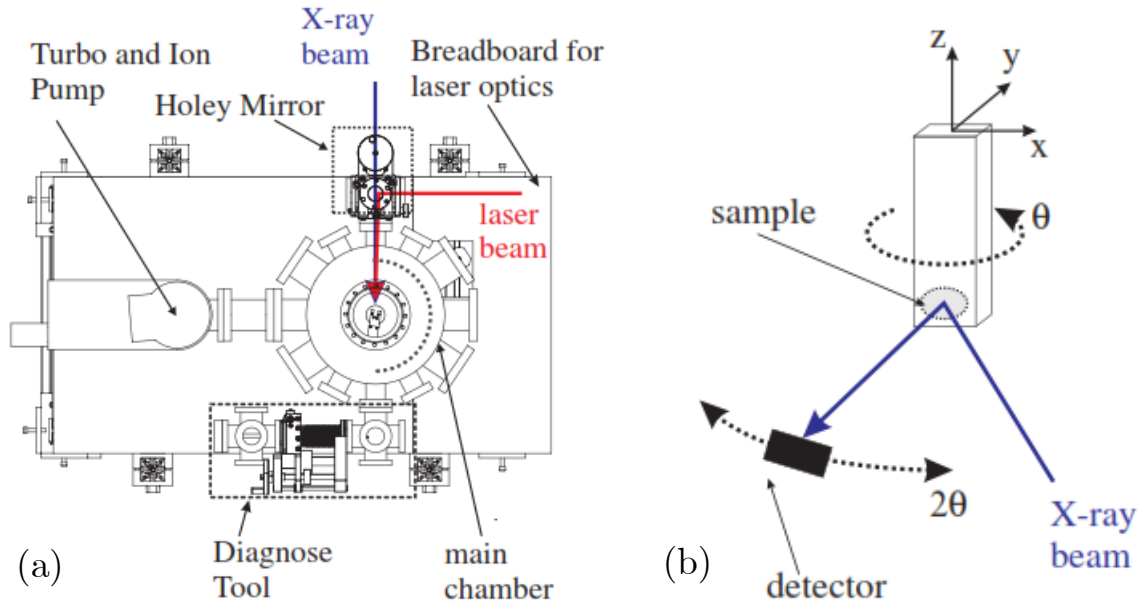
Figure 4.7 (a)Diffraction chamber used for Tr-RSXD. (b) Degrees of freedom of sample holder and detector. Both the sample holder and detector can be translated along the z-direction [77].

3. <u>Energy scan</u>. Here the photon energy dependence of for fixed Q is measured. This is achieved by scanning the photon energy, while recording the scattered intensity at $Q = k' - k$. Since both k and k' change with the photon energy, for each photon energy the scattering geometry is adjusted to keep Q constant.

The sample holder is attached to a liquid Helium flow cryostat, allowing control of the sample temperature between $4.5 - 320\,K$. The sample holder also incorporates a knife edge – to measure the x-ray and laser spot size at the sample, and a phosphor screen above the sample which lies in the same vertical plane as the sample, Fig 4.7(b). The phosphor screen not only helps with making the x-rays visible to the naked eye via a CCD camera but also aids with coarse spatial overlap of the x-ray and laser beams. A 'holey mirror' (a silver mirror with a hole in the center) is used to couple the laser light into the chamber resulting in a nearly collinear pump-probe configuration, with the x-ray beam passing from the back of the mirror through a hole. A schematic of this is shown in Fig. 4.8. Once the x-rays and laser beam are overlapped on the phosphor screen, the sample is translated into the beam and spatial overlap is optimized with the help of fast steering mirrors, which raster the laser beam on the sample (in the XZ plane) to give the maximum photo-excited signal. Thereafter, the
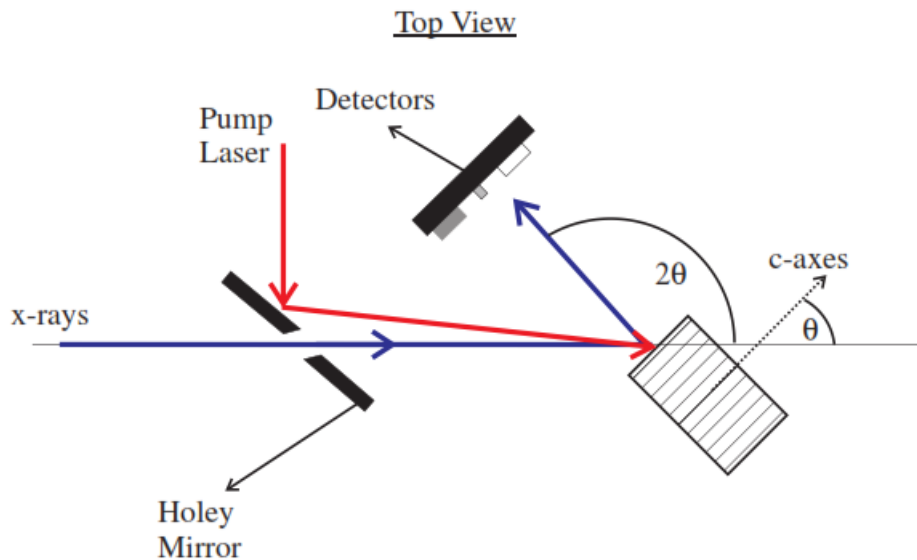
Figure 4.8. A nearly collinear geometry of X-ray and laser beam is achieved by using a holey mirror [77].

laser beam is spatially locked onto the sample position using a combination of fast steering mirrors and beam position monitors. Active beam stabilization of both the laser and x-rays mitigates against loss of spatial overlap on the sample due to long term changes (primarily thermal in origin) in the experimental setup.

Lastly, just before the laser beam is coupled into the vacuum chamber, a polarizer sets the polarization of the laser beam. In conjunction with a motorized half-wave plate, the excitation fluence of the laser pulse on the sample can be controlled. The beam profile and power of the laser are actively recorded to have an accurate assessment of the pump fluence during a measurement.

4.10 Detection Instrumentation

The detector arm also holds an array of detectors which can be used to measure static and time resolved signals. A photodiode is used to measure the static diffracted signal and a Micro Channel Plate (MCP) is used to measure the time resolved diffracted signal from the sample. The MCP is an ideal detector for such time resolved measurements as,

- it is fast enough to resolve the X-ray bunch structure

- can detect single photons

- is blind to $1.55\ eV$ excitation photons of the optical laser.

The signal from the MCP is amplified and fed into two identical gated discriminators, which are triggered by a gate signal generated from a delay generator synchronized to the master clock of the storage ring. Two adjacent x-ray pulses are used to measure the photo-excited response. One discriminator measures the pump 'on' signal – when the sample is in its photo-excited state and the second discriminator measures the pump 'off' channel – when the sample is in its ground state[39]. Therefore, with each measurement we can measure the change in the diffracted intensity normalized to the ground state of the sample. The signal from the discriminator is converted into a scaler counter, giving counts per unit time and this value from the two channels - ON and OFF are logged.

4.11 Laser System

The light source for the sample excitation in Tr-RSXD experiments at I06 is a Ti:sapphire laser system, producing $800\ nm$ ($1.55\ eV$) femtosecond laser pulses. The system comprises of a mode-locked oscillator (MIRA) which seeds a Regenerative Amplifier (RegA) producing μJ pulses with a pulse width of $\sim200\ fs$. Both the oscillator and the amplifier are pumped by the same pump source, a Verdi V18 CW solid state laser emitting at 532 nm.

Laser pulses are synchronized to the X-rays by locking the repetition rate of the laser oscillator to exactly one-sixth ($83.275\ MHz$) of the storage ring master clock frequency. This stabilization is done actively through electronic synchronization (Synchrolock system, Coherent Inc. [78]), which receives the frequency from the storage ring master clock and the oscillator frequency from an external photodiode. The stabilization system minimizes the timing jitter between the x-ray and laser pulses by adjusting the

---

[39] Such a measurement is only possible if the repetition rate of the laser, f_l, is smaller than half the revolution frequency of the single x-ray bunch, i.e. $f_l < \frac{533.82}{2}\ KHz$

length of the oscillator cavity by moving a piezo element on one of its end mirrors. Whilst the repetition rate of the oscillator is locked the frequency of the amplifier can be adjusted from $266.91\,KHz$ (half the revolution frequency of the storage ring) down to $22\,KHz$. An Avalanche Photo Diode (APD) housed at the back of the vacuum chamber is used to measure the temporal delay between the x-ray and laser pulses. Output from the APD can be viewed directly on a fast oscilloscope and with the use of Synchrolock, the laser pulse delay can be adjusted to within a resolution of $\pm 500\,ps$ of the x-ray pulse.

The Synchrolock is also used while taking scans to measure the photo-induced signal as a function of pump (laser) delay. Coarse temporal delay is achieved by choosing which oscillator pulse is amplified. This gives a delay of an integer multiple of the oscillator clock $t = n \cdot \dfrac{2}{83.275\,MHz} \approx n \cdot 24\,ns$. By changing the phase delay in the Synchrolock one can adjust the time delay continuously between $0 - 12\,ns$, with an accuracy of 22 fs. The finest temporal adjustment is achieved by using a mechanical delay stage, which gives a range of $1\,ns$ with a minimum step size of 1 fs.

Measurements performed with the above experimental setup are reported in chapter 6.

5 Terahertz Time-Domain Spectroscopy

5.1 The Terahertz Domain

The Terahertz ($1\,THz = 10^{12}$ Hz) band lies between microwaves and infrared region of the electromagnetic spectrum and is roughly defined from 0.1 THz - 10 THz, which corresponds to wavelengths ranging between $3\,mm$ to $30\,\mu m$[40]. This spectral range is important to understanding the electronic properties of condensed matter systems as, electronic bound states such as excitons and Cooper pairs, collective quasiparticle excitations, scattering rates, confinement in low dimensional materials, all have energies in the THz regime.

Traditionally, terahertz spectroscopy has been hampered by lack of bright sources and efficient detectors. Microwave sources are limited to frequencies below 100 GHz and Fourier Transform InfraRed (FTIR) spectrometers lack brightness in the THz regime. Additionally, the aforementioned techniques only measure the intensity of the electric field and are insensitive to the phase and therefore rely on Kramers-Kronig analysis, to calculate the real and imaginary part of the response functions.

In the last few decades, advances in laser and optical technologies, especially the widespread adoption of femtosecond laser systems has led to proliferation of Terahertz Time-Domain Spectroscopy (THz-TDS). The principle of THz-TDS is based on the opto-electronic generation of the THz transients from femtosecond laser pulses, which are then detected using optical gating. This allows for the direct measurement of the amplitude and phase of the terahertz electric field, from which the real and imaginary

---

[40] In other frequently used units: $1\,THz = 4.13\,meV; 33.3\,cm^{-1}$.

part of the response function (optical constants) of a medium can be extracted without resorting to Kramers-Kronig analysis. The THz transients are much brighter than conventional thermal sources and spectrally broad, ranging from less than 100 GHz to more than 10 THz. Additionally, as gated detection is only sensitive to signals in phase with the source, it is orders of magnitude more sensitive than bolometric detection. Furthermore, the THz transients are inherently, temporally synchronised with the femtosecond laser pulses that generate them and are typically less than 1 ps duration, thus making THz-TDS ideally suited for pump-probe experiments.

5.2 Generation and Detection

Single- or few-cycle THz pulses are generated and detected using either of the two operational concepts (i) Interaction of a femtosecond laser pulse with a non-linear medium, giving rise to a time varying induced polarization in the medium which results in Optical Rectification (OR) of the incident pulse (ii) Accelerating charges or time varying currents radiating electromagnetic waves. In the experiments undertaken in this thesis, the latter principle has been used for the generation of THz using a Photoconductive emitter, while the former is used for the detection of THz using the technique of Electro-Optic sampling (EOS) in a $ZnTe$ crystal.

5.3 Terahertz Generation using a Photoconductive Switch

Photoconductive (PC) emitters are an array of photoconductive switches/antenna and are the most commonly used method for the generation and detection of THz in TDS. A photoconductive switch is a fast, optically activated switch comprising of metal electrodes on a semiconductor substrate. The switch is shortened by a laser pulse with photon energy greater than the bandgap of the semiconducting material, creating free carriers – electrons and holes. A bias voltage between the electrodes accelerates the free carriers which are then recaptured on a picosecond timescale, leading to a transient photocurent I_{PC} generated between the electrodes.
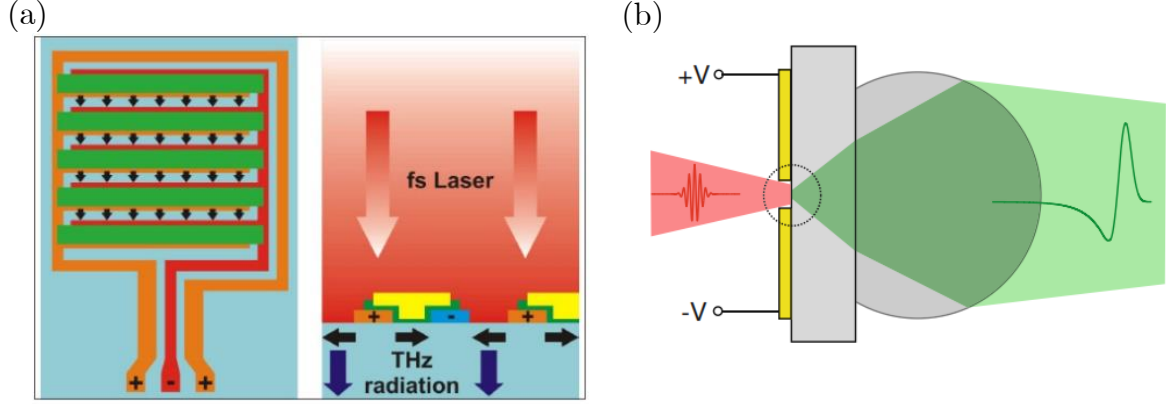
(a)

(b)

Figure 5.1 (a) Ariel and cross-sectional view of the photoconductive antenna (TeraSED) used for generation of THz. Black arrows indicate direction of the applied electric field across the electrodes [79]. (b) Profile view of a PC antenna. Femtosecond laser light (800 nm) incident on the surface of an antenna with emission of THz radiation [80].

The PC switch can thus be modelled as a Hertzian dipole with the far field radiation E_{THZ} described as [81]:

$$E_{THZ} \propto dI_{PC}/dt \qquad (5.1)$$

For the emitted radiation to be in the THz regime the switching action (ON-OFF) of the PC switch should be in the sub-picosecond time range. Switch-ON time is a function of the laser pulse duration (first half cycle of the emitted radiation is a function of this) and the switch-OFF time is mostly dictated by the lifetime of the photoexcited carriers (second half cycle of the emitted radiation is a function of this). Therefore, in order to generate single cycle broad bandwidth THz pulses, a combination of short femtosecond laser pulses and a material with short carrier lifetime is vital. Among the photoconductive materials used, low-temperature grown gallium arsenide (LT-GaAs) is the most common. It has a photoexcited carrier lifetime[41] of $\sim 0.2\,ps$ [81] and a bandgap of 850 nm which is well suited for use with a Ti:sapphire laser system.

For our measurements it was crucial to that we measured frequencies down to $\sim 100\,GHz$. To meet these requirements, we used a photoconductive emitter, Tera-SED,

---

[41] LT-GaAs has a high concentration of defects ($> 10^{18}\,cm^3$) induced during the growth process by incorporating an excess of arsenic [ref]

manufactured by Laser Quantum which has a spectral range from 100 GHz up to 6 THz [79]. Tera-SED is a large-area GaAs based photoconductive emitter employing a patented interdigitated metal-semiconductor-metal (MSM) structure, effectively multiplexing more than a hundred photoconductive switches. Metal electrodes with $5\,\mu m$ spacing are fabricated on a semi-insulating GaAs substrate, giving an electric field of a $20\,kV/cm$ for a bias voltage of only $10\,V$. As the field direction between adjacent electrodes is reversed, every second electrode finger spacing is masked with an optically opaque metallic layer. Therefore, only gaps with the same field direction are optically excited, resulting in constructive interference of the emitted THz in the far field.

5.4 Terahertz Detection – Electro-Optic Sampling

Electro-Optic (EO) sampling is based on temporally sampling the electric field profile of a THz pulse, $E_{THz}(t)$, by a much shorter optical pulse. In general, the optical setup involves splitting a small fraction of the optical beam that is used to generate the THz, to measure the temporal profile of the THz pulse in EO crystals. The underlying principle of EO sampling makes use of the Pockels effect, which describes the birefringence induced in nonlinear optical medium as proportional to the applied electric field. Conversely, by measuring the field-induced birefringence in an EO crystal we can determine the applied field strength. Importantly, for the optical pulse to experience a constant electric field of the THz pulse in the EO crystal, the optical group velocity and THz phase velocity should match inside the crystal.

A schematic of a typical EO sampling setup is shown in Fig. 5.2 with the bottom half depicting the evolution of the polarization of the sampling probe beam, with and without a THz field. A balanced photodetector measures the intensity difference, I_s between the two orthogonal components of a circularly polarized sampling probe pulse. In the absence of a THz field, the orthogonal components are equal, and the photodetector is perfectly balanced, thus registering no signal. However, the presence of a THz field induces birefringence in an EO crystal which causes the linearly polarised probe pulse to develop ellipticity. As a result, after the quarter waveplate, the
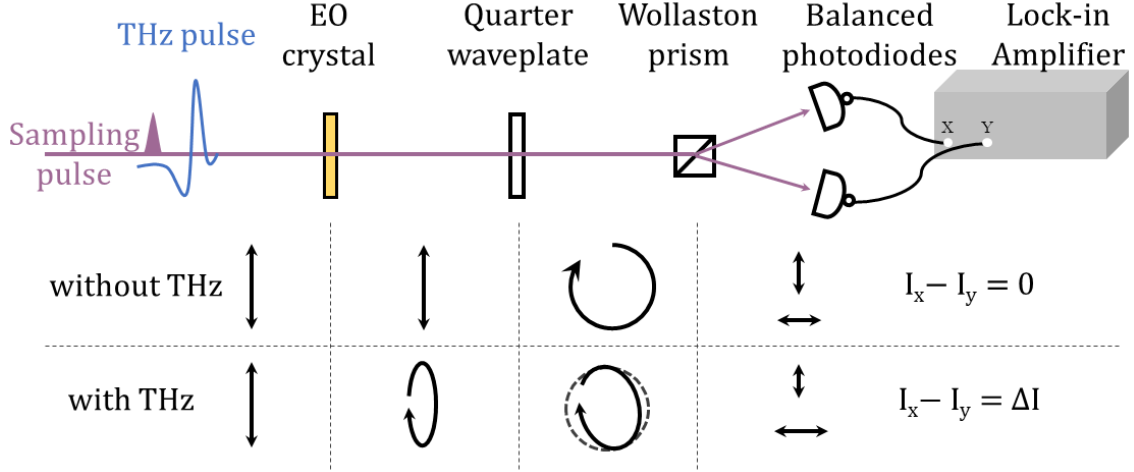
71

Figure 5.2 Illustration of the Free space Electro-optic sampling used to detect THz. [81]. See section 5.4 for description.

polarization of the probe pulse is no longer perfectly circular and the two orthogonal components after the Wollaston prism are unequal.

This leads to the photodetector becoming imbalanced and registering an intensity difference, I_s, which is proportional to the THz electric field, E_{THz} [81] −

$$I_s = I_x - I_y = I_o\Delta\phi = \frac{I_o\omega L}{c}n_O^3 r_{41}E_{THz} \propto E_{THz} \qquad (5.2)$$

Here $\Delta\phi$ is the differential phase retardation experienced by the sampling probe beam due to the Pockels effect over the thickness (L) of the EO crystal. I_o is the intensity of the sampling probe beam, n_o is the refractive index at the optical frequency and r_{41} is the EO coefficient.

By scanning the relative delay between the sampling and THz pulses, and measuring the corresponding intensity differences, we can map out the electric field of the THz pulse, $E_{THz}(t)$, thus allowing the simultaneous determination of the amplitude and phase of the field. The absolute value of the Fourier transform of $E_{THz}(t)$ gives the spectral range of the field.

In our measurements, 1 mm, <110> cut $ZnTe$ crystals were used for the EO sampling of the THz pulse. $ZnTe$ meets the phase-matching conditions for THz and 800 nm, is

transparent at optical and THz frequencies, and has a large to EO coefficient, making it an ideal EO crystal for measuring THz frequencies[42] up to 5 THz.

5.5 Pump-Probe Scanning

There are two time delays in time-resolved THz spectroscopy (TRTS):

1. The time delay τ which refers to the delay between the optical pump pulse and the sampling probe pulse. This reflects the excitation dynamics of the sample.

2. The time delay t, this refers to the delay between the THz pulse and the optical sampling pulse and maps out the THz field reflected off the sample.

Conventionally, $\tau = 0$, is defined as the pump pulse arriving at the sample surface. However, in the case of TRTS there are a couple of challenges that need to be addressed.

Since the THz pulse is much longer than the optical pump pulse, only the part of the THz pulse arriving after the photoexcitation will be affected. Therefore, the THz pulse reflected off the sample will contain a mixture of information about optical constants of the sample at equilibrium and in its photoexcited state. Scanning τ, will create datasets with different time zeros, creating ambiguity in defining $\tau = 0$. This will also complicate analysing the temporal evolution of the photoexcited response. The problem is further exacerbated if the response of the system is faster than the THz pulse. By only scanning τ, we will miss out on the earliest dynamics of the photoexcited system.

The solution is to simultaneously scan both the delay lines, τ and t, such that every part of the THz pulse experiences the same pump delay, see Fig. 5.3. This ensures that there is no ambiguity with regard to $\tau = 0$ and for a given pump delay, the reflected THz profile encodes the full spectral response of the sample. This also highlights the fact that the temporal resolution of the experiment is not limited by the duration of

---

[42] A TO phonon mode at 5.3 THz limits the bandwidth to frequencies below 5 THz
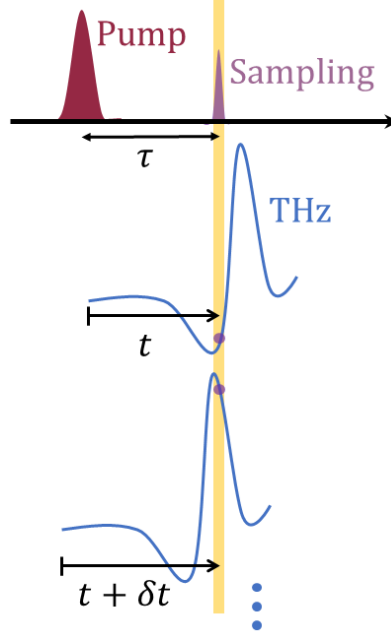
Figure 5.3 The time delays involved in time-resolved THz spectroscopy. τ is the time delay between the pump and sampling pulse, and reflects the time after excitation of the sample. t on the other hand, is the delay between the THz and sampling pulse, and maps out the THz field reflected off the sample.

the THz pulse, which extends over a few picoseconds, but rather by the spectral content of the THz.

Since our goal is to measure the pump-induced changes to the THz field, which is given as, $\Delta E(t) = E_{on}(t) - E(t)$, where $E_{on}(t)$ is THz field reflected off the sample after excitation and $E(t)$ is the reflected field with sample at equilibrium. The two fields can be measured concurrently by using a chopper to modulate the THz beam, with a lock-in amplifier synchronised to the chopper frequency to read out the signal from the EOS photodetector. When the pump-induced changes are very small, we can modulate the pump beam to directly measure $\Delta E(t)$ at a higher lock-in sensitivity.

Thus, we measure $\Delta E_{THz}(t, \tau)$ which is Fourier transformed to yield $\Delta \tilde{E}_{THz}(\omega, \tau)$. The normalized Fourier transform reflectivity spectrum is given as:

$$\frac{\Delta \tilde{E}_{THz}(\omega)}{\tilde{E}_{THz}(\omega)} = \frac{\tilde{E}_{on}(\omega) - \tilde{E}_{THz}(\omega)}{\tilde{E}_{THz}(\omega)} \tag{5.3}$$

5.6 Setup and Chamber

A picture and sketch of the optical pump THz probe setup used for our experiments is shown is Fig. 5.4. The measurements presented in the thesis were carried out on single crystals of $LBCO_{11.5}$ and in reflection geometry, with the pump beam hitting the sample at normal incidence and the probe beam is incident at 30°. In order to eliminate water absorption, achieve short focal length and avoid losses in windows, the THz was generated and detected inside a vacuum chamber. The chamber can reach a base pressure of 5×10^{-7} mbar, which is sufficient to prevent ice formation at cryogenic temperatures. The sample and a piece of n-doped GaAs sat at the end of a cold finger of a Helium-flow cryostat which is affixed to the chamber. By pumping at the exhaust of the helium siphon we could reach temperatures of ~2 K. GaAs has a large optical pump THz probe response which makes it convenient to optimize for spatial and temporal overlap. Once optimized the sample is translated into the beams. After cooling, measurements are only commenced once thermal equilibrium is reached which can take up to 4 hours. Thermal contraction/expansion of the cold finger can also be checked, by looking at the THz reflected off the GaAs or the sample.

Polarization of the THz is determined by the orientation of the photoconductive switch and is checked by a MIR polarizer placed in its path before the EOS optics. The focal plane of the THz beam is determined by translating the cold finger so as to maximise the low frequency THz response. The pump beam profile is measured outside the vacuum chamber using a razor blade and a photodiode, using distances and focal lengths that are identical to that used in the setup in the chamber. The focussing lens position is optimized to match the THz beam width, with the pump beam spot size kept slightly bigger than the THz, so that the THz probes a homogenous pumped region.

Pump-probe response is measured by moving delay stages set along the pump and sampling probe paths. A chopper is placed in the pump beam path to measure the pump induced changes.
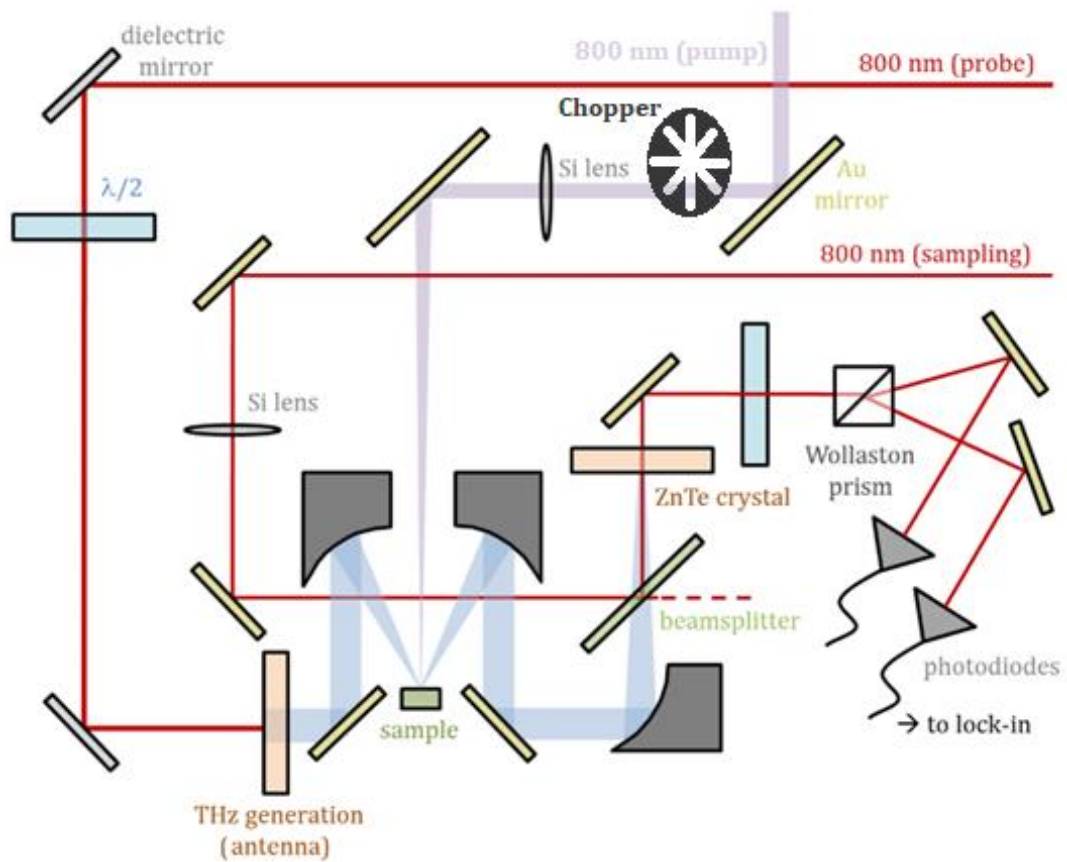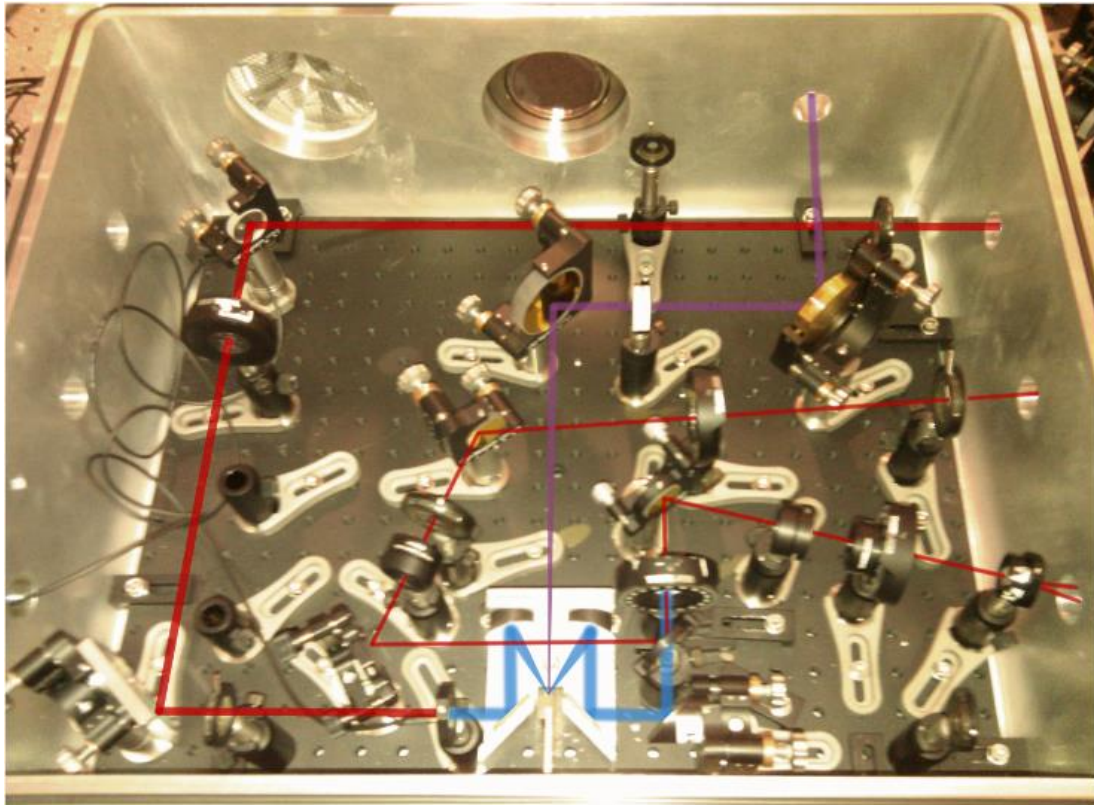
Figure 5.4 (top) Picture and (bottom) schematic of the optical pump and THz probe setup used for our measurements.

5.7 Analytic Models for photo-excited materials

As light propagates through a medium it is absorbed, and its intensity decreases exponentially according to the Beer-Lambert Law:

$$I(z) = I_0 e^{-\alpha z} \tag{5.4}$$

where, I_0 is the incident intensity, α is the absorption coefficient and $1/\alpha$ gives the penetration depth. Consequently, the optical properties of the material vary not only in time but in space as well. We will consider a few models to analysis the optical properties of the photo-excited material.

5.7.1 Bulk excitation

When the pump penetration depth is much larger than that of the probe, we can consider a homogenously photo-excited volume of the sample. In this limit, we can relate the complex reflection coefficient of the excited material, $\tilde{r}'$, with the transformed refractive index, $\tilde{n}'$, via the Fresnel's equations -

$$\tilde{r}'_s = \frac{\cos\theta_i - \tilde{n}'\sqrt{1 - \left(\frac{\sin\theta_i}{\tilde{n}'}\right)^2}}{\cos\theta_i + \tilde{n}'\sqrt{1 - \left(\frac{\sin\theta_i}{\tilde{n}'}\right)^2}} , \quad \text{(TE Wave)} \tag{5.5}$$

$$\tilde{r}'_p = \frac{\sqrt{1 - \left(\frac{\sin\theta_i}{\tilde{n}'}\right)^2} - \tilde{n}'\cos\theta_i}{\sqrt{1 - \left(\frac{\sin\theta_i}{\tilde{n}'}\right)^2} + \tilde{n}'\cos\theta_i} , \quad \text{(TM Wave)} \tag{5.6}$$

The subscripts s and p refer to the two orthogonal components - perpendicular and parallel, respectively - of the incident light. The above are simplified Fresnel equations, where we have considered a vacuum interface with the medium ($n = 1$) and θ_i is the angle of incidence on the sample.
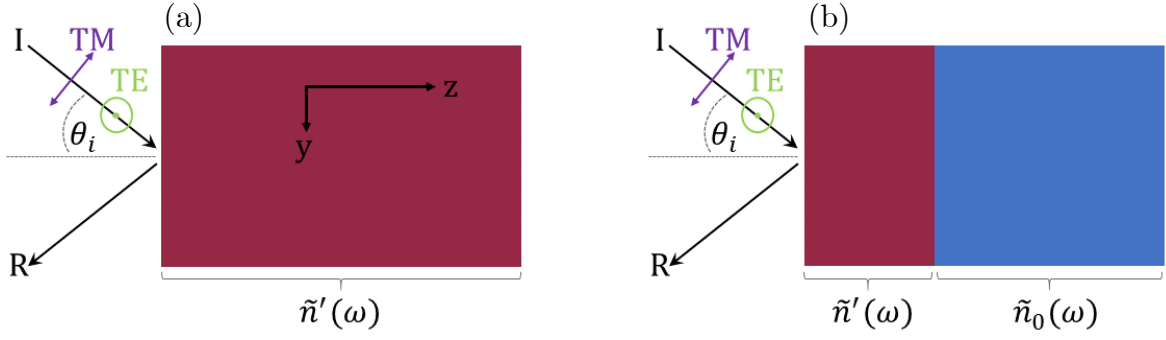
Figure 5.5 Photoexcited models: (a) Bulk excitation and (b) single film limit

The change in the reflection coefficient is related to the change in the reflected electric field,

$$\frac{\Delta \tilde{E}(\omega)}{\tilde{E}(\omega)} \equiv \frac{\Delta \tilde{r}}{\tilde{r}} = \frac{\tilde{r}' - \tilde{r}}{\tilde{r}} \tag{5.7}$$

Thus, by measuring the relative changes in the electric field is insufficient to determine $\tilde{r}'$, since we need to know the equilibrium reflection coefficient $\tilde{r}$ as well. $\tilde{r}$ can be calculated independently from broadband reflectivity using Kramers-Kronig analysis or from referenced time-domain THz spectra. From the equilibrium refractive index $\tilde{n}_0$ we can determine $\tilde{r}$ using the Fresnal equations. Once we have determined $\tilde{r}'$ we can invert equations (5.5) and (5.6) to calculate the transient refractive index,

$$\tilde{n}' = \sqrt{sin^2\theta_i + cos^2\theta_i \left(\frac{1 - \tilde{r}'}{1 + \tilde{r}'}\right)}, \qquad \text{(TE Wave)} \tag{5.8}$$

$$\tilde{n}' = \frac{1}{\sqrt{2}}\left(\frac{1 + \tilde{r}'}{1 - \tilde{r}'}\right)\sqrt{1 + \sqrt{1 - 4sin^2\theta_i cos^2\theta_i \left(\frac{1 - \tilde{r}'}{1 + \tilde{r}'}\right)^2}}, \qquad \text{(TM Wave)} \tag{5.9}$$

5.7.2 High Pump-Probe penetration mismatch: Thin Film limit

In the opposing limit when the probe penetration depth is much larger than that of the pump, we can consider a thin homogenously photo-excited layer sitting above an unperturbed bulk, see Fig 5.5 (b).

The complex reflection coefficient of such a multilayer system is expressed as [82]:

$$\tilde{r}(\omega, \tau) = \frac{\tilde{r}_A(\omega, \tau) + \tilde{r}_B(\omega, \tau)e^{2i\delta(\omega, \tau)}}{1 + \tilde{r}_A(\omega, \tau)\tilde{r}_B(\omega, \tau)e^{2i\delta(\omega, \tau)}} \tag{5.10}$$

Where $\tilde{r}_A(\omega, \tau)$ and $\tilde{r}_B(\omega, \tau)$ are the reflection coefficients at the interfaces vacuum/photoexcited layer and photoexcited layer/unperturbed bulk, respectively, while $\delta = 2\pi d\tilde{n}(\omega, \tau)/\lambda_0$ (here, $\tilde{n}(\omega, \tau)$ is the complex refractive index of the photoexcited layer and λ_0 is the probe wavelength).

Equation (5.10) can be solved numerically, thus retrieving $\tilde{n}(\omega, \tau)$ from the experimentally determined $\tilde{r}(\omega, \tau)$. Complex conductivity for a volume that is homogenously transformed can then be calculated using the following relation,

$$\tilde{\sigma}(\omega, \tau) = \frac{\omega}{4\pi i}[\tilde{n}(\omega, \tau) - \varepsilon_\infty]. \tag{5.11}$$

Where ε_∞ represents the screening by interband transitions [83].

Alternatively, we can also model the photo-excited system as a stack of thin layers with a homogenous refractive index, with an excitation profile given by an exponential decay. Both these models yield similar results.

6 Melting of Stripe and Structural order in La$_{2\text{-x}}$Ba$_{x}$CuO$_4$

6.1 Introduction

In this chapter we report time-resolved resonant soft X-ray diffraction (TR-RSXD) measurements of the near-infrared photoexcitation dynamics of the stripe order and crystal lattice in superconducting La$_{1.885}$Ba$_{0.115}$CuO$_4$ (LBCO$_{11.5}$) carried out at the I06 beamline at Diamond Light Source [5]. These results are augmented with our TR-RSXD experiments on the excitation of the in-plane Cu-O stretching phonon with mid-infrared pulses in the non-superconducting, stripe ordered La$_{1.875}$Ba$_{0.125}$CuO$_4$ (LBCO$_{1/8}$) performed at the SXR beamline of the Linac Coherent Light Souce (LCLS) [84]. Excitation of the in-plane Cu-O stretching phonon with a midinfrared pulse has been previously shown to induce a transient superconducting state in the closely related compound La$_{1.675}$Eu$_{0.2}$Sr$_{0.125}$CuO$_4$ (LESCO$_{1/8}$)[43], however the fate of the charge stripe order and of the LTT distortion in the transient 3D coherent superconductor, following the excitation was unknow [2,85]. We demonstrate that stripe order melting is prompt following near-infrared and mid-infrared photoexcitations, whereas the crystal structure follows significantly longer timescales and remains intact for moderate fluences.

In chapter 2 we discussed how in underdoped La$_{2-\text{x}}$Ba$_{\text{x}}$CuO$_4$, holes doped into the CuO$_2$ planes order along domain walls (stripes), separating regions of antiphase antiferromagnetic spin ordering. Concomitantly, the crystal structure distorts from the

---

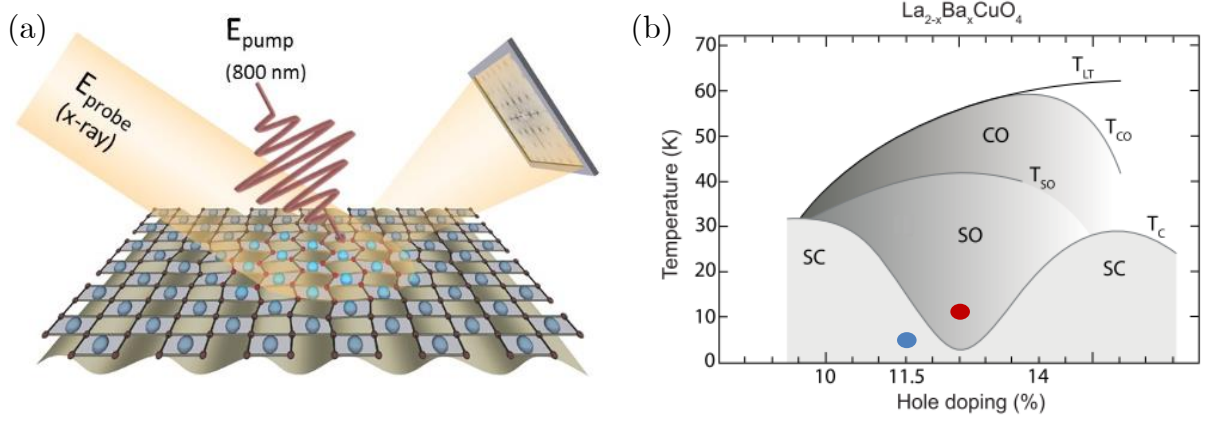[43] LESCO$_{1/8}$ exhibits an LTT phase below 135 K and charge stripe order below 25 K.

Figure. 6.1 (a) Schematic of the optical pump X-ray probe. (b) Phase diagram of La$_{2-x}$Ba$_x$CuO$_4$ as a function of temperature and doping as determined in [52]. Red and blue dots indicate the dopings of the samples investigated. SC, SO, and CO indicate the superconducting, spin-order, and charge- order states, respectively, with T$_C$, T$_{SO}$, and T$_{CO}$ being the corresponding transition temperatures. T$_{LT}$ represents the structural transition temperature.

low-temperature orthorhombic phase into the low-temperature tetragonal (LTT) phase, with the stripes mirroring the symmetry of the LTT phase and posited to be stabilized by the LTT distortion. As shown in Fig. 6.1(b) the emergence of superconductivity from the stripe phase for $0.09 \leq x \leq 0.16$ follows a peculiar double-dome phase boundary, with the superconducting transition temperature, T$_C$, greatly suppressed for x = 1/8 [52].

6.2 X-ray Absorption Spectroscopy

Single crystals of (LBCO$_{1/8}$) and (LBCO$_{11.5}$), grown using the traveling-solvent-floating zone method (see Appendix A.1) and cleaved to reveal the (001) surface, were used for our measurements. In LBCO$_{11.5}$, bulk superconductivity develops at T$_C \simeq 13$ K, spin-ordering at T$_{SO} \simeq 41$ K and charge ordering along with LTT structural distortion at T$_{CO} \simeq$ T$_{LTT} \simeq 53$ K. While in LBCO$_{1/8}$, bulk superconductivity is suppressed < 3 K, with T$_{SO} \simeq 42$ K and T$_{CO} \simeq$ T$_{LTT} \simeq 55$ K [61]. The lattice parameters of the unit cell of the high-temperature tetragonal (HTT) phase are $a_t \simeq 3.78$ Å and $c \simeq 13.2$ Å, with the scattering vectors specified as Q = (h k l) in all phases in units of $(2\pi/a_t$, $2\pi/a_t$, $2\pi/c)$. Static charge stripes are observed at a wave vector of Q = (0.23 0 0.65) for
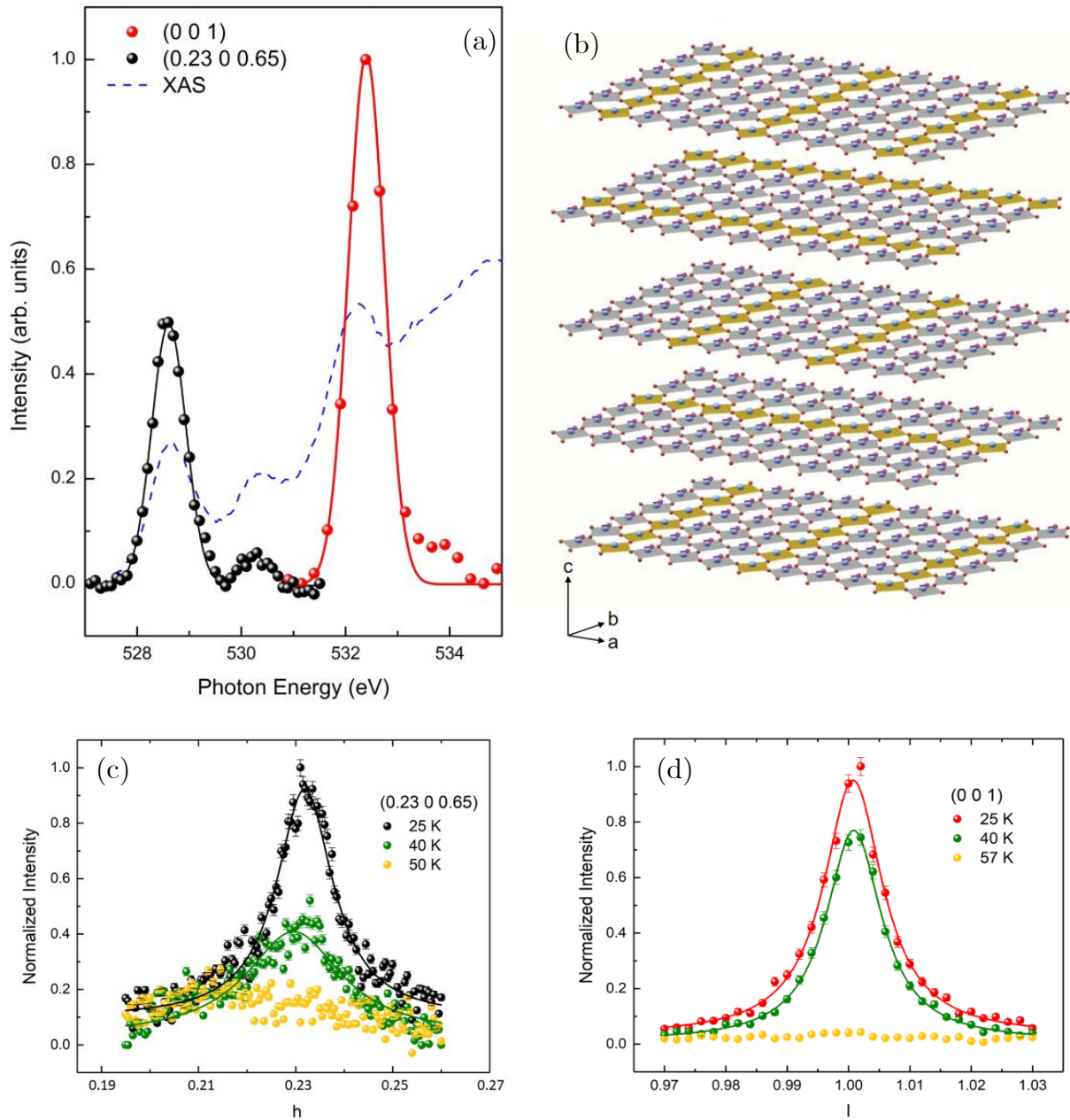
Figure 6.2 (a) XAS spectrum for La$_{1.885}$Ba$_{0.115}$CuO$_4$ over the O K edge (dashed blue line) along with the (0.23 0 0.65) charge-ordering diffraction peak (black circles) and (001) LTT distortion diffraction peak (red circles). The (0.23 0 0.65) peak has been scaled up by a factor of 3000. (b) Schematic of the stripe ordering (yellow polygons) in the CuO$_2$ planes. Temperature dependence of (c) stripe and (d) (001) peak. Solid lines represent Lorentzian fits to the data.

$LBCO_{11.5}$, and Q = (0.24 0 0.5) for $LBCO_{1/8}$ [60]. The structural distortion associated with the LTT phase has a screw axis along the *c*-direction[44], this allows for the observation of the (0 0 1) reflection, which is structurally forbidden at higher temperatures [86].

Figure 6.2(a) shows the energy dependence of the (0.23 0 0.65) stripe and (0 0 1) structural diffraction peaks as well as the X-ray absorption spectroscopy (XAS) spectrum across the O K edge recorded at T = 5 K. The resonances at 528.6 eV, along with the weak shoulder at 530.2 eV, corresponding to transitions into the O 2p doped hole states in the conduction band and the Cu 3d upper Hubbard band hybridized with O 2p states, respectively [57]. The (0 0 1) diffraction peak has a strong resonance at the O K edge, centered at 532.4 eV corresponding to resonant transitions into La-O hybridized states [86]. Therefore, the intensities of the (0.23 0 0.65) and (0 0 1) diffraction peaks are direct probes of the degree of stripe ordering and LTT distortion, which can be measured through resonant soft x-ray diffraction at the oxygen K pre-edge.

6.3 TR-RSXD: Near-infrared excitation in $La_{1.885}Ba_{0.115}CuO_4$

We first discuss TR-RSXD measurements on $LBCO_{11.5}$ performed at I06 beamline at Diamond where we probed the (0.23 0 0.65) and (0 0 1) peak, centered at 528.6 eV and 532.4 eV, respectively to 1.55 eV (800 nm) excitation. All measurements were carried out in the superconducting state (T ≃ 5 K). The TR-RSXD experimental setup at the I06 beamline has been reported in detail in sections 4.7-4.11.

The 1.55 eV pump pulses with a pulse duration of ∼ 250 fs from a Ti:Sa amplifier running at 22 KHz were polarized in the ab plane and were focused down to a spot size

---

[44] In the LTT phase neighboring CuO_2 planes are rotated by 90°, yielding O sites with different (rotated) local environments and affect the hybridization between the apical O and the La orbitals. On the other hand, in the LTO phase, neighboring CuO_2 planes are just shifted, not rotated, with respect to each other and the (0 0 1).

Figure: 6.3 (a) Intensity changes in the (0.23 0 0.65) charge-ordering diffraction peak (solid black circles) and (001) LTT distortion diffraction peak (solid red circles) following near-infrared photoexcitation using a pump fluence of 1.6 mJ/cm^2. The data were measured in for the open circle which represents the change in intensity of the low-α mode with an x-ray pulse width of ~7 ps (FWHM) except (0.23 0 0.65) diffraction peak for $\tau = 375$ ps recorded in hybrid represent fits to the data using an exponential function. mode with an x-ray pulse width of ~60 ps (FWHM). The solid lines represent fits to the data using an exponential function. Photoexcited (b) Stripe and (c) (001) peak at ~ 125 ps positive time delay measured in Hybrid mode. Solid lines represent Lorentzian fits.

of ~ 200 μm (FWHM) onto the sample. The X-ray probe pulses are also polarized in the ab plane (σ polarization) and focused to a spot size of ~ 100 μm. Since the penetration depth inside the sample at 1.55 eV and ~ 530 eV is the about same (~ 200 nm), a homogenous photoexcited volume is probed [38]. The change in diffraction peak intensities were measured using a gated micro-channel plate, which is insensitive to 1.55 eV photons.

In Fig. 6.3(a) the change in diffraction intensities relative to the fluorescence background ($\Delta I_\tau / I_0$) as a function of time delay (τ) for (0.23 0 0.65) and (0 0 1) peak is plotted, with the excitation fluence for both measurements kept at 1.6 mJ/cm^2. The results were recorded with the storage ring operating in low-α mode, for which the longitudinal width of the electron bunch was compressed to give a temporal resolution of ~ 7 ps at the expense of photon flux. As evident from Fig 6.3 both the (0.23 0 0.65) and (0 0 1) peaks are reduced in intensity by $\sim 40\%$, for the same pump fluence. However, the temporal response to the photoexcitation is different. An exponential fit to the stripe peak data (Fig. 6.3 (a), black line) gives a time constant of 10 ± 3 ps and is limited by the x-ray pulse width in the low-α mode of operation. The decay of the stripe peak likely occurs within only a few hundred femtoseconds of photoexcitation [84](discussed further in the next section). The (0 0 1) peak, on the other hand, is observed to decrease over a much slower timescale with an exponential fit (Fig. 6.3(b), red line) yielding a time constant of 77 ± 7 ps. We note here that the different responses of the two peaks precludes loss of intensity from sample heating from the laser pulses since $T_{CO} \simeq T_{LTT}$ (see Fig. 6.2 (c) and (d) showing temperature dependence of the stripe and (0 0 1) peaks).

Further insights regarding the disruption of stripe and LTT order can be retrieved from the pump fluence dependence of the relative change in intensities. Figure 6.4 shows $\Delta I_\tau / I_0$ for the stripe and LTT distortion diffraction peaks as a function of fluence for $\tau = 350$ ps. The results were recorded with the storage ring operating in hybrid mode with a temporal resolution of ~ 60 ps. Interestingly, at ~ 0.8 mJ/cm^2 the melting of the stripe ordering saturates whereas the LTT distortion remains largely intact, which
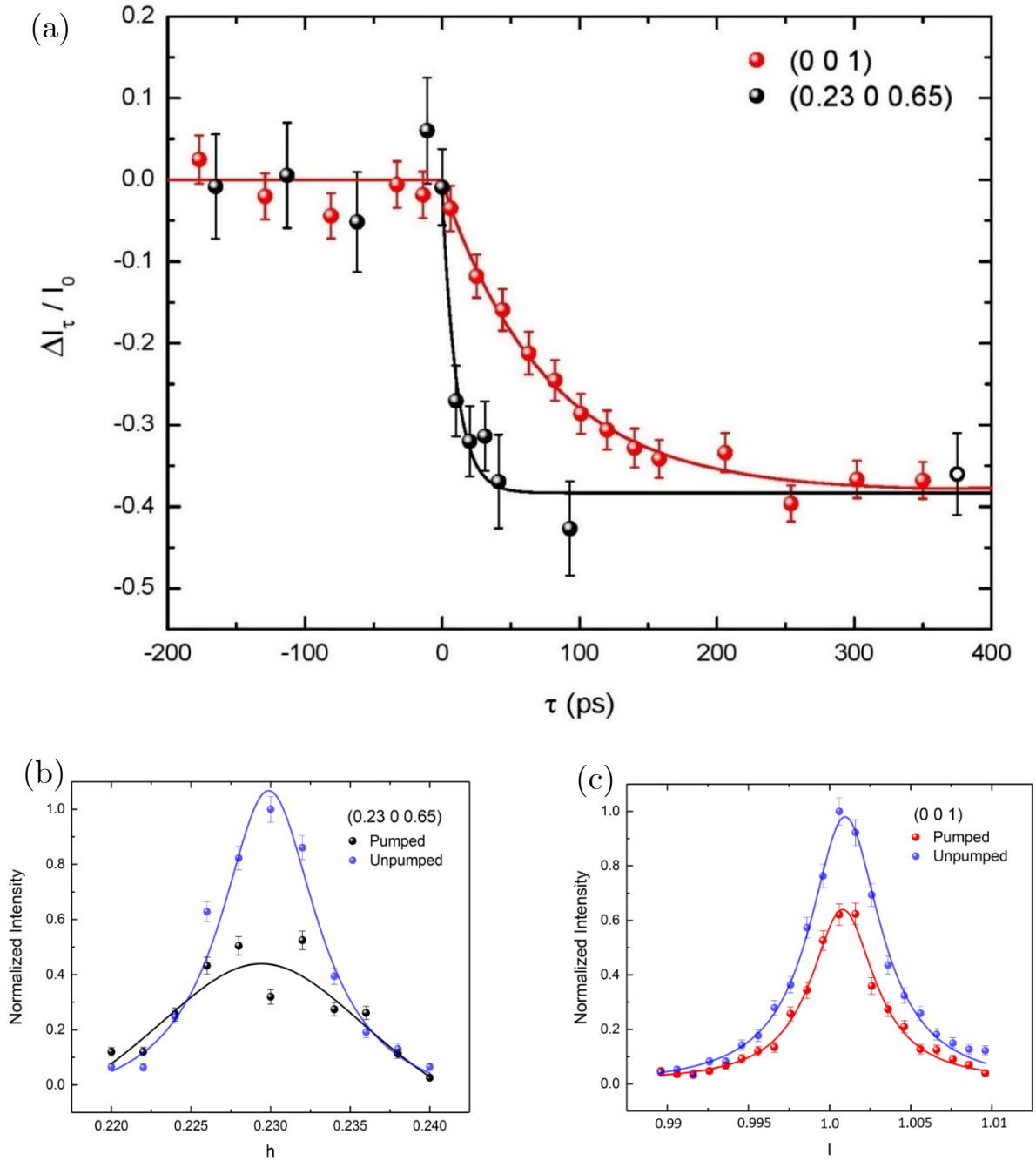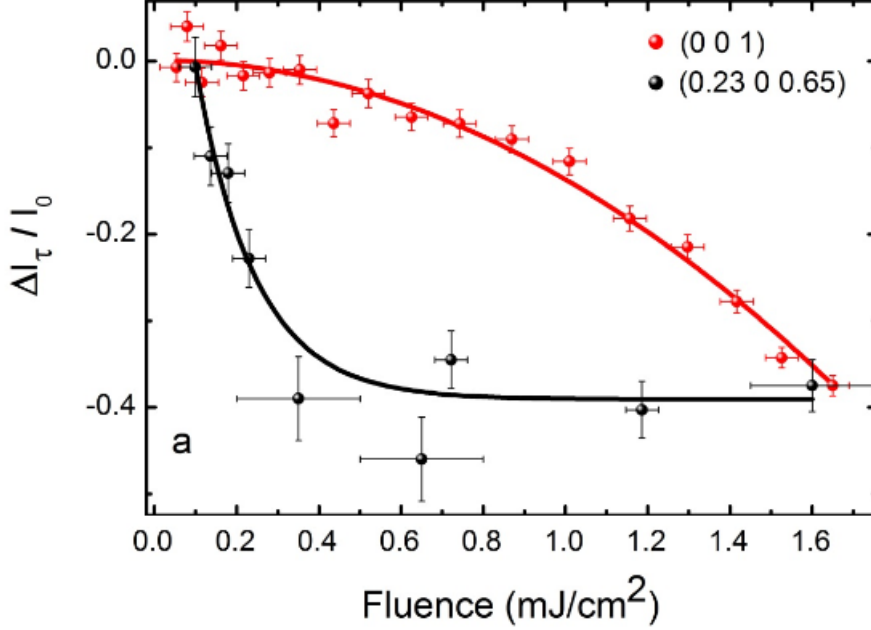
85

Figure. 6.4 Fluence dependence of the (0.23 0 0.65) charge-ordering diffraction peak (solid black circles) and (001) LTT distortion diffraction peak (solid red circles) intensity after photoexcitation with $\tau = 350$ ps. The error in the fluence indicates the uncertainty in the pump beam diameter at the sample position. The red line shows a quadratic fit whereas the black line shows an exponential fit to the data.

should remain the case for the shortest picosecond timescales inaccessible for synchrotron-based TR-RSXD.

Our experiments demonstrate that photoexcitation using near-infrared 1.55 eV pulses creates a charge transfer nonequilibrium phase in which the LTT distortion remains intact, but the stripe ordering is strongly suppressed. Given that the measurements were carried out in the superconducting state, this then gives a unique system with which to explore the emerging dynamics of superconductivity once stripe order is disrupted. The photoinduced dynamics of the superconducting state with identical excitation conditions are reported in chapter 7.

6.4 TR-RSXD: Mid-infrared excitation in La$_{1.875}$Ba$_{0.125}$CuO$_4$

We used femtosecond resonant soft x-ray diffraction at a free electron laser (FEL) to directly probe the dynamics of both the stripe order and the LTT distortion in the stripe-ordered cuprate LBCO$_{1/8}$ following a mid-infrared pump, tuned to resonantly excite the 85 meV (14.5 μm) infrared-active, in-plane Cu-O stretching mode [38].

The experiments were performed at the SXR beam line of the Linac Coherent Light Source (LCLS) [87,88]. A schematic drawing of the experimental setup is shown in Fig. 6.5(A). The sample was held at base temperature T = 13 K in the stripe-ordered, LTT-distorted phase. Femtosecond midinfrared pulses (85 meV), derived from an optical parametric amplifier and subsequent difference frequency mixing, were used for excitation. The excitation pulses were 200 fs long, polarized in the ab plane, and focused onto the sample with a spot size of 700 μm. In our experiments, the excitation fluence was kept at 1.9 mJ/cm^2, equal to the conditions of the light-induced superconductivity transition studied in LESCO$_{1/8}$ [2].

X-ray pulses of sub-100 fs duration, tuned to photon energies of 528 eV and 532 eV for the (0.24 0 0.5) and (0 0 1) wave vectors, respectively, were selected by a grating monochromator providing a bandwidth of approximately 1.5 eV. The X-ray beam was aligned collinearly with the mid-IR pump and focused onto the sample with a 200 μm diameter (see Fig 6.5(A)). Since extinction depth of the mid-IR at the phonon resonance is 1–2 μm and that of the x-ray pulses at the oxygen K edge is approximately 200 nm, a homogenously pumped sample volume is probed by the X-rays. A high-vacuum diffraction chamber, equipped with a fast- readout CCD camera, was used for the experiments [89]. The measurements were performed with a 60 Hz repetition rate. The time resolution of this experiment was 300 fs, limited by the timing jitter between the synchronized X-ray and optical laser pulses.

The time-dependent response of the (0.24 0 0.5) stripe order diffraction peak to the optical excitation is shown in Fig. 6.5(B). The upper panel shows the diffracted X-ray beam, recorded with the CCD camera and averaged over about 20 000 FEL shots. At negative time delays, a broad and rather weak peak is observed on the CCD camera, consistent with the short correlation length of the stripe order in LBCO$_{1/8}$ [60,90]. The lower panel shows the integrated transient intensity of this diffraction peak. The integrated diffraction intensity of this peak promptly decreases by about 70% after the arrival of the mid-IR excitation. These results show that stripe order is melted on a subpicosecond time scale by these mid-IR pulses. The red solid line represents a single-
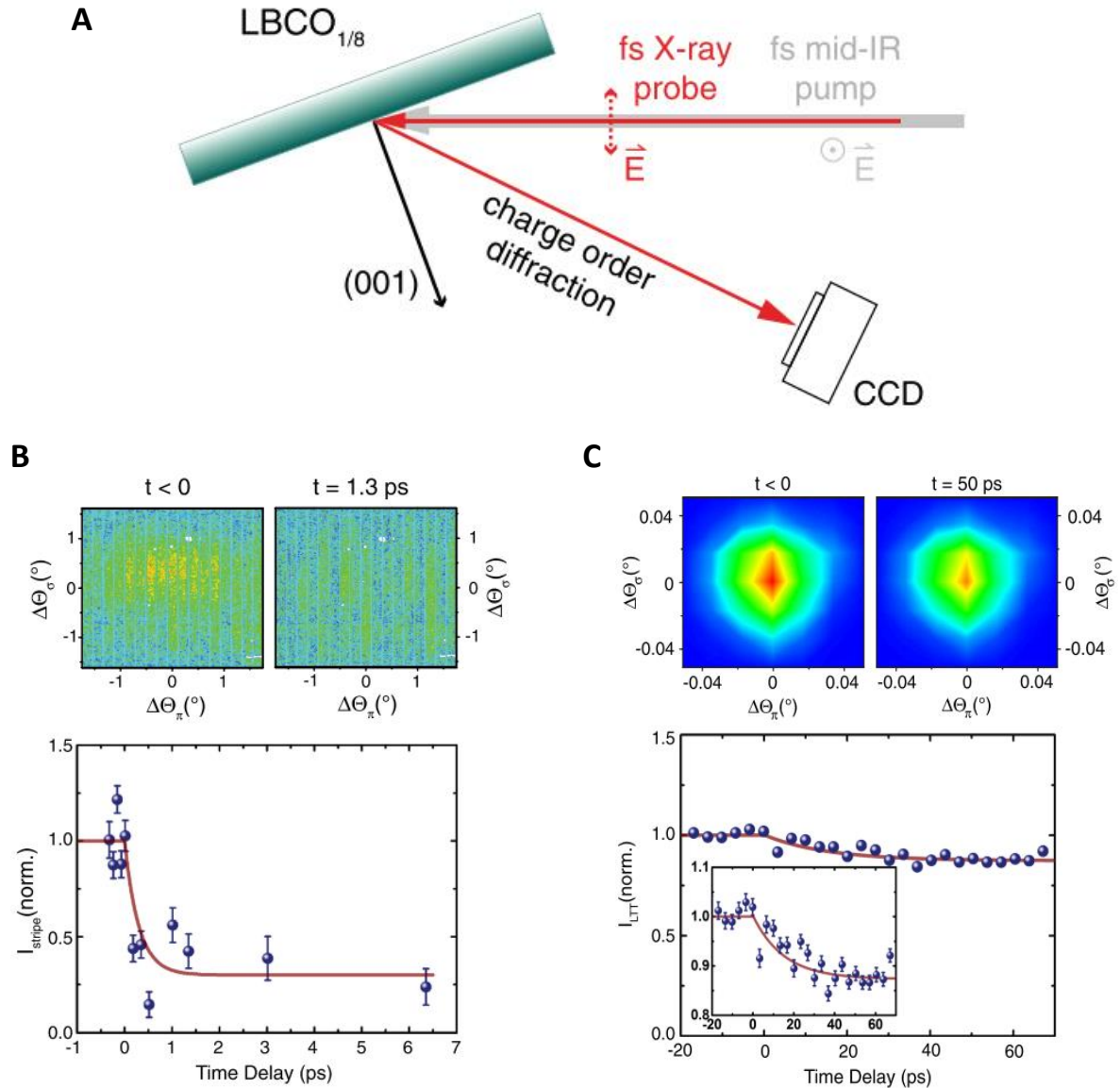
Figure. 6.5 (A) Top view of the experimental setup, shown for the diffraction condition of the charge stripe order peak.

(B) Transient intensity of the charge stripe order diffraction peak in (001) cleaved $La_{1.875}Ba_{0.125}CuO_4$ measured at the (0.24 0 0.5) wave vector. Resonant mid-IR excitation with 1.9 mJ/cm² fluence at positive time delay results in a prompt decrease of the scattered intensity on the sub-ps time scale. The red solid line represents an exponential function with a time constant set to 300 fs, i.e., the resolution of the experiment. The upper panel shows the diffracted spots, recorded with the CCD camera and averaged over about 20 000 FEL shots, at negative and positive time delays.

(C) Light-induced changes in the intensity of the (001) diffraction peak reflecting the LTT distortion. Again, the $La_{1.875}Ba_{0.125}CuO_4$ crystal is excited with the 1.9 mJ/cm² fluence of midinfrared light. The red solid line is a single exponential fit to the data yielding a time constant of 15 ps. The inset shows the same data set with an expanded y axis. The diffraction spots recorded on the CCD, averaged over 400 FEL shots for a positive and a negative time delay, are shown in the upper panel.

exponential function used to visualize the reduction of the scattering intensity, with a time constant set to the 300 fs time resolution of the experiment. The fast timescale observed here is similar to the one observed in the $LESCO_{1/8}$ THz probe experiments, implying that the ultrafast formation of the superconducting state and the melting of charge modulations are connected.

In contrast, the evolution of the LTT phase, as probed by the (001) diffraction peak, is very different from that of the stripe order. CCD images of this diffraction peak, averaged over 400 FEL shots taken at a positive and a negative time delay, are shown in Fig. 6.5(C). The integrated scattered intensity of this structural (and therefore sharp and intense) peak drops by only 12%, and on a much longer time scale. A single-exponential decay fitted to the data (red solid line) yields a time constant of 15 ps. This time scale is likely set by acoustic propagation, as the relaxation of the LTT distortion requires the lattice planes to expand, a process that is limited by the speed of sound.

Here too, our experiments demonstrate that the resonant mid-IR excitation in $LBCO_{1/8}$ triggers the ultrafast formation of a nonequilibrium state in which stripe charge correlations have disappeared while the LTT distortion still exists. This decoupling is not present in the equilibrium phase diagram of LBCO.

Given the prompt appearance of 3D superconductivity in $LESCO_{1/8}$ under identical conditions, the present results support the conclusion that it is the stripe order and not the LTT distortion which is responsible for the suppression of the 3D coherent super-conducting state [62]. These results are also consistent with the scenario of a system which, in the presence of stripe order, is a 2D superconductor. In this case, the superconductivity is proposed to be in the form of a pair density wave state, where the superconducting order parameter is modulated by the periodic potential resulting from the charge order, with twice the period [91]. This, and the 90° rotation of the charge stripes along the c axis, provides a natural explanation for the destructive interference of the Josephson currents. In this scenario, when the mid-IR pulse melts the charge

order, it removes the periodic potential. At that point, the superconducting condensates are free to coherently couple along the c axis and do so on a time scale of the Josephson plasma resonance, i.e., a few hundred femtoseconds, resulting in the emergence of a transient 3D superconducting state.

7 Photoinduced Enhancement of Josephson coupling in $La_{1.885}Ba_{0.115}CuO_4$

7.1 Introduction

In this chapter we present results showing the transient enhancement of Josephson interlayer coupling in $LBCO_{11.5}$. The effects of optical excitation on LBCO are studied with THz time domain spectroscopy which can probe the response of the superconducting condensate at its natural energy scale. In our experiments, $LBCO_{11.5}$ was excited with 1.55 eV (800 nm) femtosecond laser pulses polarized either parallel (E ∥ *ab* plane) or perpendicular (E ∥ c axis) to the CuO_2 planes. For in-plane excitation, since the pump wavelength, polarization and fluence used in the resonant X-ray diffraction and THz time domain measurements is the same, this allows us to build a comprehensive and complementary picture of the resulting electronic and structural dynamics in the $LBCO_{11.5}$ system. Furthermore, by varying the polarization of the near-infrared pump we can compare the efficiency of the enhancement of the interlayer coupling for different excitation protocols.

As mentioned previously, above-gap charge excitation at near-infrared and visible wavelengths has been extensively studied in conventional and high-temperature superconductors in the past. Typically, the pump fluences used in such studies was $\lesssim$ 10 $\mu J/cm^2$, which is sufficient to destroy the superconducting condensate and investigate its recovery dynamics. Ultrafast studies on high-T_c superconductors with probing frequencies in the near- and mid-infrared range helped identifying the intrinsic timescales of the response dynamics of the superconducting condensate as well as of pseudogap correlations [70]. In addition, by probing the response to above-gap

excitations in the THz frequency range, one can study the dynamics of excess quasiparticles and condensate recovery on the energy scale of the superconducting gap [70,71]. The umbrella of these experiments shed light on evolution of superfluid density after photoexcitation by examining the breaking and recombination of Cooper pairs.

Instead, here we photoexcite a 'frustrated' high-T_c cuprate, exhibiting coexisting/competing orders, with much higher laser fields (fluences up to 2 mJ/cm^2) with a goal to directly melt the electronic order (stripes), which frustrates interlayer phase coherence at equilibrium, and probe the underlying superconducting condensate using transient reflectivity at THz frequencies.

7.2 Equilibrium Optical Response

La$_{1.885}$Ba$_{0.115}$CuO$_4$ single crystal investigated in our THz spectroscopy study was grown using traveling-solvent floating-zone method[45]. The crystal was cut and polished, thus exposing an ac-oriented surface of $\sim$ 10 mm^2 area, which was sufficient to perform long-wavelength THz spectroscopy. As shown in the temperature vs doping phase diagram of La$_{2-x}$Ba$_x$CuO$_4$ in Fig. 7.1(b), LBCO$_{11.5}$ undergoes a superconducting transition at T_c $\simeq$ 13 K, spin-ordering at T_{SO} $\simeq$ 42 K and charge ordering along with the LTT distortion at T_{CO} $\simeq$ T_{LTT} $\simeq$ 53 K.

The equilibrium optical properties were determined using single-cycle THz pulses generated by illuminating a large-area photoconductive antenna with near-infrared laser pulses from a Ti:Sa amplifier. The THz pulses were focused onto the sample surface to a spot size of $\sim$ 1 mm diameter and incident at an angle of 30°, with polarization perpendicular to the CuO$_2$ planes (E∥c axis). The reflected electric field from the sample, $E_R(t)$, was measured both above and below T_c, by electro-optical sampling in a 1-mm thick $ZnTe$ crystal. $E_R(t)$ was then Fourier transformed to obtain the complex-valued, frequency dependent $\tilde{E}_R(\omega)$.

---

[45] From the same batch of crystals that were used for TR-RSXD measurements reported in chapter 6. An overview of the traveling-solvent floating-zone method is presented in appendix A.1.
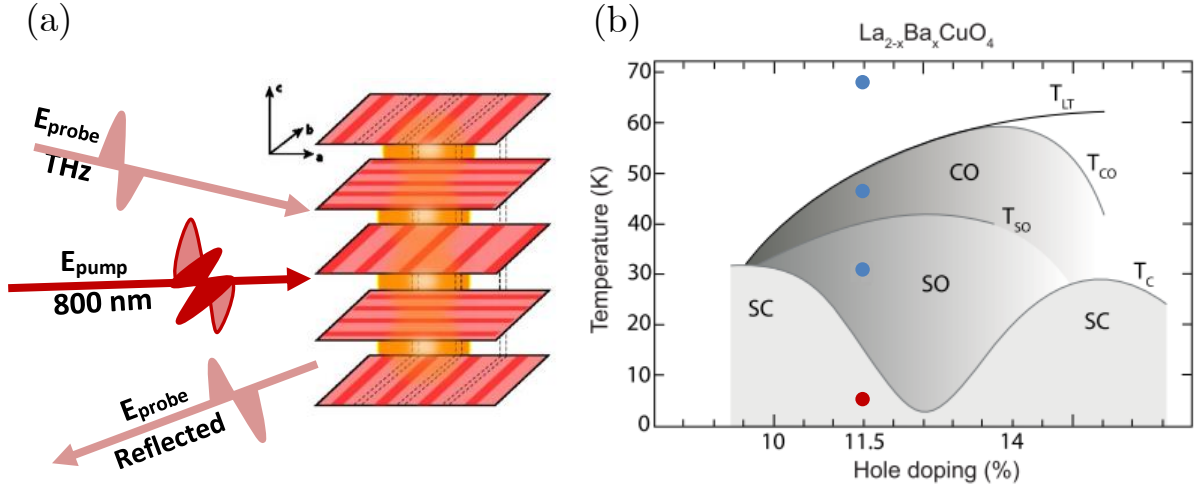
Figure 7.1 (a) Schematic of the pump-probe set up used for the THz time domain spectroscopy. (b) Phase diagram of $La_{2-x}Ba_xCuO_4$ as a function of temperature and doping as determined in [52]. SC, SO, and CO indicate the superconducting, spin-order, and charge- order states, respectively, with T_c, T_{so}, and T_{co} being the corresponding transition temperatures. T_{LT} represents the structural transition temperature. The circles indicate the different temperatures for which the data is reported here. Below T_c (dark red) the sample was photoexcited with both in- and out-of-plane pump polarizations. At higher temperatures (blue circle) the sample was only pumped out-of-plane.

The out-of-plane equilibrium reflectivity of the superconducting state, $R(\omega, T < T_c)$ was determined as $R(\omega, T < T_c) = \frac{|\tilde{E}_R(\omega, T < T_c)|^2}{|\tilde{E}_R(\omega, T \gtrsim T_c)|^2} R(\omega, T \gtrsim T_c)$. Here, $R(\omega, T \gtrsim T_c)$ is the normal-state reflectivity measured with Fourier-Transform Infrared Spectroscopy on the same sample, which is completely flat and featureless in the THz range, Fig. 7.2(b.1). The datasets were then fitted with the model that describes the optical response of a Josephson plasma and merged at $\omega \simeq 2.5\,\text{THz}$ with the broadband spectra from Ref. [38]. By performing Kramers-Kronig (KK) transformations on the full spectrum we were able to retrieve the complex equilibrium optical response functions like optical conductivity $\tilde{\sigma}_0(\omega)$, dielectric function $\tilde{\varepsilon}_0(\omega)$ and refractive index $\tilde{n}_0(\omega)$.

The in- and out-of plane, equilibrium reflectivity and the real part of the optical conductivity σ_1 above and below T_c for $LBCO_{11.5}$, retrieved with this procedure, are shown in Fig. 7.2. The weak interlayer superconducting coupling of $LBCO_{11.5\%}$ results in an equilibrium Josephson Plasma Resonance (JPR) at ~ 0.2 THz, which shows up as an edge in the c-axis reflectivity [Fig. 7.2(b.1)].
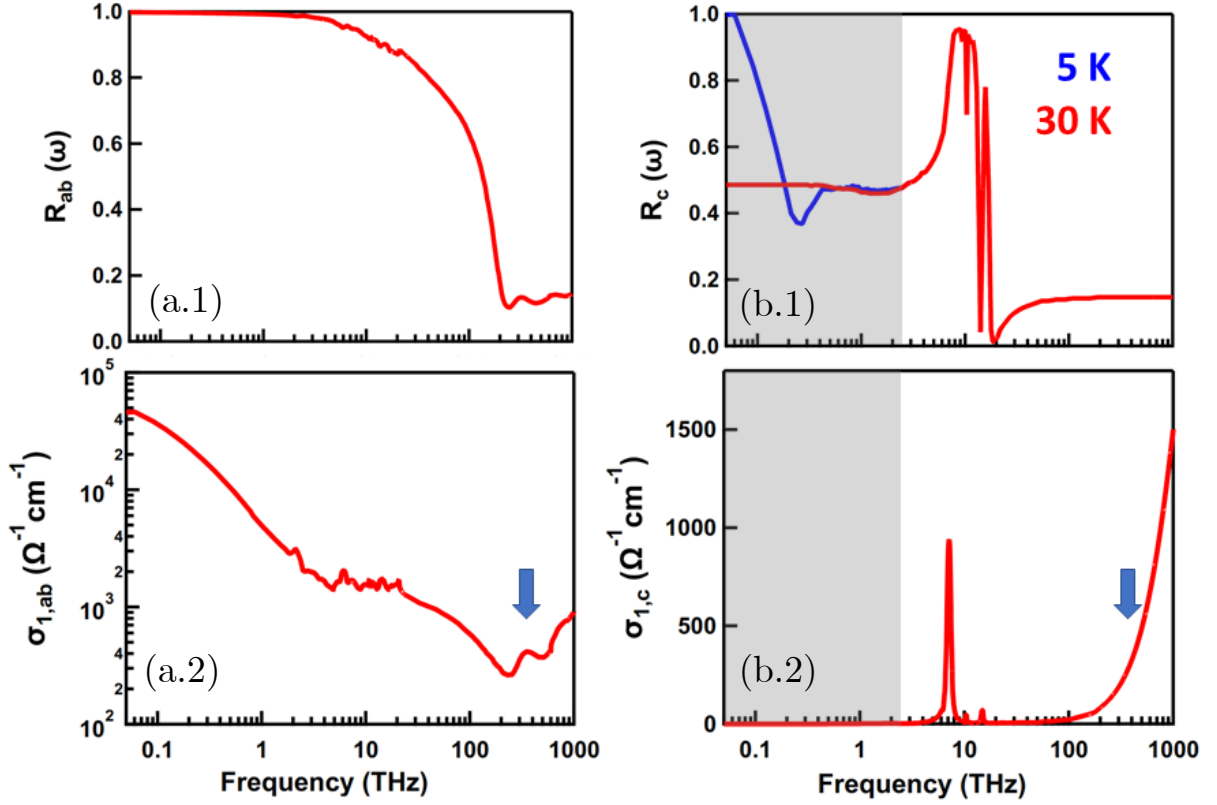
Figure 7.2 C-axis and in-plane optical properties of $La_{1.885}Ba_{0.115}CuO_4$ at equilibrium: Frequency-dependent reflectivity [panels (a.1) and (b.1)] and real part of the optical conductivity $\sigma_1(\omega)$ [panels (a.2) and (b.2)]. The spectral region probed in the current experiment is highlighted in gray. The blue arrow indicates the pump wavelength (800 nm) used for excitation.

We stress here that, to our knowledge, this measurement is the first direct observation of a JPR in LBCO$_{11.5}$, as conventional Fourier-transform spectroscopy techniques can hardly yield enough spectral weight down to such low frequencies.

Out-of-plane superconducting transport is also observed as a small low-frequency divergence of the imaginary part of the conductivity, which can be seen in the gray line in Fig. 7.3(b). An increase in a positive $\sigma_2(\omega \rightarrow 0)$ with decreasing frequency is indicative of perfect transport. Although $\sigma_2(\omega)$ scales as $1/\omega$ in an ideal superconductor, in the cuprates it can deviate from this behavior due to the combined effect of the condensate and quasiparticle tunneling [30].

For completeness, we also report in Fig. 7.2 [panels (a.1) and (a.2)] the corresponding in-plane reflectivity and optical conductivity of LBCO from Ref. [38], where we indicate

with an arrow the frequency of our excitation pulses. Unlike the out-of-plane direction, the response parallel to the plane is clearly that of a metal ($T>T_C$), being characterized by a very high reflectivity (close to unity) toward low frequencies, and by a Drude peak in $\sigma_1(\omega)$.

7.3 Evaluation of transient optical properties

To measure the transient response of the sample after photoexcitation, we employed the same THz time-domain spectroscopy geometry used for the equilibrium characterisation. The sample was irradiated at normal incidence with optical pulses of $\sim$ 100 fs duration and 800 nm wavelength from the same Ti:Sa amplifier which is used to seed the THz generation. These optical "pump" pulses were focused on a $\gtrsim$2-mm-diameter. Their polarisation and fluence was controlled by a polarizer – waveplate combination. THz pulses were used to probe the pump-induced reflectivity changes for frequencies between $\sim$ 0.15 - 2.0 THz.

To measure the pump-induced change, $\Delta E_R(t,\tau) = E_R^{pumped}(t,\tau) - E_R(t)$, the THz electric field was acquired at each pump-probe time delay τ. The electro-optic sampling signal was filtered with a lock-in amplifier, triggered at the frequency of a mechanical chopper used to modulate the optical pump. This measurement yields "pump ON" minus "pump OFF" reflected electric field[46].

The stationary field $E_R(t)$, was determined for each measurement by chopping the probe beam while keeping the pump ON at negative time delay, that is $E_R(t,\tau \ll 0)$. Since the pump power hitting the sample at negative delays is the same as that used to determine $\Delta E_R(t,\tau)$, this procedure allowed us to account for possible average heating effects.

The differential electric field $\Delta E_R(t,\tau)$ and the stationary reflected electric field $E_R(t)$ were then independently Fourier transformed to obtain the complex-valued, frequency

---

[46] The time delay t, refers to the delay between the THz pulse and the optical sampling pulse and maps out the THz field reflected off the sample.

dependent $\Delta\tilde{E}_R(\omega,\tau)$ and $\tilde{E}_R(\omega)$. The complex reflection coefficient of the photo-excited material, $\tilde{r}(\omega,\tau)$, was determined using the relation,

$$\frac{\Delta\tilde{E}_R(\omega,\tau)}{\tilde{E}_R(\omega)} = \frac{\tilde{r}(\omega,\tau) - \tilde{r}_0(\omega)}{\tilde{r}_0(\omega)} \tag{7.1}$$

here $\tilde{r}_0(\omega)$ is the stationary reflection coefficient and was extracted from the equilibrium optical properties as described in section 7.2.

Due to the mismatch between the penetration depth, $d(\omega) = \frac{c}{2\omega.\mathrm{Im}[\tilde{n}_0(\omega)]}$, of the THz probe $[\mathrm{d}(\omega \simeq 0.15 - 2.5\,\mathrm{THz}) \simeq 50 - 500\,\mu\mathrm{m}]$ and that of the optical pump $[\mathrm{d}(\omega \simeq 375\,\mathrm{THz}) \simeq 0.1\,\mu\mathrm{m}$ for E ∥ ab, and $\simeq 0.4\,\mu\mathrm{m}$ for E ∥ c] the raw pump-induced reflectivity changes were only $\sim 0.5 - 1\%$. This mismatch was corrected by modelling the response of the system in the thin film limit, where we considered a thin homogenously photo-excited layer sitting above an unperturbed bulk. The complex reflection coefficient of such a multilayer system is expressed as [82]:

$$\tilde{r}(\omega,\tau) = \frac{\tilde{r}_A(\omega,\tau) + \tilde{r}_B(\omega,\tau)e^{2i\delta(\omega,\tau)}}{1 + \tilde{r}_A(\omega,\tau)\tilde{r}_B(\omega,\tau)e^{2i\delta(\omega,\tau)}} \tag{7.2}$$

Here $\tilde{r}_A(\omega,\tau)$ and $\tilde{r}_B(\omega,\tau)$ are the reflection coefficients at the interfaces vacuum/photoexcited layer and photoexcited layer/unperturbed bulk, respectively, while $\delta = 2\pi d\tilde{n}(\omega,\tau)/\lambda_0$ (here, $\tilde{n}(\omega,\tau)$ is the complex refractive index of the photoexcited layer and λ_0 is the probe wavelength).

Eq. 7.2 can be solved numerically, thus retrieving $\tilde{n}(\omega,\tau)$ from the experimentally determined $\tilde{r}(\omega,\tau)$. The complex optical conductivity for a volume that is homogenously transformed can then be calculated using the following relation,

$$\tilde{\sigma}(\omega,\tau) = \frac{\omega}{4\pi i}[\tilde{n}(\omega,\tau) - \varepsilon_\infty]. \tag{7.3}$$

Where ε_∞ represents the screening by interband transitions. For high-T_c cuprates the standard value of $\varepsilon_\infty = 4.5$ [83].
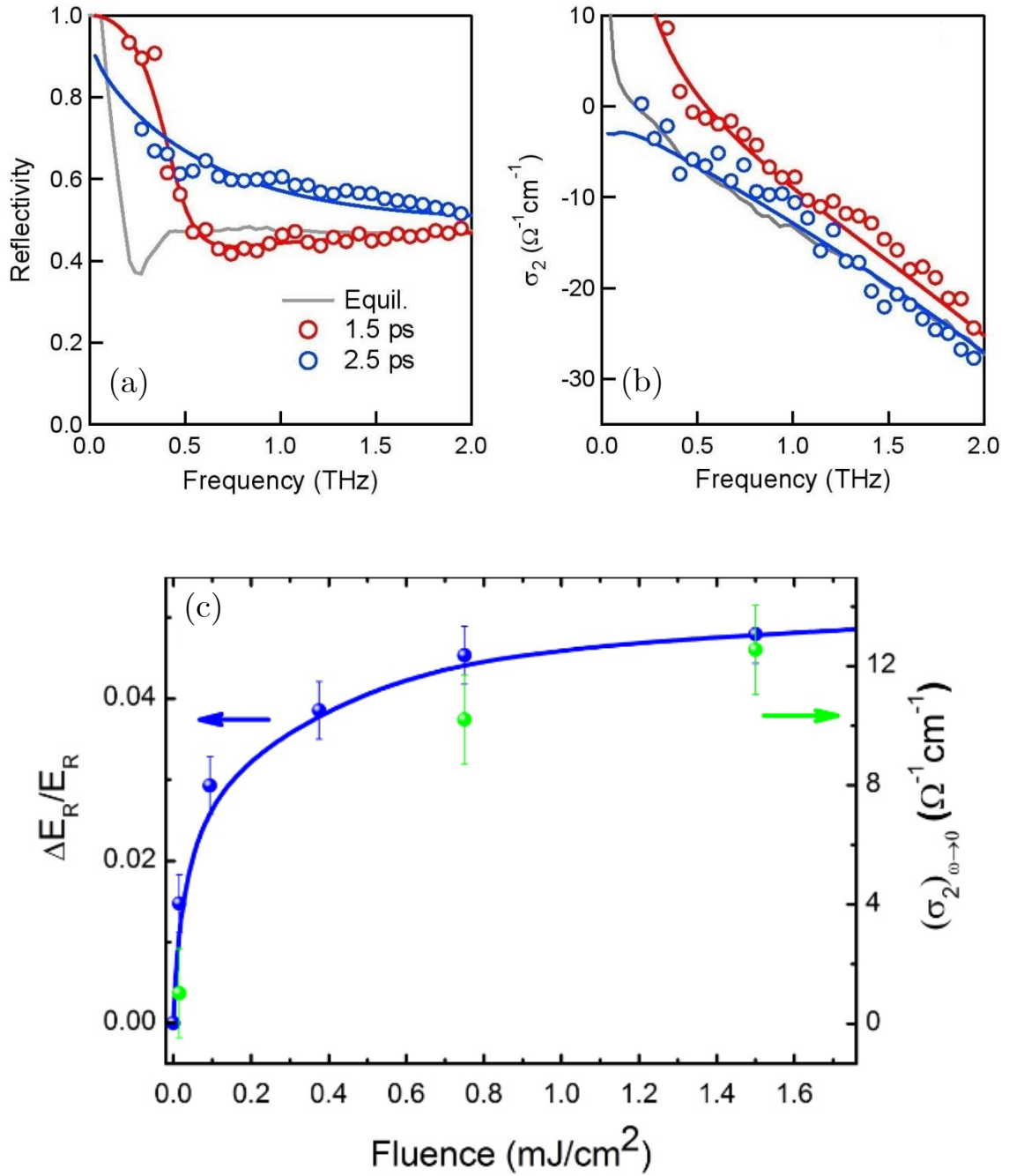
Figure 7.3 (a) Normal-incidence reflectivity and (b) imaginary optical conductivity (σ_2) of LBCO$_{11.5}$ measured with THz time-domain spectroscopy 1.5 ps (red circles) and 2.5 ps (blue circles) after near-infrared optical excitation. The same quantities measured at equilibrium are displayed as gray lines. Red and blue lines are fits to the data performed with a superconducting and Drude model, respectively. (c) Changes in the electric field, $\Delta E_R/E_R$ (solid blue circles) and $(\sigma_2)_{\omega\to 0}$ (solid green circles) as a function of fluence (frequency = 0.2 THz, τ = 1.5 ps). The blue line shows a fit using an exponential function.

Note that the temporal resolution of our experiment (~350 fs) is limited by the duration of the pump pulse and by the inverse bandwidth of the probe pulse. In all our measurements, since the signal develops in ~ 1.5-2 ps, and the relaxation occurs within ~ 3-5 ps, the possibility of any spectral deformation is negligible [92].

7.4 Near-infrared excitation parallel to the Cu-O planes

We first discuss results of in-plane near-infrared (1.55 eV) excitation. The c-axis transient reflectivity and imaginary conductivity σ_2 spectra, measured 1.5 ps time delay after photoexcitation, are shown in Fig. 7.3 (red circles) for a pump fluence of ~2 mJ/cm^2. Remarkably, the plasma resonance displays a prompt blue shift from ~ 0.25 THz to ~ 0.5THz (Fig. 7.3(a), red circles). Correspondingly, an enhancement of σ_2 is observed which reflects an increase in interlayer Josephson coupling (Fig. 7.3(b), red circles).

At $\tau = 2.5$ ps we observe a relaxation to a state in which coherence is reduced, characterized by a broader edge in reflectivity (Fig. 7.3(a), blue circles) and the absence of a divergence in σ_2 (Fig. 7.3(b), blue circles). The transient spectra could be fitted assuming a superconducting model for $\tau = 1.5$ ps (Fig. 7.3, red lines), while in the relaxed state a Drude model with a finite carrier scattering time in the picosecond range had to be employed (Fig. 7.3, blue lines). A more detailed explanation of the fitting procedure for the above datasets is given in sections 7.5 and appendix A.2.

Importantly, we take here the low-frequency limit of the imaginary part of the conductivity $(\sigma_2)_{\omega \to 0}$, as well as the change in the reflected electric field at the peak of the THz response $\Delta E_R/E_R$ to estimate the fluence-dependent Josephson interlayer coupling. As shown in Fig 7.3(c), both these quantities show signatures of a saturation ~ 0.8 mJ/cm^2, suggesting a threshold for enhancement in the interlayer coupling.

The enhancement of the superconducting response upon above gap optical excitation is surprising given that the process certainly generates high-energy hot quasiparticles [70]. For LBCO$_{11.5}$, one may rationalize the process occurring here as follows: First, the

frustration of interlayer Josephson coupling due to the competing stripe phase is presumably removed by optical excitation, which promptly melts the charge order. This leads to an enhancement of the superconducting response (blue shift of the plasma resonance). Only at later delays, the role of hot quasiparticles sets in, resulting in a broadening, and eventually in the disappearing of the plasma resonance.

Notably, since light polarized out-of-plane is supposed to couple less efficiently to quasiparticle excitations in quasi-2D superconductor like high-T_c cuprates, whilst still perturbing the competing stripe phase, we have decided to also explore this different excitation geometry with the goal of optimizing optically enhanced superconductivity in LBCO.

7.5 Optimising enhancement of interlayer coupling by near-infrared excitation

The c-axis transient reflectivity, [Fig. 7.4 panels (a.1), (b.1), (c.1), (d.1)] measured 1.5 ps (red) after photoexcitation for a pump fluence of ~ 2 mJ/cm^2 is displayed alongside the same quantity at equilibrium (gray). Here, unlike the case of in-plane excitation (see previous Section), we have extended our study to carefully determine the temperature dependence of the transient dynamics, crossing all relevant phases in this compound.

Below T_C [panel (a.1)] a prompt blue shift of the equilibrium JPR from ~ 0.2 to 0.6 THz was observed after out-of-plane excitation, similar to that reported for in-plane pumping [see Fig. 7.3 (a)]. Even more remarkably, in the spin-ordered phase [panel (b.1)] above T_C, where no edge is observed at equilibrium, an edge appeared at $\sim$0.5 THz immediately after photoexcitation. A similar effect, although less evident, was present also above T_{SO} [panel (c.1)], where a reflectivity edge appeared near $\sim$0.4 THz. No appreciable photoinduced dynamics could be measured above T_{CO} [panel (d.1)].

The combined coherent and incoherent response of the photoexcited state can captured by plotting the frequency- and time-delay-dependence of the energy loss function $-\mathrm{Im}[(1/\tilde{\varepsilon}(\omega, \tau)]$. The loss function exhibits a peak where $\tilde{\varepsilon}$ crosses zero, that is, at the
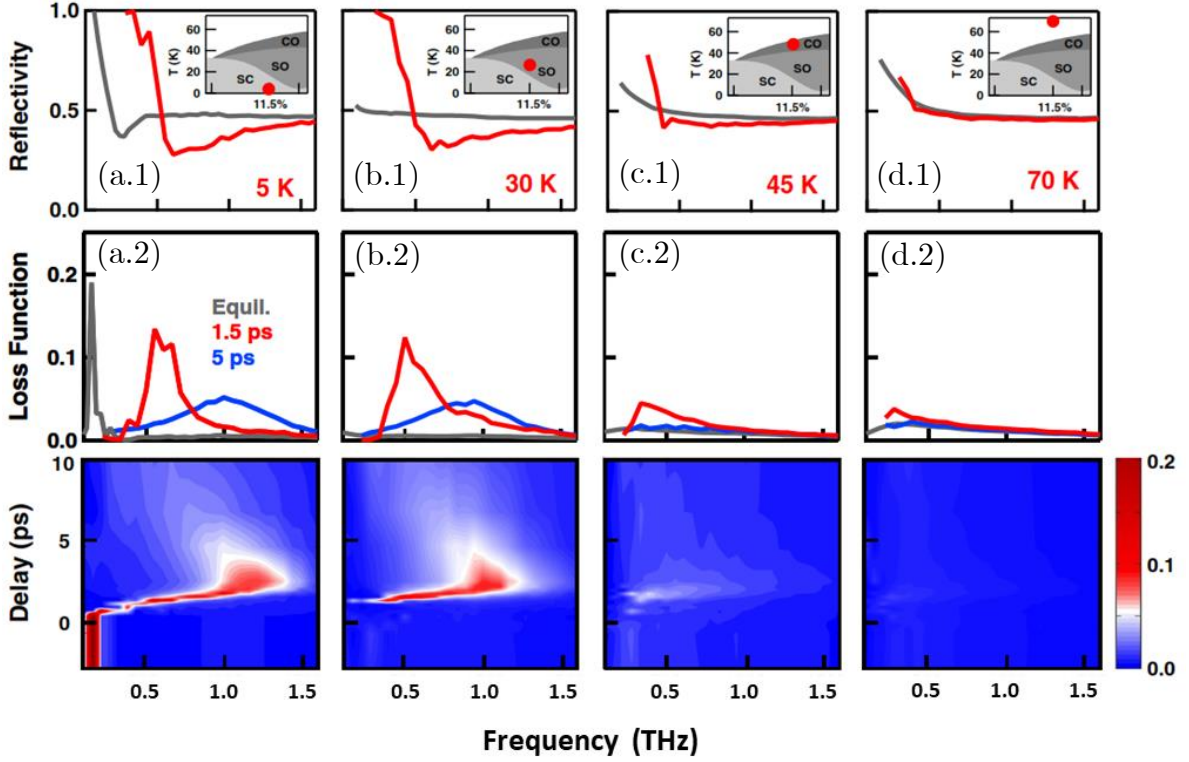
Figure 7.4. THz reflectivity of LBCO displayed at different temperatures at equilibrium (gray) and 1.5 ps after excitation (red). Data in panels (a) and (b) have been taken with a pump fluence of ~2 mJ/cm^2 (a saturation in the fluence dependence of the pump-induced changes was found above ~1 mJ/cm^2). Energy loss function $-\text{Im}[(1/\tilde{\varepsilon}(\omega,\tau)]$ of La$_{1.885}$Ba$_{0.115}$CuO$_4$ as a function of temperature and pump-probe delay. The lower panels show its evolution throughout the light-induced dynamics. The middle panels show selected line cuts at negative (gray), +1.5 ps (red), and +5 ps (blue) time delay.

the frequency of the plasma resonance. The width of the loss function reflects the scattering rate or, equivalently, the inverse coherence length for superconducting tunneling. The complete time-dependent response of the energy loss function $-\text{Im}[(1/\tilde{\varepsilon}(\omega,\tau)]$ is shown in the color plots of Fig. 7.4 while selected line cuts (showing specific time delays) are shown in the panels [(a.2), (b.2), (c.2), (d.2)].

Below T$_C$ the loss-function peak was found to continuously shift from its equilibrium value (~ 0.2 THz) toward higher frequencies, up to ~ 1.2 THz (at ~ 2.5 ps delay) before relaxing back to lower values. Also, for T$_C$ <T <T$_{SO}$ [panel (b.2)] a well-developed loss-function peak (absent at equilibrium), appeared in the perturbed material, continuously broadening and shifting first to the blue and then to the red at

longer time delays. All light-induced effects progressively reduce with increasing T and completely disappear after crossing T_{CO} [panels (c.2) and (d.2)].

Further analysis is reported in Fig. 7.5, where the transient optical conductivity $\sigma_1(\omega) + i\sigma_2(\omega)$ is displayed for T = 5 K [panels (a.1) and (a.2)], and T = 30 K [panels (b.1) and (b.2)] at three selected pump-probe delays: $\tau < 0$ (equilibrium), $\tau = 1.5$ ps, and $\tau = 5$ ps. In the superconducting state at equilibrium, a fully gapped $\sigma_1(\omega)$ [Fig. 7.5(a.1), gray curve] and a $\sigma_2(\omega)$ that turns positive and increases with decreasing ω is shown [Fig. 7.5(a.2), gray curve]. At about 1.5 ps after photoexcitation (red curves), a strong enhancement in $\sigma_2(\omega)$ was observed down to the lowest measured frequency, while $\sigma_1(\omega)$ remained gapped. This complex conductivity behavior underscores the increase in the superconducting coupling between layers and is incompatible with a charge excitation scenario. Indeed, the light-induced conductivity changes saturate with fluence (at ~ 1 mJ/cm^2) and do not follow the response of an incoherent plasma excited above a semiconducting gap. At later delays ($\tau = 5$ ps, blue curves), a relaxation toward a more incoherent state is observed.

The same qualitative behavior was found at 30 K, where the system is insulating at equilibrium. After photoexcitation, $\sigma_2(\omega)$ shows a strong light-induced enhancement at low frequency, turning positive and increasing with decreasing ω down to the lowest measured frequency, strongly resembling the response observed below Tc. These transient properties could be quantified by fitting the optical response with a Drude model:

$$\sigma_1(\omega) + i\sigma_2(\omega) = \frac{\omega_P^2}{4\pi} \frac{\tau_s}{1 - i\omega\tau_s} \tag{7.4}$$

where ω_P is the plasma frequency and τ_s is the carrier scattering time. The background in the optical spectra, mainly caused by phonon absorptions [see Fig. 7.2(b.1) and (b.2)] was simulated by adding high-frequency Lorentz oscillators chosen for the equilibrium compound and kept constant in all fits (see appendix A.2). Examples of these fits are reported as dashed lines in Figs. 7.5 (b.1) and (b.2).
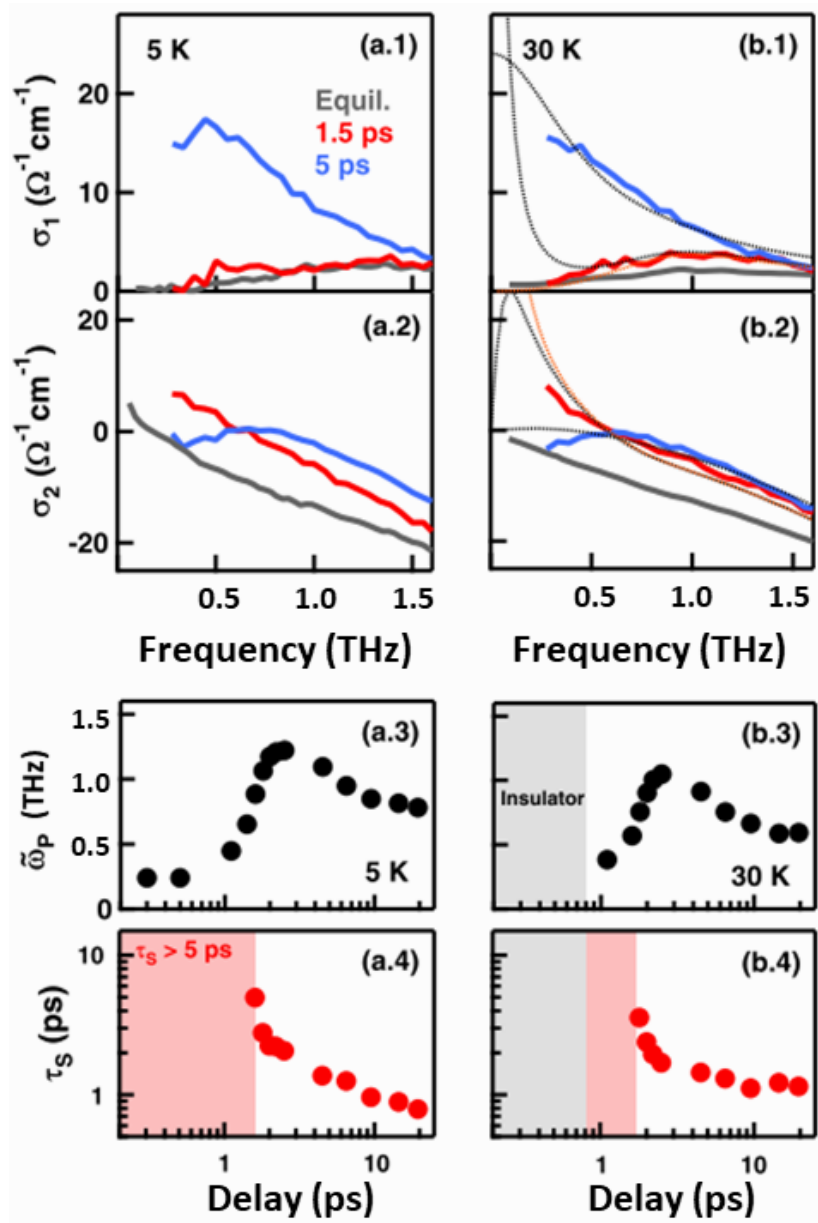
Figure 7.5. [Panels (a.1), (a.2), (b.1), (b.2)] Complex optical conductivity of $La_{1.885}Ba_{0.115}CuO_4$ at 5 K and 30 K, shown at different pump-probe delays, for a fluence of 2 mJ/cm2. In panels (b.1) and (b.2) examples of fits with a Drude model (black dots) and with a perfect-conductor model (red dots) are displayed. [Panels (a.3), (a.4), (b.3), (b.4)] Parameters extracted from the Drude fits as a function of pump-probe delay. The gray shaded region indicates the insulating regime (no Drude fit possible). The red shaded area refers to the highly coherent state.

Remarkably, the experimental data could be well reproduced at all temperatures and time delays. The extracted fit parameters, i.e., the screened plasma frequency $\widetilde{\omega}_P = \omega_P/\sqrt{\varepsilon_{FIR}}$ (where $\varepsilon_{FIR} \simeq 30$; see Ref. [38]) and the scattering time τ_s are displayed in Figs. 7.5 [panels (a.3), (a.4), (b.3), and (b.4)].

Below Tc [panels (a.3) and (a.4)] and at delays $\tau \lesssim 1.5$ ps the transient optical properties are described by a Drude model with scattering time $\tau_s > 5$ ps, or with the spectrum of a superconductor with $\tau_s \to \infty$:

$$\sigma_1(\omega) + i\sigma_2(\omega) = \frac{\omega_P^2}{8}\delta[\omega = 0] + \frac{\omega_P^2}{4\pi}\frac{i}{\omega} \tag{7.5}$$

Similar dynamics can be extracted also from the fits to the 30 K data [panels (b.3) and (b.4)] where, from the insulating ground state (gray region), a state with high-mobility carriers ($\tau_s > 5$ ps) is induced, whose optical properties are compatible with those of a transient superconductor. At longer time delays ($\tau \gtrsim 2$ ps), the system relaxes into a state only quantitatively different, in which coherence is reduced. Here the data can be fitted with a finite carrier scattering time $\tau_s \sim 5$ ps, reducing to $\tau_s \sim 1$ ps at later delays. At the same time, $\widetilde{\omega}_P$ continues to increase, exceeding 1 THz at $\tau_s \simeq 2.5$ ps, and then relaxing back to about 0.5 THz.

It is important to emphasis that within the frequency range over which the optical response of the transient state can be defined ($\omega \gtrsim \Gamma = 1/\tau_s$), a transient superconductor with lifetime τ_s and a normal conductor with a momentum relaxation rate $\Gamma = 1/\tau_s$ are indistinguishable. However, despite this ambiguity we describe/attribute the transient state in our experiments as a transient superconducting state for the following reasons:

1. We observe a continuous transformation from a weak superconductor at equilibrium as evidenced by a Josephson Plasma resonance, into a qualitatively identical phase with a blue-shifted resonance. At early time delays ($\tau \lesssim 2$ ps), the width of this resonance is essentially limited by our frequency resolution, giving $1/\Gamma$ values more than $\sim$ 5-10 ps, which corresponds to carrier mobilities

$\gtrsim 10^4 \text{ cm}^2(\text{Vs})^{-1}$. Such high values are unprecedented for out-of-plane transport in highly resistive normal state oxide [94].

2. At later time delays ($\tau \gtrsim$ 2-3 ps), the momentum relaxation rates extracted from the Drude fits, $1/\Gamma \approx 1$ ps, are still anomalously high for conventional incoherent charge transport, and are instead suggestive of a strongly fluctuating superconducting state [95,96], which may persist for several picoseconds after photo-excitation.

3. Lastly, from the frequency of the Josephson plasma resonance we can determine the Cooper pair density along the c-axis. The fact that such high mobility transport in the transient state occurs at a Cooper pair density which is comparable to that of the same compound at equilibrium, gives further credence to the picture of optically enhanced superconducting transport in photo-excited $La_{1.885}Ba_{0.115}CuO_4$.

In summary we show that superconducting interlayer coupling, which coexists with and is depressed by stripe order in $La_{1.885}Ba_{0.115}CuO_4$, can be enhanced by excitation with near-infrared laser pulses. For temperatures lower than T_c = 13 K, we observe a blue shift of the equilibrium Josephson plasma resonance, detected by terahertz-frequency reflectivity measurements. Key to these measurements is the ability to probe the optical properties at frequencies as low as 150 GHz, detecting the weak interlayer coupling strengths. For T > T_c a similar plasma resonance, absent at equilibrium, is induced up to the spin-ordering temperature $T_{SO} \simeq 40$ K. Furthermore, enhancement of the below-Tc interlayer coupling and its appearance above T_c are preferentially achieved when the near-infrared pump light is polarized perpendicular to the superconducting planes, likely due to more effective melting of stripe order and the less effective excitation of quasiparticles from the Cooper pair condensate when compared to in-plane excitation.

Summary and Outlook

In the work presented in this thesis, by using a combination of x-ray and optical spectroscopies we were able to establish a causal link and a hierarchy of timescales between rearrangement of the crystal structure, melting of stripe charge order, and enhanced superconducting phase rigidity, in stripe ordered $La_{1.885}Ba_{0.115}CuO_4$.

The measurement of both TR-RSXD and THz time-domain spectroscopy, under the same near-infrared excitation conditions, allows the first direct comparison of the time scales involved in the dynamics. The interlayer coupling enhancement, which develops in ~1 ps following photoexcitation, is strongly connected with the stripe order melting. On the other hand, the lattice dynamics start to develop on considerably longer timescales (>10 ps).

Additionally, the pump fluence dependence of the change in diffraction peak intensities $(\Delta I_\tau/I_0)$ for the stripe and LTT distortion diffraction peaks shown in Fig. S.1(a) establishes that at ~0.8 mJ/cm^2 the melting of the stripe ordering saturates whereas the LTT distortion remains largely intact. These changes can then be compared with the fluence-dependent Josephson interlayer coupling enhancement Fig. S.1(b), estimated by the increase in the low-frequency limit of the imaginary part of the conductivity $(\sigma_2)_{\omega \to 0}$ and by the change in the reflected electric field $(\Delta E_R/E_R)$ at the peak of the response. These results confirm the causal link between stripe melting and superconductivity enhancement, as both the (0.23 0 0.65) diffraction peak and the σ_2 response show a clear saturation at ~0.8 mJ/cm^2 fluence, which is not present for the (0 0 1) peak.

Though a conventional interpretation of competing charge-density wave and superconducting order posits that the two orders interact on energy scales commensurate with the ordering temperatures (~10 meV). This is not the case here
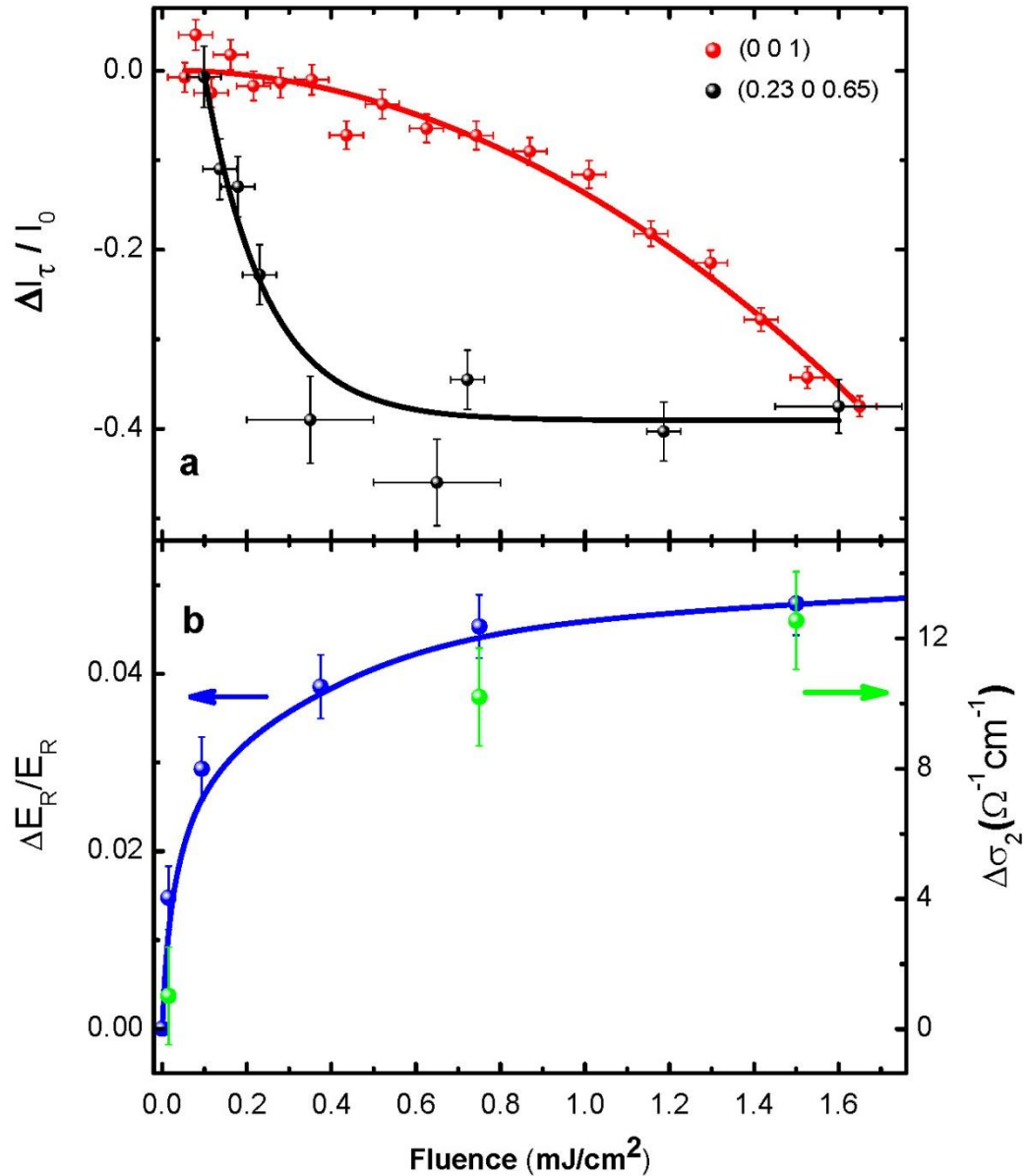
105

Figure. S.1. (a) Fluence dependence of the (0.23 0 0.65) charge-ordering diffraction peak and (001) LTT distortion diffraction peak intensity after photoexcitation with $\tau = 350$ ps. The error in the fluence indicates the uncertainty in the pump beam diameter at the sample position. The red line shows a quadratic fit whereas the black line shows an exponential fit to the data. (b) Changes in the electric field, $\Delta E_R/E_R$ (blue circles) and $(\sigma_2)_{\omega \to 0}$ (green circles) as a function of fluence (frequency = 0.2 THz, $\tau = 1.5$ ps). The blue line is an exponential function.
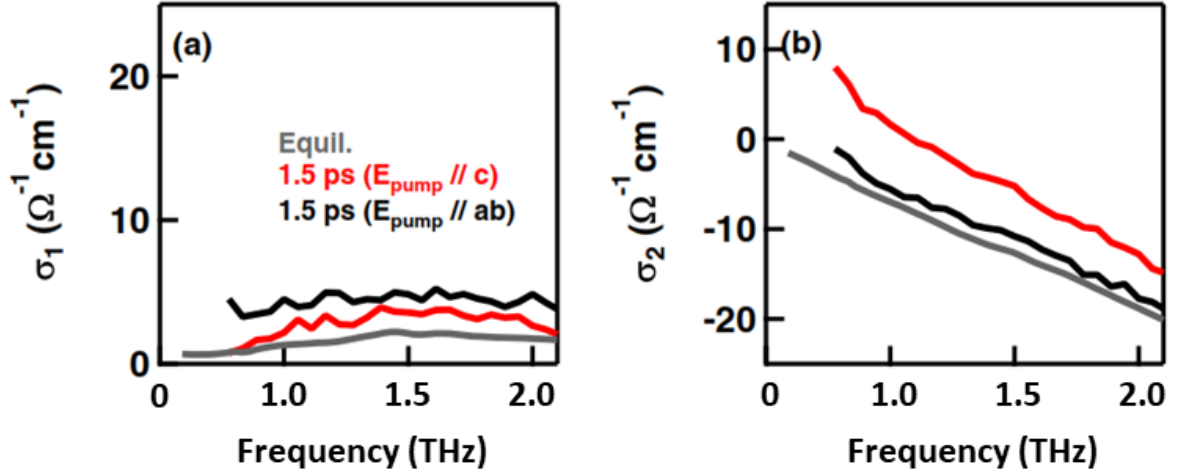
Figure S.2. (Color online) Complex optical conductivity of $La_{1.885}Ba_{0.115}CuO_4$ at 30 K, 1.5 ps after optical excitation with light polarized perpendicular (red) or parallel (black) to the CuO_2 planes. Data are taken with the same pump fluence of 2 mJ/cm^2.

where interactions on a high-energy scale compete and cooperate to provide order at far lower energies.

Lastly, the polarization-selective character of the enhanced coherent response is highlighted in Fig. S.2, where the transient optical conductivity at 30 K (red) is compared with that obtained after excitation with light polarized in the CuO_2 planes (black). Although a coherent response, attributable to a transiently enhanced Josephson tunneling, is certainly present for excitation parallel to the Cu-O planes, this appears to be enhanced and "optimized" for out-of-plane pumping. This aspect is evidenced not only by the stronger low-ω increase in $\sigma_2(\omega)$, but also by the much-reduced quasiparticle response in $\sigma_1(\omega)$.

Qualitatively the preferential enhancement of interlayer coherent coupling can be explained as light polarized out of plane does not couple to quasiparticle excitations in two-dimensional superconductors and is expected to couple only weakly in the quasi-two-dimensional case of cuprates. However, because of the peculiar arrangement of charge order in LBCO, in which parallel stripes in planes 1 and 3 (and 2 and 4) are shifted by π, coupling to the charge stripes and dipole activity is expected for polarization perpendicular to the planes [97].

More generally, our results show how the use of light to switch between different symmetries in complex materials can provide microscopic information on the stability of individual orders and complement linear spectroscopies in important ways. The collapse of stripe order along with the concomitant emergence of an improved superconducting phase should encourage further work to reveal the nature of the charge transfer process. Systematic studies of the conditions required to depress stripe order using charge transfer may become effective for high-speed devices in which the electrical, optical, and magnetic properties of highly correlated materials can be modified using near-infrared light.
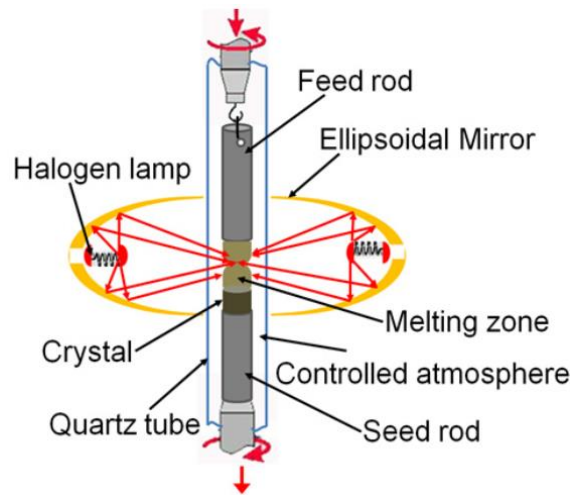
Appendix

A.1 Crystal Growth

Figure A.1. Schematic of the vertical cross section of a floating-zone furnace [98].

Single crystals of LBCO were grown using Traveling Solvent Floating Zone technique (TSFZ). TSFZ allows for the growth of large crystals with high melting point and a major advantage of this technique over others is that crystals can be grown without coming in contact with other materials, like crucibles, which eliminates the main source of contamination.

The crystals are grown inside an infrared radiation furnace equipped with two large ellipsoidal gold mirrors and halogen lamps. The light from the lamps is focused onto the melt, yielding a sharp temperature gradient around the molten zone, thereby providing stable conditions during the growth. The melt is situated between the polycrystalline feed rod and seed rod, which rotate counter to each other to ensure a homogenous mixing and temperature distribution inside the molten zone. In addition, the feed and seed rod are enclosed inside a quartz tube, giving a controlled atmosphere for crystal growth. A slow vertical translation of the feed rod initiates crystal growth,

109

which effectively corresponds to a melt traveling along the feed rod and thus the name Traveling Solvent Floating Zone.

The recipe used for growing single crystals of $La_{2-x}Ba_xCuO_4$ that were measured in the thesis is the following: the raw materials for the feed and seed rod are powders of La_2O_3, $BaCO_3$ and CuO. The powders are mixed in their metal ratios, ground in an agate mortar and then calcined in air at 970 °C for 24 hrs. This process was repeated three times. Thereafter, the powders are put into thin-walled rubber tubes and hydrostatically pressed at 4 kbars. The last step involves sintering in air for 48 hrs so as to obtain compact, high density rods.

The fed and seed rods are put inside the furnace and crystal growth is carried out under specific O_2 pressure, which depends on the desired doping of Ba. The vertical translation rate of the zone was 1.0 mm/hr and the rotation speed of the feed rod and grown crystal was 30 rpm.

A.2 Fitting Procedure

All transient optical spectra reported in this work was fitted either with a model describing a Josephson Plasma or with a Drude model for metals. For each data set taken at a specific temperature and pump-probe delay, the transient reflectivity, $R(\omega)$, and the real and imaginary part of the optical conductivity, $\sigma_1(\omega)$ and $\sigma_2(\omega)$, respectively, were fitted concurrently with a single set of parameters.

The phonon modes in the far- and mid-infrared spectral range (5 THz $\lesssim \omega \lesssim$ 20 THz) and the high frequency electronic absorption ($\omega \gtrsim$ 100 THz) were fitted from the equilibrium spectra with Lorentz oscillators, for which the complex dielectric function is expressed as

$$\tilde{\varepsilon}_{HF}(\omega) = \sum_i \frac{S_i^2}{(\Omega_i^2 - \omega^2) - i\omega\Gamma_i},$$

And kept fixed throughout the whole analysis. Here, Ω_i, S_i, and Γ_i are central frequency, strength, and damping coefficient of the ith oscillator, respectively.

An additional term in the model was introduced for the low-frequency spectral range ($\omega \lesssim$ 2.5 THz), which was directly probed in our pump-probe experiment. For all data taken at long time delays ($\tau \gtrsim$ 2 ps), for which the reflectivity edge appeared broadened, the transient optical spectra could be well reproduced by a simple Drude term. The full complex dielectric function used in this case is expressed as

$$\tilde{\varepsilon}_D(\omega) = \varepsilon_\infty \left[1 - \frac{\omega_p^2}{\omega^2 + i\omega\Gamma} \right] + \tilde{\varepsilon}_{HF}(\omega)$$

Where ω_p and Γ are the Drude plasma frequency and momentum relaxation rate, which were left as free parameters for the fit, while ε_∞ was kept fixed to 4.5, a standard value for high-T$_c$ cuprates [83].

For the early time delays, a model describing the optical response of a Josephson Plasma at equilibrium used to fit the data and compare results. This model was also

employed to reproduce the equilibrium spectra in the superconducting state and was able to fully capture all the main features – sharp edge in $R(\omega)$, a gapped $\sigma_1(\omega)$, and a diverging $\sigma_2(\omega)$ at low frequencies – observed at early time delays in our experiment.

The full dielectric function for this model is expressed as

$$\tilde{\varepsilon}_J(\omega) = \varepsilon_\infty \left[1 - \frac{\omega_J^2}{\omega^2}\right] + \tilde{\varepsilon}_N(\omega) + \tilde{\varepsilon}_{HF}(\omega)$$

Here, the free fit parameters are the Josephson Plasma frequency, ω_J, and $\tilde{\varepsilon}_N(\omega)$, a weak "normal fluid" component [99] (overdamped Drude term), which was introduced to replicate the small positive offset in $\sigma_1(\omega)$.

Bibliography

[1] Renée C, Renée R, Dissertation H, Phillips P W and Thaler J J
*MANIPULATING SUPERCONDUCTIVITY IN CUPRATES WITH
SELECTIVE ULTRAFAST EXCITATION*

[2] Fausti D, Tobey R I, Dean N, Kaiser S, Dienst A, Hoffmann M C, Pyon S,
Takayama T, Takagi H and Cavalleri A 2011 Light-Induced Superconductivity
in a Stripe-Ordered Cuprate *Science (80-.).* 331 189 LP – 191

[3] Tranquada J M, Sternlieb B J, Axe J D, Nakamura Y and Uchida S 1995
Evidence for stripe correlations of spins and holes in copper oxide
superconductors *Nature* 375 561–3

[4] Cavalleri A 2018 Photo-induced superconductivity *Contemp. Phys.* 59 31–46

[5] Khanna V, Mankowsky R, Petrich M, Bromberger H, Cavill S A, Möhr-
Vorobeva E, Nicoletti D, Laplace Y, Gu G D, Hill J P, Först M, Cavalleri A
and Dhesi S S 2016 Restoring interlayer Josephson coupling in
La1.885Ba0.115CuO 4 by charge transfer melting of stripe order *Phys. Rev. B*
93 224522

[6] Först M, Tobey R I, Bromberger H, Wilkins S B, Khanna V, Caviglia A D,
Chuang Y-D, Lee W S, Schlotter W F, Turner J J, Minitti M P, Krupin O, Xu
Z J, Wen J S, Gu G D, Dhesi S S, Cavalleri A and Hill J P 2014 Melting of
Charge Stripes in Vibrationally Driven La1.875Ba0.125CuO4 : Assessing the
Respective Roles of Electronic and Lattice Order in Frustrated
Superconductors *Phys. Rev. Lett.* 112 157002

[7] Nicoletti D, Casandruc E, Laplace Y, Khanna V, Hunt C R, Kaiser S, Dhesi S
S, Gu G D, Hill J P and Cavalleri A 2014 Optically induced superconductivity
in striped La2−xBaxCuO4 by polarization-selective excitation in the near

infrared *Phys. Rev. B* 90 100503

[8]   Kivelson S and Kivelson S A 2016 Defining emergence in physics *npj Quantum Mater.* 1 1

[9]   Andersen P W 1972 More is different *Science (80-.).* 177 393–6

[10]   H. Kamerlingh Onnes 1911 *Commun. Phys. Lab. Univ. Leiden. Suppl.29 (Nov. 1911)*

[11]   Blundell S J 2009 *Superconductivity* (Oxford University Press)

[12]   Prize N 1913 The Nobel Prize in Physics 1913 *https://www.nobelprize.org/prizes/physics/1913/summary/*

[13]   Meissner W and Ochsenfeld R 1933 Ein neuer Effekt bei Eintritt der Supraleitfähigkeit *Naturwissenschaften* 21 787–8

[14]   Rey C M and Malozemoff A P 2015 Fundamentals of superconductivity *Superconductors in the Power Grid: Materials and Applications* (Elsevier Ltd) pp 29–73

[15]   Doan M-L File:Meissner effect p1390048.jpg - Wikimedia Commons

[16]   Gorter C J and Casimir H 1934 On supraconductivity I *Physica* 1 306–20

[17]   London F and H communicated by Lindemann F A 1935 The electromagnetic equations of the supraconductor *Proc. R. Soc. London. Ser. A - Math. Phys. Sci.* 149 71–88

[18]   Pippard A B 1953 An experimental and theoretical study of the relation between magnetic field and current in a superconductor *Proc. R. Soc. London. Ser. A. Math. Phys. Sci.* 216 547–68

[19]   Tinkham M 1996 *Introduction to superconductivity* (New York : McGraw Hill)

[20]   Ginzburg, V.L., Landau L D 1950 No Title *Zh. Eksp. Teor. Fiz.* 20 1064

114

[21]   Anon 1965 ON THE THEORY OF SUPERCONDUCTIVITY *Collected Papers of L.D. Landau* (Elsevier) pp 546–68

[22]   Abrikosov A A 1957 *On the Magnetic Properties of Superconductors of the Second Group* vol 100

[23]   Buckel W and Kleiner R 2004 *Superconductivity* (Wiley)

[24]   Hess H F, Robinson R B, Dynes R C, Valles J M and Waszczak J V. 1989 Scanning-Tunneling-Microscope Observation of the Abrikosov Flux Lattice and the Density of States near and inside a Fluxoid *Phys. Rev. Lett.* 62 214–6

[25]   Maxwell E 1950 Isotope effect in the superconductivity of mercury [14] *Phys. Rev.* 78 477

[26]   Reynolds C A, Serin B, Wright W H and Nesbitt L B 1950 Superconductivity of isotopes of mercury [27] *Phys. Rev.* 78 487

[27]   Fröhlich H 1950 Theory of the superconducting state. I. The ground state at the absolute zero of temperature *Phys. Rev.* 79 845–56

[28]   Bardeen J and Pines D 1955 Electron-phonon interaction in metals *Phys. Rev.* 99 1140–50

[29]   Dresselhaus M S 2011 Superconducting Properties of Solids 1–68

[30]   Bardeen J, Cooper L N and Schrieffer J R 1957 Theory of superconductivity *Phys. Rev.* 108 1175–204

[31]   Prize N 1972 The Nobel Prize in Physics 1972 - NobelPrize.org *https://www.nobelprize.org/prizes/physics/1972/summary/*

[32]   Josephson B D 1962 Possible new effects in superconductive tunnelling *Phys. Lett.* 1 251–3

[33]   Shimano R and Tsuji N 2020 Higgs Mode in Superconductors *Annu. Rev.*

Condens. Matter Phys. 11 103–24

[34]   Smith P H, Shapiro S, Miles J L and Nicol J 1961 Superconducting characteristics of superimposed metal films *Phys. Rev. Lett.* 6 686–8

[35]   Anderson P W and Rowell J M 1963 Probable observation of the Josephson superconducting tunneling effect *Phys. Rev. Lett.* 10 230–2

[36]   Josephson B 1973 The Nobel Prize in Physics 1973 - NobelPrize.org

[37]   Josephson B 1973 *THE DISCOVERY OF TUNNELLING SUPERCURRENTS*

[38]   Homes C C, Hücker M, Li Q, Xu Z J, Wen J S, Gu G D and Tranquada J M 2012 Determination of the optical properties of La 2-xBa xCuO 4 for several dopings, including the anomalous x=18 phase *Phys. Rev. B - Condens. Matter Mater. Phys.* 85 134510

[39]   Laplace Y and Cavalleri A 2016 Josephson plasmonics in layered superconductors *Adv. Phys. X* 1 387–411

[40]   Bednorz J G and Müller K A 1986 Possible high Tc superconductivity in the Ba-La-Cu-O system *Zeitschrift für Phys. B Condens. Matter* 64 189–93

[41]   Bednorz J G, Takashige T and Müller K A 1987 Susceptibility measurements support high-tc superconductivity in the ba-la-cu-o system *Epl* 3 379–86

[42]   Anon The Nobel Prize in Physics 1987

[43]   Keimer B, Kivelson S A, Norman M R, Uchida S and Zaanen J 2015 From quantum matter to high-temperature superconductivity in copper oxides *Nature* 518 179–86

[44]   Kleiner R, Steinmeyer F, Kunkel G and Mller P 1992 Intrinsic Josephson effects in Bi2Sr2CaCu2O8 single crystals *Phys. Rev. Lett.* 68 2394–7

[45]   Lee P A, Nagaosa N and Wen X-G 2004 Doping a Mott Insulator: Physics of High Temperature Superconductivity *Rev. Mod. Phys.* 78

[46]   Emery V J and Kivelson S A 1995 Importance of phase fluctuations in superconductors with small superfluid density *Nature* 374 434–7

[47]   Zaanen J and Gunnarsson O 1989 Charged magnetic domain lines and the magnetism of high-Tc oxides *Phys. Rev. B* 40 7391–4

[48]   Uchida S, Ido T, Takagi H, Arima T, Tokura Y and Tajima S 1991 Optical spectra of La2-xSrxCuO4: Effect of carrier doping on the electronic structure of the CuO2 plane *Phys. Rev. B* 43 7942–54

[49]   Uchida S, Ido T, Takagi H, Arima T, Tokura Y and Tajima S 1991 Optical spectra of La2-xSrxCuO4: Effect of carrier doping on the electronic structure of the CuO2 plane *Phys. Rev. B* 43 7942–54

[50]   Moodenbaugh A R, Xu Y, Suenaga M, Folkerts T J and Shelton R N 1988 Superconducting properties of La2-xBaxCuO4 *Phys. Rev. B* 38 4596–600

[51]   Axe J D, Moudden A H, Hohlwein D, Cox D E, Mohanty K M, Moodenbaugh A R and Xu Y 1989 Structural phase transformations and superconductivity in La2-xBaxCuO4 *Phys. Rev. Lett.* 62 2751–4

[52]   Hücker M, V. Zimmermann M, Gu G D, Xu Z J, Wen J S, Xu G, Kang H J, Zheludev A and Tranquada J M 2011 Stripe order in superconducting La2-xBaxCuO 4 (0.095≤x≤0.155) *Phys. Rev. B - Condens. Matter Mater. Phys.* 83 104506

[53]   Kivelson S A, Fradin E and Emery V J 1998 Electronic liquid-crystal phases of a doped mott insulator *Nature* 393 550–3

[54]   Emery V J, Kivelson S A and Tranquada J M 1999 Stripe phases in high-temperature superconductors *Proc. Natl. Acad. Sci. U. S. A.* 96 8814–7

[55]   Berg E, Fradkin E, Kim E A, Kivelson S A, Oganesyan V, Tranquada J M and Zhang S C 2007 Dynamical layer decoupling in a stripe-ordered high-tc superconductor *Phys. Rev. Lett.* 99 127003

[56]   Fujita M, Goka H, Yamada K, Tranquada J M and Regnault L P 2004 Stripe order, depinning, and fluctuations in La1.875Ba 0.125CuO4 and La1.875Ba0.075Sr 0.050CuO4 *Phys. Rev. B - Condens. Matter Mater. Phys.* 70 104517

[57]   Fink J, Schierle E, Weschke E, Geck J, Hawthorn D, Soltwisch V, Wadati H, Wu H H, Dürr H A, Wizent N, Büchner B and Sawatzky G A 2009 Charge ordering in La1.8-x Eu0.2 Srx CuO4 studied by resonant soft x-ray diffraction *Phys. Rev. B - Condens. Matter Mater. Phys.* 79 100502

[58]   Chen C T, Sette F, Ma Y, Hybertsen M S, Stechel E B, Foulkes W M C, Schulter M, Cheong S W, Cooper A S, Rupp L W, Batlogg B, Soo Y L, Ming Z H, Krol A and Kao Y H 1991 Electronic states in La2-xSrxCuO4+ probed by soft-x-ray absorption *Phys. Rev. Lett.* 66 104–7

[59]   Chen C T, Tjeng L H, Kwo J, Kao H L, Rudolf P, Sette F and Fleming R M 1992 Out-of-plane orbital characters of intrinsic and doped holes in La2-xSrxCuO4 *Phys. Rev. Lett.* 68 2543–6

[60]   Abbamonte P, Rusydi A, Smadici S, Gu G D, Sawatzky G A and Feng D L 2005 Spatially modulated "Mottness" in La 2−x Ba x CuO 4

[61]   Hücker M, V. Zimmermann M, Debessai M, Schilling J S, Tranquada J M and Gu G D 2010 Spontaneous symmetry breaking by charge stripes in the high pressure phase of superconducting La1.875Ba0.125CuO4 *Phys. Rev. Lett.* 104 3–6

[62]   Li Q, Hücker M, Gu G D, Tsvelik A M and Tranquada J M 2007 Two-Dimensional Superconducting Fluctuations in Stripe-Ordered

La1.875Ba0.125CuO4 *Phys. Rev. Lett.* 99 067001

[63]   Fujita M, Hiraka H, Matsuda M, Matsuura M, Tranquada J M, Wakimoto S, Xu G and Yamada K 2012 Progress in neutron scattering studies of spin excitations in high-Tc cuprates *J. Phys. Soc. Japan* 81 1–19

[64]   Rajasekaran S, Okamoto J, Mathey L, Fechner M, Thampy V, Gu G D and Cavalleri A 2018 Probing optically silent superfluid stripes in cuprates *Science (80-.).* 359 575–9

[65]   Berg E, Fradkin E, Kivelson S A and Tranquada J M 2009 Striped superconductors: How spin, charge and superconducting orders intertwine in the cuprates *New J. Phys.* 11 115004

[66]   Stöhr J Birth of the X-Ray Laser: Movies of the Dynamic Worlds of Atoms and Electrons *http://www-ssrl.slac.stanford.edu/stohr/*

[67]   Orenstein J 2012 Ultrafast spectroscopy of quantum materials *Phys. Today* 65 44–50

[68]   Basov D N, Averitt R D and Hsieh D 2017 Towards properties on demand in quantum materials *Nat. Mater.* 16 1077–88

[69]   Zhang J and Averitt R D 2014 Dynamics and control in complex transition metal oxides *Annu. Rev. Mater. Res.* 44 19–43

[70]   Kusar P, Kabanov V V., Demsar J, Mertelj T, Sugai S and Mihailovic D 2008 Controlled vaporization of the superconducting condensate in cuprate superconductors by femtosecond photoexcitation *Phys. Rev. Lett.* 101 227001

[71]   Pashkin A, Porer M, Beyer M, Kim K W, Dubroka A, Bernhard C, Yao X, Dagan Y, Hackl R, Erb A, Demsar J, Huber R and Leitenstorfer A 2010 Femtosecond response of quasiparticles and phonons in superconducting YBa2Cu3O7-δ studied by wideband terahertz spectroscopy *Phys. Rev. Lett.* 105 067001

[72]   Stöhr J and Siegmann H C 2006 *Magnetism: From fundamentals to nanoscale dynamics* vol 152 (Springer Berlin Heidelberg)

[73]   Als-Nielsen J (Jens) and McMorrow D 2011 *Elements of modern X-ray physics* (Wiley)

[74]   Comin R and Damascelli A 2016 Resonant X-Ray Scattering Studies of Charge Order in Cuprates *Annu. Rev. Condens. Matter Phys.* 7 369–405

[75]   School of Crystallography, Birkbeck College U of L How do Synchrotrons Work?

[76]   Physics Stack Exchange particle physics - What is the difference between an undulator and a free-electron laser (FEL)? - Physics Stack Exchange

[77]   Ehrke H P 2010 *Dynamics of electronic order in Magnetoresistive Manganites studied with time-resolved x-ray scattering*

[78]   Inc. C Synchrolock-AP | Coherent

[79]   Laser Quantum *Tera-SED3 Tera-SED10*

[80]   Kai-Erik PeiponenAxel ZeitlerMakoto Kuwata-Gonokami Terahertz Spectroscopy and Imaging

[81]   Lee Y S 2009 *Principles of terahertz science and technology* (Springer US)

[82]   Dressel M and Grüner G 2002 Electrodynamics of Solids: Optical Properties of Electrons in Matter

[83]   Van der Marel D, Molegraaf H J A, Zaanen J, Nussinov Z, Carbone F, Damascelli A, Eisaki H, Greven M, Kes P H and Li M 2003 Quantum critical behaviour in a high-Tc superconductor *Nature* 425 271–4

[84]   Först M, Frano A, Kaiser S, Mankowsky R, Hunt C R, Turner J J, Dakovski G L, Minitti M P, Robinson J, Loew T, Le Tacon M, Keimer B, Hill J P,

Cavalleri A and Dhesi S S 2014 Femtosecond x rays link melting of charge-density wave correlations and light-enhanced coherent transport in YB a2 C u3 O6.6 *Phys. Rev. B - Condens. Matter Mater. Phys.* 90 184514

[85] Klauss H H, Wagener W, Hillberg M, Kopmann W, Walf H, Litterst F J, Hücker M and Büchner B 2000 From antiferromagnetic order to static magnetic stripes: The phase diagram of (La,Eu)2-xSrxCuO4 *Phys. Rev. Lett.* 85 4590–3

[86] Fink J, Soltwisch V, Geck J, Schierle E, Weschke E and Büchner B 2011 Phase diagram of charge order in La1.8-xEu0.2Sr xCuO4 from resonant soft x-ray diffraction *Phys. Rev. B - Condens. Matter Mater. Phys.* 83 6–9

[87] Emma P, Akre R, Arthur J, Bionta R, Bostedt C, Bozek J, Brachmann A, Bucksbaum P, Coffee R, Decker F J, Ding Y, Dowell D, Edstrom S, Fisher A, Frisch J, Gilevich S, Hastings J, Hays G, Hering P, Huang Z, Iverson R, Loos H, Messerschmidt M, Miahnahri A, Moeller S, Nuhn H D, Pile G, Ratner D, Rzepiela J, Schultz D, Smith T, Stefan P, Tompkins H, Turner J, Welch J, White W, Wu J, Yocky G and Galayda J 2010 First lasing and operation of an ångstrom-wavelength free-electron laser *Nat. Photonics* 4 641–7

[88] Schlotter W F, Turner J J, Rowen M, Heimann P, Holmes M, Krupin O, Messerschmidt M, Moeller S, Krzywinski J, Soufli R, Fernndez-Perea M, Kelez N, Lee S, Coffee R, Hays G, Beye M, Gerken N, Sorgenfrei F, Hau-Riege S, Juha L, Chalupsky J, Hajkova V, Mancuso A P, Singer A, Yefanov O, Vartanyants I A, Cadenazzi G, Abbey B, Nugent K A, Sinn H, Lning J, Schaffert S, Eisebitt S, Lee W S, Scherz A, Nilsson A R and Wurth W 2012 The soft x-ray instrument for materials studies at the linac coherent light source x-ray free-electron laser *Rev. Sci. Instrum.* 83 043107

[89] Doering D, Chuang Y D, Andresen N, Chow K, Contarato D, Cummings C, Domning E, Joseph J, Pepper J S, Smith B, Zizka G, Ford C, Lee W S,

Weaver M, Patthey L, Weizeorick J, Hussain Z and Denes P 2011 Development of a compact fast CCD camera and resonant soft x-ray scattering endstation for time-resolved pump-probe experiments *Rev. Sci. Instrum.* 82 073303

[90]   Wilkins S B, Dean M P M, Fink J, Hücker M, Geck J, Soltwisch V, Schierle E, Weschke E, Gu G, Uchida S, Ichikawa N, Tranquada J M and Hill J P 2011 Comparison of stripe modulations in La1.875Ba 0.125CuO4 and La1.48Nd0.4Sr 0.12CuO4 *Phys. Rev. B - Condens. Matter Mater. Phys.* 84 195101

[91]   Berg E, Fradkin E, Kim E-A, Kivelson S A, Oganesyan V, Tranquada J M and Zhang S C 2007 *Dynamical layer decoupling in a stripe-ordered, high T c superconductor*

[92]   Nicoletti D, Mitrano M, Cantaluppi A and Cavalleri A 2015 Comment on "Terahertz time-domain spectroscopy of transient metallic and superconducting states" (arXiv:1506.06758)

[93]   Casandruc E, Nicoletti D, Rajasekaran S, Laplace Y, Khanna V, Gu G D, Hill J P and Cavalleri A 2015 Wavelength-dependent optical enhancement of superconducting interlayer coupling in La1.885Ba0.115CuO4 *Phys. Rev. B* 91 174502

[94]   Kaiser S, Hunt C R, Nicoletti D, Hu W, Gierz I, Liu H Y, Le Tacon M, Loew T, Haug D, Keimer B and Cavalleri A 2014 Optically induced coherent transport far above Tc in underdoped YBa2Cu3 O6+Î *Phys. Rev. B - Condens. Matter Mater. Phys.* 89 184516

[95]   Bilbro L S, Aguilar R V, Logvenov G, Pelleg O, Božović I and Armitage N P 2011 Temporal correlations of superconductivity above the transition temperature in la 2-x Sr x CuO 4 probed by terahertz spectroscopy *Nat. Phys.* 7 298–302

[96]   Hunt C R, Nicoletti D, Kaiser S, Takayama T, Takagi H and Cavalleri A 2015

Two distinct kinetic regimes for the relaxation of light-induced superconductivity in La 1.675 Eu 0.2 Sr 0.125 Cu O 4 *Phys. Rev. B* 91 020505

[97] Mansart B, Lorenzana J, Mann A, Odeh A, Scarongella M, Chergui M and Carbone F 2013 Coupling of a high-energy excitation to superconducting quasiparticles in a cuprate from coherent charge fluctuation spectroscopy *Proc. Natl. Acad. Sci. U. S. A.* 110 4539–44

[98] Wen J *Interplay between magnetism and superconductivity in high-temperature superconductors La2-xBaxCuO4 and Fe1+yTe1-xSex: crystal growth and neutron scattering studies*

[99] van der Marel D and Tsvetkov A 1996 Transverse optical plasmons in layered superconductors *Czechoslov. J. Phys.* 46 3165–8

[100] Prize N Vitaly L. Ginzburg - Facts - NobelPrize.org *2003*